# Image-domain material decomposition in spectral photon-counting CT for medical applications

Bingqing Xie

N°d'ordre NNT : 2020LYSEI021

**THESE de DOCTORAT DE L'UNIVERSITE DE LYON**
opérée au sein de
**l'Institut National des Sciences Appliquées de Lyon**

**Ecole Doctorale** N° ED160
**Electronique, électrotechnique, automatique**

**Spécialité/ discipline de doctorat** :
**Traitement du Signal et de l'Image**

Soutenue publiquement/à huis clos le 19/Mars/2020, par :
**Bingqing XIE**

---

# Image-domain material decomposition in spectral photon-counting CT for medical applications

---

Devant le jury composé de :

| | |
|---|---|
| M. LAQUERRIERE Patrice, Professeur à l'Institut Pluridisciplinaire Hubert CURIEN | Rapporteur |
| MME. VINCENT Nicole, Professeur à l'Universités Paris Descartes | Rapporteuse |
| M. PIERE-SIMON Jouk, Professeur à CHU de Grenoble | Examinateur |
| M. ZHU Yuemin, Directeur de Recherche CNRS à l'INSA de Lyon | Directeur de thèse |
| MME. KAFTANDJIAN Valérie, Professeur à l'INSA de Lyon | Co-directrice de thèse |
| M. DUVAUCHELLE Philippe, Maître de Conférences à l'INSA de Lyon | Co-directeur de thèse |

# Département FEDORA – INSA Lyon - Ecoles Doctorales – Quinquennal 2016-2020

| SIGLE | ECOLE DOCTORALE | NOM ET COORDONNEES DU RESPONSABLE |
|---|---|---|
| CHIMIE | **CHIMIE DE LYON**<br>http://www.edchimie-lyon.fr<br>Sec. : Renée EL MELHEM<br>Bât. Blaise PASCAL, 3e étage<br>secretariat@edchimie-lyon.fr<br>INSA : R. GOURDON | **M. Stéphane DANIELE**<br>Institut de recherches sur la catalyse et l'environnement de Lyon<br>IRCELYON-UMR 5256<br>Équipe CDFA<br>2 Avenue Albert EINSTEIN<br>69 626 Villeurbanne CEDEX<br>directeur@edchimie-lyon.fr |
| E.E.A. | **ÉLECTRONIQUE, ÉLECTROTECHNIQUE, AUTOMATIQUE**<br>http://edeea.ec-lyon.fr<br>Sec. : M.C. HAVGOUDOUKIAN<br>ecole-doctorale.eea@ec-lyon.fr | **M. Gérard SCORLETTI**<br>École Centrale de Lyon<br>36 Avenue Guy DE COLLONGUE<br>69 134 Écully<br>Tél : 04.72.18.60.97 Fax 04.78.43.37.17<br>gerard.scorletti@ec-lyon.fr |
| E2M2 | **ÉVOLUTION, ÉCOSYSTÈME, MICROBIOLOGIE, MODÉLISATION**<br>http://e2m2.universite-lyon.fr<br>Sec. : Sylvie ROBERJOT<br>Bât. Atrium, UCB Lyon 1<br>Tél : 04.72.44.83.62<br>INSA : H. CHARLES<br>secretariat.e2m2@univ-lyon1.fr | **M. Philippe NORMAND**<br>UMR 5557 Lab. d'Ecologie Microbienne<br>Université Claude Bernard Lyon 1<br>Bâtiment Mendel<br>43, boulevard du 11 Novembre 1918<br>69 622 Villeurbanne CEDEX<br>philippe.normand@univ-lyon1.fr |
| EDISS | **INTERDISCIPLINAIRE SCIENCES-SANTÉ**<br>http://www.ediss-lyon.fr<br>Sec. : Sylvie ROBERJOT<br>Bât. Atrium, UCB Lyon 1<br>Tél : 04.72.44.83.62<br>INSA : M. LAGARDE<br>secretariat.ediss@univ-lyon1.fr | **Mme Sylvie RICARD-BLUM**<br>Institut de Chimie et Biochimie Moléculaires et Supramoléculaires<br>(ICBMS) - UMR 5246 CNRS - Université Lyon 1<br>Bâtiment Curien - 3ème étage Nord<br>43 Boulevard du 11 novembre 1918<br>69622 Villeurbanne Cedex<br>Tel : +33(0)4 72 44 82 32<br>sylvie.ricard-blum@univ-lyon1.fr |
| INFOMATHS | **INFORMATIQUE ET MATHÉMATIQUES**<br>http://edinfomaths.universite-lyon.fr<br>Sec. : Renée EL MELHEM<br>Bât. Blaise PASCAL, 3e étage<br>Tél : 04.72.43.80.46<br>infomaths@univ-lyon1.fr | **M. Hamamache KHEDDOUCI**<br>Bât. Nautibus<br>43, Boulevard du 11 novembre 1918<br>69 622 Villeurbanne Cedex France<br>Tel : 04.72.44.83.69<br>hamamache.kheddouci@univ-lyon1.fr |
| Matériaux | **MATÉRIAUX DE LYON**<br>http://ed34.universite-lyon.fr<br>Sec. : Stéphanie CAUVIN<br>Tél : 04.72.43.71.70<br>Bât. Direction<br>ed.materiaux@insa-lyon.fr | **M. Jean-Yves BUFFIÈRE**<br>INSA de Lyon<br>MATEIS - Bât. Saint-Exupéry<br>7 Avenue Jean CAPELLE<br>69 621 Villeurbanne CEDEX<br>Tél : 04.72.43.71.70 Fax : 04.72.43.85.28<br>jean-yves.buffiere@insa-lyon.fr |
| MEGA | **MÉCANIQUE, ÉNERGÉTIQUE, GÉNIE CIVIL, ACOUSTIQUE**<br>http://edmega.universite-lyon.fr<br>Sec. : Stéphanie CAUVIN<br>Tél : 04.72.43.71.70<br>Bât. Direction<br>mega@insa-lyon.fr | **M. Jocelyn BONJOUR**<br>INSA de Lyon<br>Laboratoire CETHIL<br>Bâtiment Sadi-Carnot<br>9, rue de la Physique<br>69 621 Villeurbanne CEDEX<br>jocelyn.bonjour@insa-lyon.fr |
| ScSo | **ScSo***<br>http://ed483.univ-lyon2.fr<br>Sec. : Véronique GUICHARD<br>INSA : J.Y. TOUSSAINT<br>Tél : 04.78.69.72.76<br>veronique.cervantes@univ-lyon2.fr | **M. Christian MONTES**<br>Université Lyon 2<br>86 Rue Pasteur<br>69 365 Lyon CEDEX 07<br>christian.montes@univ-lyon2.fr |

*ScSo : Histoire, Géographie, Aménagement, Urbanisme, Archéologie, Science politique, Sociologie, Anthropologie

**Abstract**

Material decomposition is a fundamental and primordial problem in spectral photon-counting X-ray CT (sCT). The present thesis focuses on the development of material decomposition methods using spectral and morphological information embedded in multi-energy sCT images. In this framework, three methods were developed. For the first method, by using bounded mass density, local joint sparsity and structural low-rank (DSR) in image domain, we achieve highly accurate decomposition of materials such as gadolinium, iodine and iron. The results on both numerical phantom and physical data demonstrated that the proposed DSR method leads to more accurate decomposition than usual pseudo-inverse method with singular value decomposition (SVD) and current popular sparse regularization method with L1-norm constraint. The second method works in a region-wise manner. It consists in optimizing basis materials based on spatio-energy segmentation of regions-of-interests (ROIs) in sCT images, reducing noise by averaging multi-energy spatial images, and performing a fine material decomposition involving optimized decomposition matrix, denoising regularization and sparsity regularization. The results on both digital and physical data showed that the proposed ROI-wise material decomposition method presents clearly higher reliability and accuracy compared to common decomposition methods based on total variation (TV) or L1-norm (lasso) regularization. In the third method, we propose the notion of super-energy-resolution (SER) sCT imaging, which is realized through establishing the relationship between simulation and physical phantoms by means of coupled dictionary learning in a pixel-wise way. The effectiveness of the proposed methods was validated on digital phantom, physical phantoms and in vivo data. The results showed that for the same decomposition method using lasso regularization, the proposed super-energy-resolution imaging presents much higher decomposition accuracy and detection ability compared to what can be provided by current sCT machine.

**Keywords:** Computed tomography, X-ray, Spectral CT, Photon-counting detector, Material decomposition, Machine learning, Sparse representation

**Résumé**

La décomposition de matériaux est un problème fondamental et primordial dans la tomographie spectrale (sCT—spectral computed tomography) par rayons X basée sur des détecteurs à comptage de photons (PCD—photon-counting detector). La présente thèse porte sur le développement de méthodes de décomposition de matériaux en utilisant des informations spectrale et morphologique encodées dans des images sCT multi-énergie. Dans ce cadre, trois méthodes ont été développées. Pour la première méthode, en utilisant la densité de masse limitée, la parcimonie conjointe locale, et le faible rang structurel (DSR) dans le domaine de l'image, nous obtenons une décomposition très précise de matériaux tels que le gadolinium, l'iode et le fer. Les résultats sur les données numériques et physiques du fantôme ont démontré que la méthode DSR proposée conduit à une décomposition plus précise que la méthode pseudo-inverse habituelle avec décomposition en valeur singulière (SVD—singular value decomposition) et la méthode de régularisation parcimonieuse courante avec contrainte de norme L1 (lasso). La deuxième méthode opère par région. Elle consiste à optimiser les matériaux de base en se basant sur la segmentation spatio-énergétique des régions d'intérêt (ROI—regions-of-interests) dans les images sCT, à réduire le bruit en faisant le moyennage des images spatiales multi-énergie, et à effectuer une décomposition fine des matériaux impliquant une matrice de décomposition optimisée, une régularisation du débruitage et une régularisation parcimonieuse. Les résultats sur des données numériques et physiques ont montré que la méthode proposée de décomposition des matériaux ROI par ROI (ROI-wise—region-of-interests-wise) présente une fiabilité et une précision nettement supérieures à celles des méthodes de décomposition courantes fondées sur la régularisation de la variation totale (TV) ou de la norme L1. Dans la troisième méthode, nous proposons la notion d'imagerie sCT à super-résolution énergétique (SER—super-energy-resolution), qui est réalisée en établissant la relation entre la simulation et les fantômes physiques au moyen d'un apprentissage par dictionnaire couplé, de manière pixel par pixel. L'efficacité de ces méthodes proposées a été validée sur des données de fantômes numériques, de fantômes physiques et in vivo. Les résultats montrent que, pour la même méthode de décomposition de matériaux utilisant la régularisation par lasso, l'imagerie à super-résolution énergétique proposée présente une précision de décomposition et un pouvoir de détection beaucoup plus élevé que ce que peut fournir la machine sCT actuelle.

**Keywords** : Tomographie, Rayons X, CT spectrale, Détecteur à comptage des photons, Décomposition de matériaux, Apprentissage machine, Représentation éparse

# Contents

# List of Figures

# List of Tables

# Résumé étendu en français de la thèse

En 1971, Godfrey Hounsfield a construit le premier scanner de tomographie (CT—computed tomography) par rayons X. Son co-inventeur Allan McLeod Cormack, quelques années auparavant, avait utilisé la transformée de Radon et son inverse pour décrire théoriquement un appareil de tomographie radiologique et une méthode de reconstruction d'image. Pour leurs recherches, Cormack et Hounsfield ont reçu le prix Nobel de physiologie ou de médecine en 1979.

Actuellement, le scanner CT classique est une technique de balayage radiologique largement utilisée dans les domaines cliniques et industriels. Il permet de répondre à des tâches diagnostiques urgentes telles que la stadification des tumeurs en oncologie, l'analyse des accidents vasculaires cérébraux aigus ou la planification de la radiothérapie, ainsi qu'à des missions industrielles telles que l'analyse de la qualité et le balayage des bagages.

Le scanner CT à bi-énergie (DECT—dual-energy CT) a ensuite été étudié par Alvarez et Macovski en 1976 [Alvarez and Macovski, 1976, Macovski et al., 1976]. Les scanners DECT ont permis d'obtenir des informations sur les propriétés d'atténuation dépendantes de l'énergie (c'est-à-dire spectrales mais seulement deux) de l'objet. Différentes réalisations techniques ont été utilisées. La solution la plus simple est la technique dite de double kVp. Deux scans CT avec différentes tensions d'accélération du tube par rayons X sont effectués. Les deux ensembles de données qui en résultent contiennent des informations sur les caractéristiques spectrales d'atténuation des rayons X de l'objet. Ces données spectrales peuvent être utilisées pour obtenir des informations supplémentaires sur l'objet. Néanmoins, les scanners DECT n'effectuent qu'une analyse en deux points de l'atténuation des rayons X, ce qui améliore la caractérisation des tissus et permet une quantification assez précise de l'iode, mais est insuffisant pour discriminer simultanément l'iode et le gadolinium, surtout à faible dose de rayonnement [Si-Mohamed et al., 2017a]. De plus, de nombreux scanners DECT exposent le patient à deux faisceaux d'énergie qui peuvent entraîner une exposition au rayonnement potentiellement élevée,

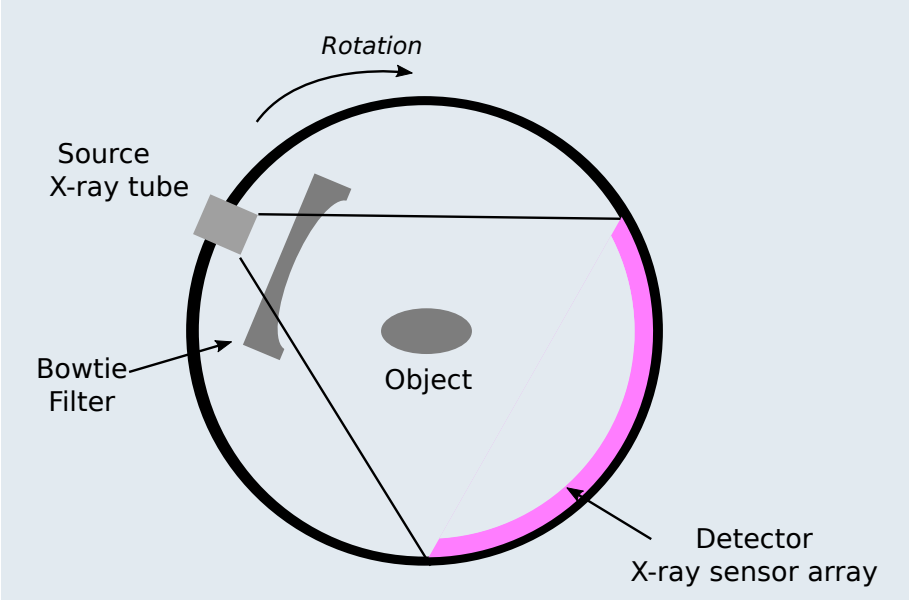


Figure 1: Mesure de l'atténuation des rayons X en CT. Les photons des rayons X émis par la source passent à travers l'objet qui est généralement un patient pour des applications cliniques. Le détecteur mesure une intensité des rayons X quantiques, résolue spatialement sur le faisceau en éventail des rayons X. Il est à noter qu'un filtre en forme de noeud papillon placé devant le tube à rayons X avant d'irradier un objet quelconque est habituellement appliqué pour moduler le flux des rayons X.

et le mouvement peut créer des problèmes pour aligner les deux ensembles de données.

La tomographie spectrale (sCT—spectral CT) ou multi-énergie a récemment fait l'objet d'une attention de plus en plus intense, en raison des nouvelles avancées de la technologie des détecteurs à comptage de photons (PCD—photon-counting detector). Par rapport à l'énergie conventionnelle intégrant le CT ou DECT, le sCT peut compter le nombre de photons dans des bandes d'énergie séparées avec une seule exposition [Taguchi and Iwanczyk, 2013, Faby et al., 2015]. De cette façon, plusieurs matériaux peuvent être identifiés simultanément. Un certain nombre de méthodes de décomposition de matériaux ont été reportées et différents systèmes expérimentaux sont en cours de développement. Cependant, la plupart des recherches se concentrent sur l'imagerie des agents de contraste à numéro atomique élevé (numéro $Z$), tels que l'iode, le gadolinium et l'or, qui ont des bords K (*i.e.* k-edge) uniques dans la gamme d'énergie de détection. Il est beaucoup plus difficile de distinguer ceux qui ont un faible numéro atomique, surtout lorsque leur numéro $Z$ est proche.

La figure 1 illustre la mise en place d'une mesure d'atténuation des rayons X en CT générale. La source $\boldsymbol{S}$ émet un flux des rayons X quantiques sur un objet. L'objet $\boldsymbol{O}$ est constitué de matériaux atténuant les rayons X qui sont décrits par leur coefficient

d'atténuation linéaire $\mu(\vec{x}, E)$ à la position $\vec{x}$. Le détecteur enregistre le quantum passant à travers l'objet.

La principale différence entre le sCT et le CT classique intégrant l'énergie ou DECT est le détecteur. Pour le CT conventionnel ou le DECT, les détecteurs ne comptent que les photons d'énergie différente dans un seul (energy intergraing detectors Figure 2(a)) ou deux canaux (dual-layer detectors in Figure 2(b)), alors que pour le sCT, le nouveau détecteur à comptage de photons peut enregistrer les photons dans plusieurs canaux ou bande (PCDs in Figure 2(c)). Dans ce qui suit, nous passons brièvement en revue les caractéristiques spectrales de la source, les atténuations dans l'objet et les détecteurs pour différentes images de tomographie.

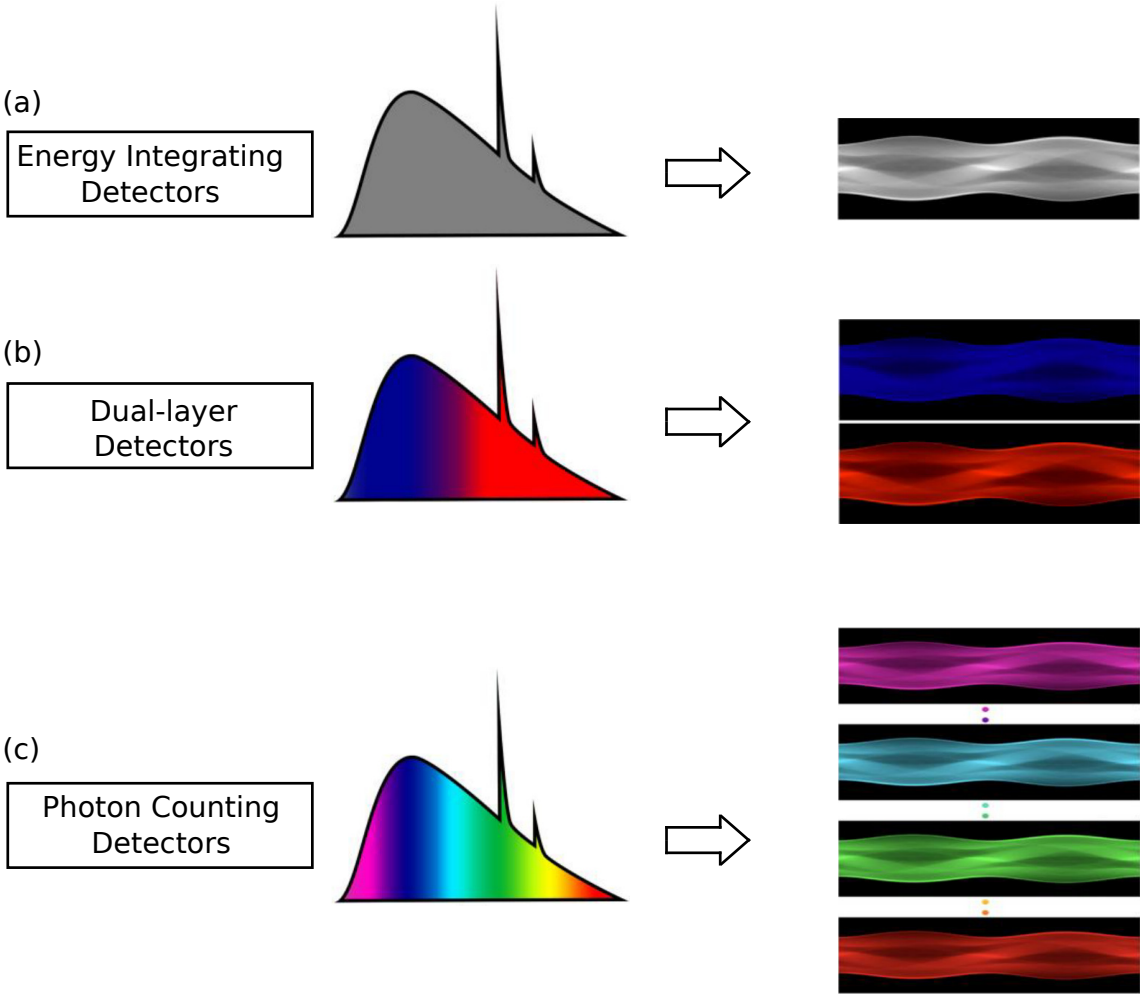


Figure 2: Représentation des informations fournies par différents détecteurs dans un CT à rayons X. (a) Détecteurs à intégration d'énergie; (b) Détecteurs à double couche; (c) Détecteurs de comptage de photons.

Le sCT peut compter le nombre de photons dans des bandes à énergie multiple séparées avec une seule exposition, ce qui est conceptuellement avantageux par rapport à DECT. A l'heure actuelle, DECT a connu une grande gamme d'applications cliniques, *p. ex.* imagerie virtuelle mono-énergétique, élimination automatisée des os et des plaques en angiographie par CT, imagerie virtuelle sans contraste et sans calcium, caractérisation des calculs rénaux et distinction entre la goutte et la pseudo goutte [Kalender et al., 1988, Wu et al., 2009, Matsumoto et al., 2011, Yu et al., 2012, Mendonca et al., 2014, McCollough et al., 2015, Zhao et al., 2016, Iyama et al., 2018]. Bien que le sCT ne soit pas encore utilisé en pratique clinique, elle offre des perspectives prometteuses pour de nombreuses applications d'importance vitale et ouvre de nombreuses possibilités d'application. Le principal avantage de la technologie sCT est un meilleur échantillonnage de l'information spectrale du spectre transmis. Parmi les applications de l'utilisation de l'information spectrale, la décomposition quantitative des matériaux est le sujet le plus délicat, y compris l'imagerie du *k-edge* des produits de contraste et l'imagerie sélective d'autres matériaux auparavant impossibles à distinguer. De plus, l'imagerie monochromatique virtuelle est une autre méthode d'utilisation de l'information spectrale pour améliorer la qualité de l'image. D'autres améliorations du sCT par rapport au CT classique, comme une résolution spatiale plus élevée, une exposition au rayonnement plus faible et un bruit plus faible, devraient également apporter des avantages pour l'imagerie diagnostique.

La première partie de ce manuscrit, qui décrit le contexte nécessaire pour les chapitres suivants:

**Chapitre1**, intitulé " *Principles of Spectral CT* ", les principes du CT par rayons X commune sont présentés, y compris la source des rayons X et l'interaction des rayons X avec les matériaux; le principe de différents détecteurs pour différents types de CT par rayons X est introduit, y compris le CT classique à énergie intégrée, DECT et sCT; les applications du nouvelle sCT sont introduites.

**Chapitre2**, intitulé " *Models of Material Decomposition and Mathematical Foundations*", présente un examen des méthodes de décomposition de matériaux existantes pour la tomographie spectraler par rayons-X. Les modèles de décomposition de matériaux basés sur différentes méthodes sont décrits, y compris les méthodes dans le domaine de projection, dans le domaine de l'image et à une étape; différentes méthodes d'optimisation sont examinées.

La deuxième partie est consacrée aux méthodes de décomposition du matériau dans le domaine d'image:

**Chapitre3**, intitulé "*Material Decomposition in X-ray Spectral CT Using Multiple Constraints in Image Domain*", en utilisant la densité de masse limitée, la parcimonie conjointe locale, et le faible rang structurel (DSR) dans le domaine de l'image, nous obtenons une

décomposition très précise de matériaux tels que le gadolinium, l'iode et le fer. Les résultats sur les données numériques et physiques du fantôme ont démontré que la méthode DSR proposée conduit à une décomposition plus précise que la méthode pseudo-inverse habituelle avec décomposition en valeur singulière (SVD—singular value decomposition) et la méthode de régularisation parcimonieuse courante avec contrainte de norme L1 (lasso).

Selon le type et le nombre de matériaux de base, la décomposition de matériaux dans le sCT peut être un problème inverse mal posé, voire mal conditionné. Un tel problème peut survenir avant [Schlomka et al., 2008, Zimmerman and Schmidt, 2015, Ducros et al., 2017], pendant [Foygel Barber et al., 2016, Mechlem et al., 2018, Hou et al., 2018], ou après [Taguchi et al., 2007, Le Huy and Molloi, 2011, Faby et al., 2014, Li et al., 2015, Li et al., 2017] le processus de reconstruction de l'image. Un certain nombre de méthodes de décomposition de matériaux ont été rapportées dans la littérature. Elles peuvent être classées en deux types principaux: l'optimisation sans et avec régularisation. La méthode pseudo-inverse avec SVD est une méthode d'optimisation habituelle sans régularisation [Faby et al., 2014]. Dans la méthode d'optimisation avec régularisation, une représentation parcimonieuse a souvent été utilisée car les données multi-énergie ont souvent une corrélation élevée. La principale motivation de la représentation parcimonieuse est d'utiliser la nature parcimonieuse des données multidimensionnelles. Une représentation parcimonieuse appropriée peut donner une décomposition précise des matériaux avec peu de bandes d'énergie. En général, la représentation parcimonieuse par minimisation de la norme L1 est considérée comme efficace dans de nombreux domaines [Candes et al., 2006, Donoho, 2006] pour éviter le surlissage. D'autres méthodes basées sur la représentation parcimonieuse ont également été étudiées pour la décomposition de matériaux, y compris le gradient parcimonieuse via la variation totale bilatérale (TVB) [Clark and Badea, 2014] et la transformation parcimonieuse via le cadre serré [Gao et al., 2011]. Toutes les méthodes citées ci-dessus ont été développées dans des cas surdéterminés; aucun travail n'est disponible pour la décomposition de matériaux dans des cas sous-déterminés où le nombre de matériaux de base est supérieur à celui des bandes d'énergie.

En fait, dans la pratique, un objet contient toujours de multiples matériaux et nous ne savons pas a priori quel est le nombre exact de matériaux qu'il contient. Par conséquent, la décomposition de matériaux dans les cas sous-déterminés reste un problème pratique. Le fait que les matériaux de base à numéros atomiques proches ont des coefficients d'atténuation massique similaires vient aggraver le problème. Pour faire face à ces problèmes, nous proposons d'utiliser les caractéristiques communes de parcimonie ou sparsité [Nie et al., 2010] des informations spectrales et spatiales. De plus, comme les

pixels voisins ont des matériaux similaires, nous exploitons la sparsité conjointe dans de petits voisinages locaux. En même temps, nous utilisons aussi la propriété structurelle de rang inférieur selon laquelle les matériaux décomposés dans une petite région locale correspondante devraient partager le même bord ('edge'), en raison de la propriété locale selon laquelle, dans une région locale, un matériau décomposé est soit présent soit absent à chaque pixel de la région. Enfin, comme la densité de masse des matériaux a toujours une valeur limitée, nous introduisons une contrainte liée à la densité de masse. Tout cela nous amène à proposer une méthode de décomposition de matériaux basée sur la densité de masse limitée, la parcimonie conjointe locale, et le faible rang structurel.

Une telle sparsité mixte de dimensions spectrale et spatiale serait intéressante pour décomposer des matériaux similaires de manière robuste. Nous adoptons alors la norme mixte L2,1 qui est particulièrement adaptée aux petites régions pour combiner les informations. La notion détaillée de la norme L2,1 est examinée au chapitre 3. La norme L2,1 peut imposer un petit nombre de lignes non nulles dans $\boldsymbol{X}$, comparé à la norme L1 habituelle qui tend à donner une solution parcimonieuse pixel par pixel. En d'autres termes, la norme L1 limite le nombre de matériaux existant en un pixel, alors que la norme L2,1 impose aux pixels de partager les mêmes atomes de matériaux de base dans chaque petit patch local. Pour la présente application des images de sCT, la norme L2,1 nous permet de combiner les informations spatiales (lignes en X) et spectrales (colonnes en X). En même temps, en plus des similitudes spectrales et spatiales, les images multi-énergie présentent également la cohérence structurelle, qui reflète le fait que les matériaux décomposés devraient partager les mêmes bords dans la même petite régions en raison de leur propriété locale dans l'image. De telles informations de bord dans une image de matériau sont également rares et peuvent être saisies par l'opérateur de gradient. Pour traiter les similitudes de bord, nous utilisons une représentation de bas rang sur les matrices de gradient de tous les matériaux décomposés. La contrainte de rang bas est réalisée via la norme nucléaire qui est l'enveloppe convexe de la matrice de rang [Candès et al., 2011].

La performance de la méthode proposée de décomposition du matériau DSR a été évaluée sur des données de fantômes numériques et physiques. Deux méthodes ont été comparées à la méthode de DSR proposée: (a) méthode pseudo-inverse avec SVD, (b) méthode de régularisation avec contrainte de la norme L1 (L1).

Les données de projection du sCT ont été simulées à l'aide du logiciel Virtual X-ray Imaging (VXI) de l'INSA [Duvauchelle et al., 2000], puis reconstruites par la méthode FBP. Le fantôme reconstruit a 800 * 800 pixels et contient cinq matériaux: eau, polyméthacrylate de méthyle (PMMA), gadolinium (Gd), iode (I) et fer (Fe), comme le montre la figure 3. Le numéro figurant sur chaque disque désigne la concentration des matériaux (mg/cc).

Notons que le disque avec # désigne les inserts de mélange qui contiennent trois matériaux de base (Gd, I et Fe) avec la même concentration dans chaque colonne. Les bandes d'énergie des rayons X ont été réglées comme suit: 30-40kev, 40-50kev, 50-60kev, 60-70kev et 70-80kev. Le nombre de bandes d'énergie 5 est choisi en suivant la configuration du prototype Philips.

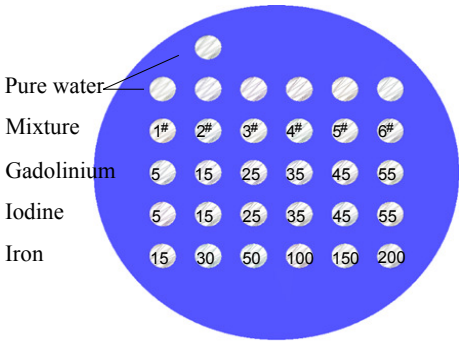


Figure 3: Fantôme numérique.

Pour évaluer pleinement les impacts du bruit, nous énumérons les résultats de la décomposition de matériaux sur la base d'une image reconstruite sans et avec bruit de Poisson. Entre-temps, la décomposition sur différents matériaux de base a été testée, en ce qui concerne les effets énormes de la catégorie et du nombre de matériaux de base. En outre, les impacts des bandes à faible énergie ont été évalués, sur lesquels les résultats de décomposition sont présentés dans la section 3.4.1. Nous n'énumérons que les résultats de cinq matériaux de base existants avec bruit de Poisson dans la figure 4.

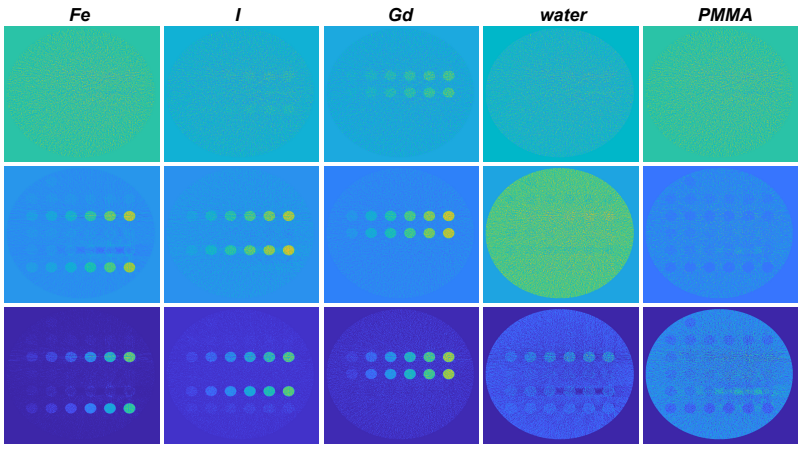


Figure 4: Les résultats de la décomposition de matériaux basés sur les images sCT reconstruites avec le bruit de Poisson en utilisant les trois méthodes: 5 bandes d'énergie, 5 matériaux de base. De haut en bas: Pseudo-inverse avec SVD, L1 et DSR.

Même pour le matériau sans k-edge (Fe), DSR montre une bonne capacité de détection

et de quantification, qui est similaire aux résultats sans bruit de Poisson. Visuellement, il y a évidemment plus d'erreurs pour les matériaux semblables à l'eau que pour le fer, l'iode et le gadolinium. Heureusement, dans les applications pratiques, les informations quantitatives des trois derniers matériaux sont plus utiles, ce qui nous permet de porter une plus grande attention aux matériaux d'intérêt: le fer, l'iode et le gadolinium.

Le fantôme physique a été acquis sur un sCT prototype de Phillips [Si-Mohamed et al., 2018, Cormode et al., 2017]. Le balayage consiste en 2400 projections; chaque projection a 643 rayons parallèles; chaque rayon contient 5 bandes d'énergie: 30-50 kev, 51-61 kev, 62-71 kev, 72-82 kev et 83-130 kev. Les photons incidents $n_0(E)$ et la fonction de réponse de la bande de détection $d_i(E)$ ont été fournis par le fabricant du prototype sCT. Le fantôme physique est représenté sur la figure 5a. L'annotation est la même que pour le fantôme numérique. Nous avons reconstruit l'image spatiale de chaque bande d'énergie via SART-TV, et l'image reconstruite de la première bande est présentée dans la Fig. 5b, où les artéfacts en anneau sont évidents. L'image reconstruite à chaque bande a une taille de 380*380.

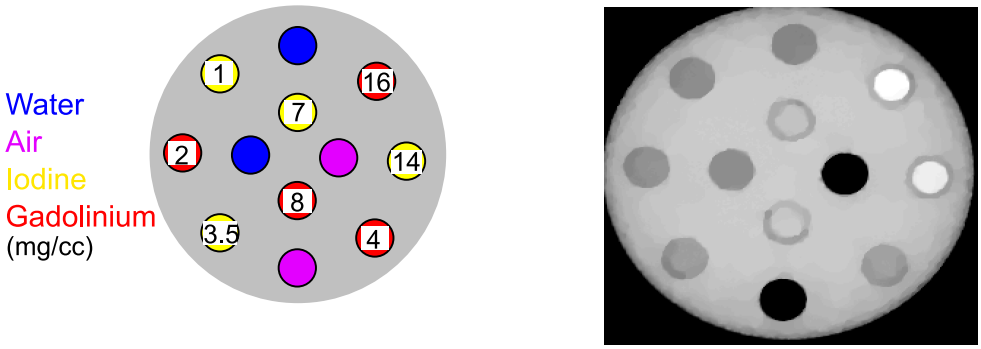


(a) (b)

Figure 5: (a) Le fantôme physique; (b) l'image reconstruite du fantôme physique à la première borne d'énergie.

Les résultats de la décomposition de matériaux sur le fantôme physique sont présentés dans la figure 6. Vu la mauvaise capacité de séparation entre l'eau et de la PMMA et leur faible intérêt dans les applications cliniques, nous n'avons considéré que trois matériaux de base, l'eau, l'iode et le gadolinium, dans le fantôme physique. La méthode de décomposition de matériaux DSR proposée est nettement plus performante en matière de détection et de quantification que les méthodes SVD et L1.

Entre-temps, nous disposons d'autres données in vivo pour évaluer plus en détail la méthode proposée. Des images reconstruites d'un lapin 15 min après l'injection de

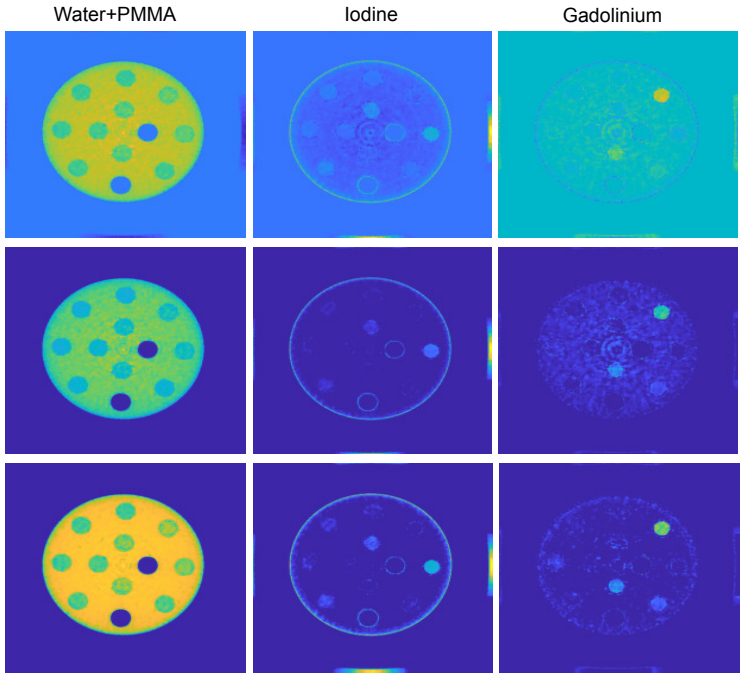


Figure 6: Les résultats de la décomposition de matériaux sur la base du fantôme physique. De haut en bas: Pseudo-inverse avec SVD, L1 et DSR.

gadolinium sont présentées dans la Fig. 7. Notons que le calcium (Ca) dans la colonne vertébrale est décomposé sur la base de l'iode du matériau, en raison de leur similitude de coefficients d'atténuation de masse dans notre réglage des seuils d'énergie. Pour le gadolinium, bien que la vérité de base soit inconnue dans les données in vivo, des tubes de dilutions de gadolinium à proximité du lapin ont été évalués alternativement.

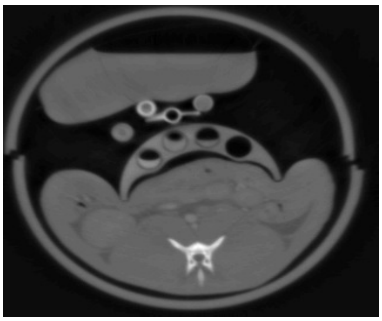

Figure 7: L'image reconstruite des données in vivo au premier bande d'énergie 15 min après l'injection de gadolinium.

Pour les données in vivo, les résultats de décomposition des différentes méthodes sont présentés dans la Fig. 8. Il est évident que les méthodes SVD et L1 ont une capacité de détection plus faible pour l'iode et le gadolinium. Au contraire, la méthode DSR proposée a une plus grande précision pour l'iode et le gadolinium. Il convient de noter qu'aucune des trois méthodes ne peuvent détecter le gadolinium à 2 mg/cc dans les données in vivo.

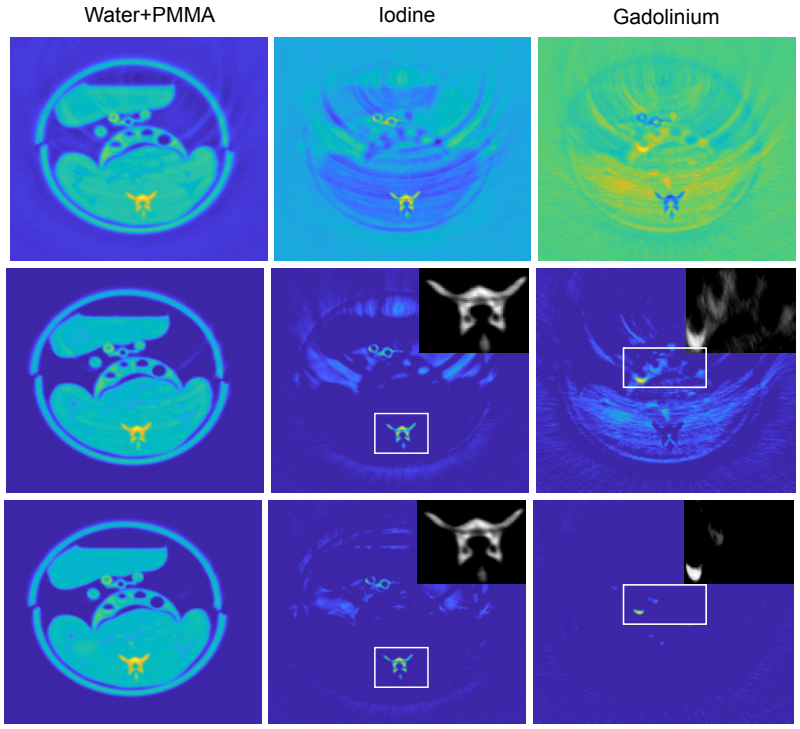


Figure 8: Les résultats de la décomposition de matériaux basés sur les données in vivo. De haut en bas: Pseudo-inverse avec SVD, L1 et DSR.

Nous avons proposé une méthode de décomposition de matériaux pour le sCT en exploitant simultanément la valeur limitée de la densité de masse, la nature multidimensionnelle, et la forte corrélation des données multiénergétiques et la propriété locale des pixels voisins. Pour surmonter les difficultés dues aux similitudes entre les matériaux de base, les redondances spectrales et spatiales sont éliminées en utilisant la sparsité mixte et le faible rang structurel. En même temps, nous ajoutons également une contrainte liée à la densité de masse, ce qui est naturellement vrai dans les applications pratiques. Les résultats préliminaires ont révélé que la méthode DSR proposée a une bonne capacité de décomposition de matériaux, même pour des problèmes très mal conditionnés.

La régularisation dans la méthode DSR proposée est un problème convexe. Nous avons utilisé un algorithme itératif ADMM (alternating direction method of multipliers)

pour résoudre le modèle proposé. Pour accélérer la convergence, l'initialisation des variables dans l'ADMM a été fixée comme les résultats de la pseudo-inverse avec la méthode DSR. Bien qu'il y ait quatre régularisations dans la fonction de coût, seuls le terme conjoint de sparsité et le terme structurel de rang inférieur ont les paramètres de régularisation $\lambda_1$ et $\lambda_2$. Les résultats de la décomposition de matériaux sont clairement influencés par les paramètres de régularisation. Il s'agit en fait d'un problème persistant, puisque la résolution de la fonction de coût avec plus d'un paramètre de régularisation est encore un problème difficile [Clark and Badea, 2014,Gao et al., 2011,Zhang et al., 2016,Ding et al., 2018]. Les paramètres de régularisation scalaire $\lambda_1$ et $\lambda_2$ influencent respectivement leniveau de sparsité et de rang faible. Nous avons choisi les deux paramètres scalaires par validation croisée [Boyd et al., 2010]. Le paramètre Lagrangien augmenté $\tau$ qui est égal à la taille du pas de l'itération a aussi un impact évident sur la vitesse de convergence. En pratique, pour rendre les performances moins dépendantes du choix initial, nous avons mis à jour $\tau$ à chaque itération de la manière discutée dans [Boyd et al., 2010, WANG and LIAO, 2001] (essayez de garder les normes primaires et doubles résiduelles dans l'ADMM à l'intérieur d'un facteur car elles convergent toutes les deux vers zéro). Enfin, en raison de l'utilisation de la propriété locale, le choix des paramètres de régularisation $\lambda_1$, $\lambda_2$ et $\tau$ est également influencé par la taille du patch. En général, une taille de patch plus petite devrait avoir des paramètres de régularisation plus petits, sinon des erreurs évidentes se produiront près des bords des patchs dans les images de matériau décomposé. Il faut noter que ni les tailles trop grandes ni les tailles trop petites ne correspondent à la propriété locale ou n'entraînent une décomposition précise, et qu'elles doivent être réglées en fonction de la propriété de chaque donnée sCT.

En conclusion, la méthode de DSR proposée présente de bonnes performances dans la séparation et la quantification simultanées de deux agents de contraste, par exemple l'iode et le gadolinium. En particulier, la bonne capacité de la DSR à distinguer des agents de contraste similaires ($p.\ ex.$, l'iode, le gadolinium et le xénon) suggère son utilisation potentielle intéressante pour des applications industrielles et médicales. Dans le cadre des travaux futurs, il faudrait étudier plus à fond la propriété conjointe de sparsité et de faible rang structurel afin d'utiliser pleinement la propriété de sparsité et de faible rang cachée dans les données sCT. Enfin, une stratégie plus robuste pour le choix des paramètres de régularisation pourrait également être étudiée.

**Chapitre4**, intitulé " *ROI-Wise Material Decomposition in Spectral Photon-counting CT* ", cette méthode opère par région. Elle consiste à optimiser les matériaux de base en se basant sur la segmentation spatio-énergétique des régions d'intérêt (ROI—regions-of-interests) dans les images sCT, à réduire le bruit en faisant le moyennage des images spatiales multi-énergie, et à effectuer une décomposition fine des matériaux impli-

quant une matrice de décomposition optimisée, une régularisation du débruitage et une régularisation parcimonieuse. Les résultats sur des données numériques et physiques ont montré que la méthode proposée de décomposition des matériaux ROI par ROI (ROI-wise—region-of-interests-wise) présente une fiabilité et une précision nettement supérieures à celles des méthodes de décomposition courantes fondées sur la régularisation de la variation totale (TV) ou de la norme L1.

Pour rendre la décomposition de matériaux plus fiable et plus précise, nous proposons d'exploiter pleinement leur similitude spatio-énergétique dans ROIs des images sCT multi-énergie et de l'absence de corrélation inter-bandes et des caractéristiques du bruit dépendant du matériau dans les images sCT. Pour ce faire, nous effectuons une optimisation du matériau de base en réduisant l'impact de la similarité des matériaux par le biais d'une segmentation spatio-énergétique. En même temps, nous construisons une image composite à bruit réduit en introduisant un soi-disant moyennage d'énergie [Leng et al., 2011], dans lequel les images à différents bandes d'énergie sont mélangées mais le bruit est réduit. Une autre caractéristique du bruit dans le sCT est qu'il est dépendant du matériau, ce qui signifie que le bruit montre différents impacts sur les matériaux selon leurs catégories et leurs densités massiques. Par exemple, les matériaux semblables à l'eau (eau, poly(méthacrylate de méthyle) (PMMA) et tissu mou, *etc*.) avec des coefficients d'atténuation massique plus faibles et les matériaux avec des densités plus faibles sont beaucoup plus susceptibles à l'influence du bruit par rapport aux matériaux denses d'intérêt. Il a été montré dans [Ducros et al., 2017, Si-Mohamed et al., 2018] que les dilutions d'agents de contraste (*p. ex.*, iode, gadolinium et or, *etc*.) à plus faible concentration ont un rapport contraste/bruit plus faible. L'image composite à bruit réduit qui en résulte est alors utilisée dans la décomposition fine du matériau. Le diagramme global de la décomposition de matériaux par ROIs est illustré à la figure 9.

(1) *Basis material optimization*: L'optimisation des matériaux de base, qui est au cœur de notre décomposition de matériaux ROI par ROI, comprend deux étapes: la segmentation spatio-énergétique et la sélection des matériaux de base. La première étape vise à séparer les images spatiales reconstruites en différents ROI. La deuxième étape consiste à supprimer les matériaux de base non pertinents en utilisant une décomposition grossière des matériaux et un seuillage de la population relative.

Nous obtenons d'abord les ROI des images multi-énergie par segmentation spatio-énergétique, où chaque ROI représente une zone homogène contenant des matériaux similaires. Pour réaliser une telle segmentation spatio-énergétique, on utilise les caractéristiques morphologiques et spectrales des images multi-énergie. La figure 10 illustre la segmentation de deux ROI dans les images spatiales multi-énergie.

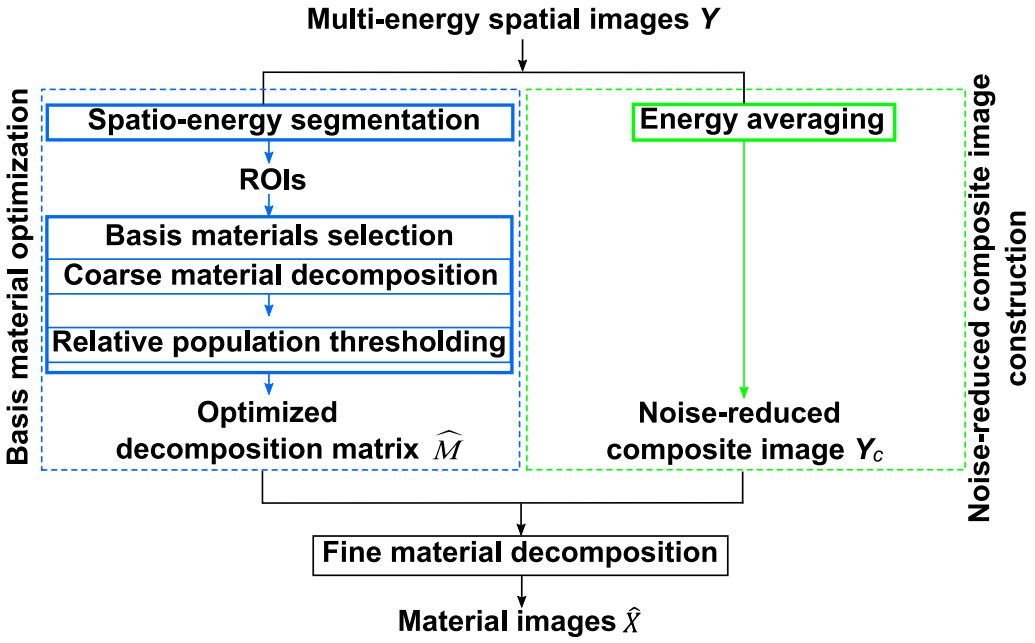


Figure 9: Diagramme de l'algorithme de décomposition de matériaux ROI par ROI. De haut en bas: la segmentation spatio-énergétique basée sur l'optimisation des matériaux de base (bleu) et la construction d'images composites à bruit réduit (vert), et la décomposition fine des matériaux.

Les caractéristiques spectrales sont extraites en regroupant les images sCT à toutes les énergies en une seule image tridimensionnelle (3-D) dans laquelle l'énergie est prise comme une troisième dimension. Chaque pixel de l'image 3-D a des valeurs multi-énergie (dépendant de l'énergie $\mu$). Les pixels ayant des courbes $\mu$ différentes, c.-à-d. des caractéristiques spectrales différentes, appartiennent à des ROIs différents, comme le montre la partie supérieure médiane de la figure 10. Les caractéristiques morphologiques des images sCT sont en fait dépendantes de l'énergie, car les caractéristiques des matériaux dans les images sCT sont dépendantes de l'énergie. Par conséquent, les structures imperceptibles à certains niveaux d'énergie peuvent être distinguées plus facilement à un autre niveau, en fonction des caractéristiques physiques des matériaux. Par conséquent, nous prenons les caractéristiques morphologiques de la bande d'énergie ayant la segmentation la plus fiable en évaluant une segmentation basée sur le modèle de mélange gaussien (GMM) à chaque bande d'énergie. Ensuite, les structures extraites sont traitées comme la contrainte commune pour les images de toutes les bandes d'énergie, comme le montre la partie inférieure et centrale de la figure 10, où $\boldsymbol{Y}_s$ désigne l'image multidimensionnelle contenant les structures communes. Les caractéristiques spectrales et morphologiques sont alors exploitées conjointement pour une segmentation basée

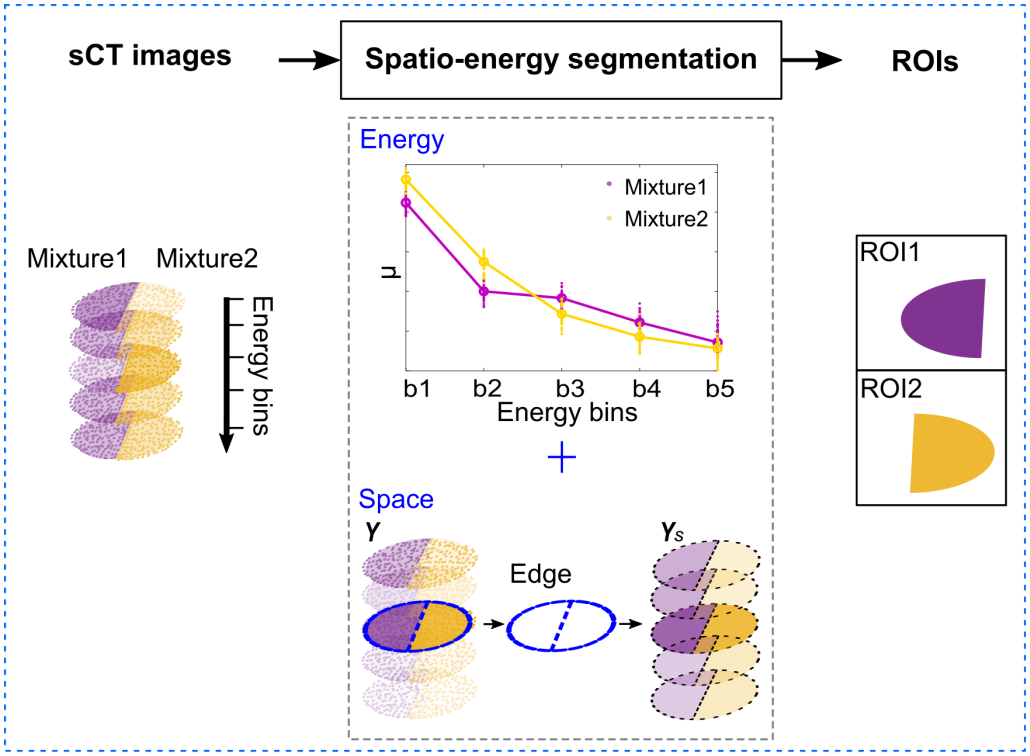


Figure 10: Diagramme de la segmentation spatio-énergétique. De gauche à droite: images spatiales multi-énergie contenant le mélange 1 et le mélange 2, la segmentation spatio-énergétique utilisant les caractéristiques spectrales (haut-moyen) et spatiales (bas-moyen), et les ROI segmentés.

sur le clustering.

La deuxième étape de l'optimisation des matériaux de base consiste à mettre à jour la matrice de décomposition initialisée selon le principe de maintenir le nombre minimum de matériaux de base nécessaires (par rapport à la vérité de terrain) tout en en excluant le plus grand nombre possible. Nous proposons une méthode de seuillage de population relative (RPT) pour déterminer quel matériau de base mérite d'être sélectionné. La méthode RPT est basée sur le pourcentage de population défini comme le rapport entre le nombre de pixels contenant certains matériaux décomposés $N_x$ et le nombre total de pixels $N_{ROI}$ dans chaque ROIs (c.-à-d. un pixel 'contient' un matériau signifie que la densité de masse décomposée de ce matériau est un nombre positif au pixel); seuls les matériaux dont le pourcentage est supérieur à un seuil $T$ seront préservés dans chaque ROI. La signification physique de la RPT est en partie impliquée dans la propriété locale susmentionnée dans les domaines spectral et morphologique. La propriété locale limite la distribution des matériaux de base, ce qui signifie qu'un pourcentage minimum de pop-

ulation correspondant doit exister pour tous les RPI. En d'autres termes, le seuil du pourcentage de population est associé au degré d'agrégation des matériaux.

Après optimisation des matériaux de base, nous obtenons un nouveau $\hat{\boldsymbol{M}}$ à partir de $\boldsymbol{M}$ dans le $k$-ième ROI.

(2) *Noise-reduced composite image construction*: Les bruits aux différentes bandes d'énergie sont indépendants lorsque l'effet de partage de charge du PCD peut être ignoré. Ainsi, en faisant la moyenne des images spatiales multi-énergie dans la dimension de l'énergie, on obtient une image composite où le bruit est réduit et l'information est mélangée.

(3) *Fine material decomposition*: La décomposition fine des matériaux est la dernière étape de la méthode proposée de décomposition de matériaux par ROI, qui fait intervenir trois termes: le terme de fidélité des données basé sur la matrice de décomposition optimisée $\hat{\boldsymbol{M}}$, le terme de régularisation du débruitage impliquant l'image composite à bruit réduit $\boldsymbol{Y}_c$, et le terme de régularisation de la sparsité.

En particulier, le terme de régularisation du débruitage est consacré à l'exploitation de l'absence de corrélation inter-bin et des caractéristiques du bruit dépendant du matériau dans les images sCT possédant la présence du symbole $\boldsymbol{Y}_c$. Pour éviter que des matériaux ressemblant à de l'eau (*p. ex.* eau, PMMA et tissus mous, *etc.*) ne dégradent les matériaux d'intérêt (*p. ex.* agents de contraste), nous proposons d'utiliser l'image composite à bruit réduit $\boldsymbol{Y}_c$.

La performance de la méthode proposée de décomposition de matériaux ROI par ROI a été évaluée sur des données de fantômes numériques et physiques. Les fantômes numériques et physiques sont les mêmes que ceux de la section 2. Deux autres méthodes ont été comparées à la méthode proposée de décomposition de matériaux par ROI: (a) la méthode la variation totale (TV); (b) la méthode grossière (Coarse). Il est à noter que la méthode " Coarse " est également une étape intermédiaire de la méthode par ROI, qui peut être utilisée pour évaluer les impacts de l'optimisation des matériaux de base et du débruitage basé sur le calcul de la moyenne énergétique. Pour plus de clarté, nous indiquons la décomposition de matériaux proposée par la méthode de ROI dans les figures.

Les résultats de la décomposition de quatre matériaux de base (eau, fer, iode et gadolinium) sont présentés dans la Fig. 11. Contrairement aux deux autres méthodes, la méthode proposée de décomposition de matériaux par ROI montre une meilleure capacité de détection en termes de performance de préservation des bords.

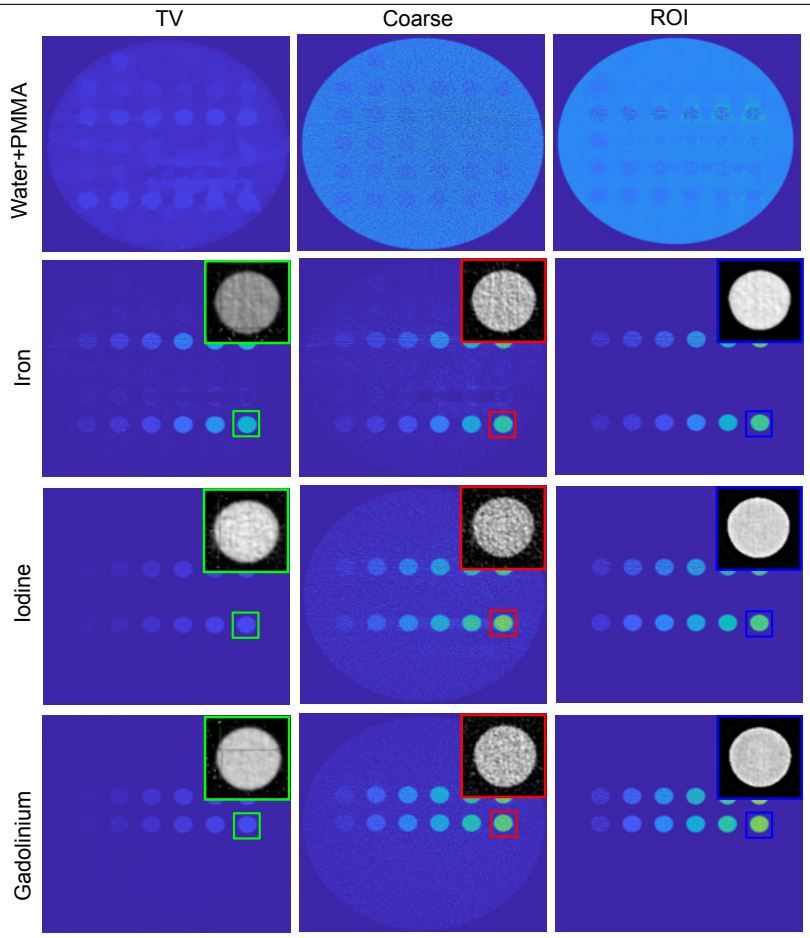


Figure 11: Les résultats de la décomposition de matériaux à l'aide de trois méthodes sur le fantôme numérique. De gauche à droite: Décompositions TV, Coarse et ROI.

Visuellement, il y a évidemment plus d'erreurs pour les matériaux semblables à l'eau que pour le fer, l'iode et le gadolinium. Heureusement, dans les applications pratiques, les informations quantitatives des trois derniers matériaux sont plus utiles, ce qui nous permet de porter une plus grande attention aux matériaux d'intérêt: le fer, l'iode et le gadolinium. A titre d'illustration, nous traçons les matériaux décomposés de chaque disque et la régression linéaire correspondante dans la Fig. 12. Il est évident que seuls les résultats de la méthode par ROI sont toujours sous-déterminés pour tous les matériaux, ce qui signifie une sorte de fiabilité supérieure.

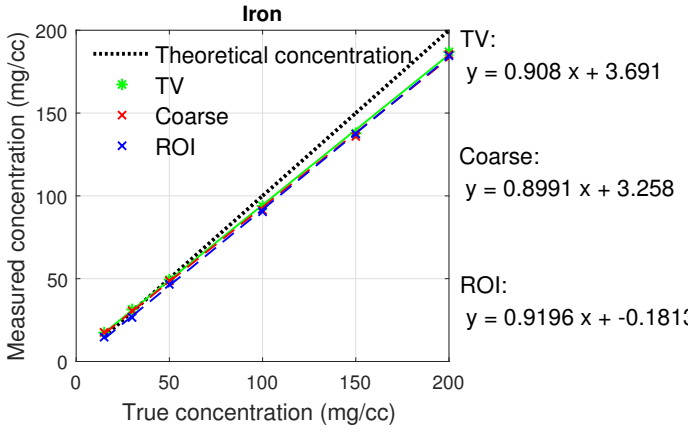


(a)

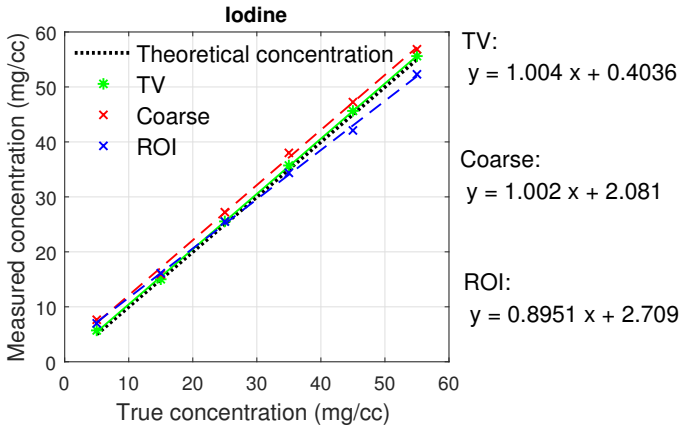


(b)

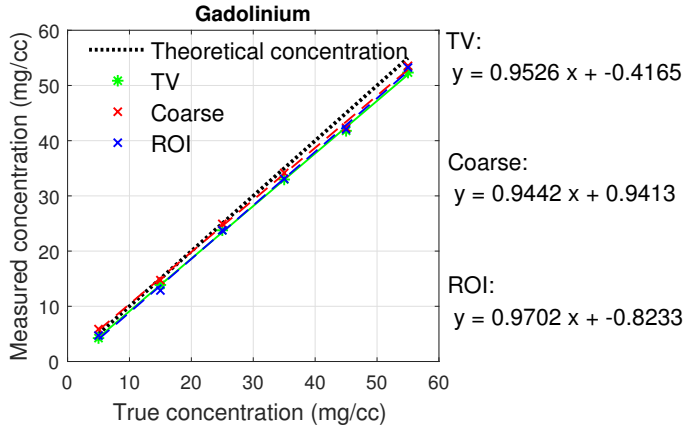


(c)

Figure 12: Les régressions linéaires de la décomposition de matériaux en utilisant trois méthodes pour (a) le fer, (b) l'iode et (c) le gadolinium.

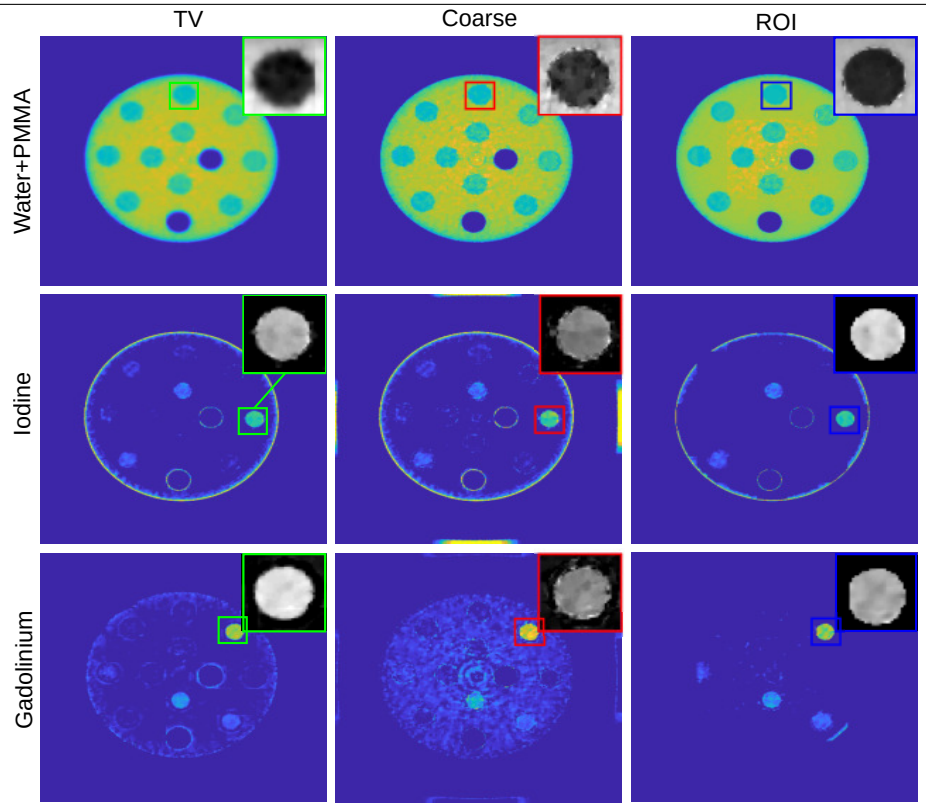


Figure 13: Les résultats de la décomposition de matériaux sur le fantôme physique en utilisant trois méthodes. De gauche à droite: décompositions TV, Coarse et ROI.

Les résultats de la décomposition de la matériaux sur le fantôme physique sont illustrés dans la figure 13. La méthode proposée est nettement plus performante en matière de détection et de quantification que les méthodes TV et Coarse. Notre méthode montre une bien meilleure précision morphologique, même pour les matériaux semblables à l'eau. Comme on l'a observé, aucune des trois méthodes n'a décomposé avec précision l'iode à une concentration de 1 $mg/cc$. Par exemple, la méthode par ROI n'a pas pu reconnaître l'iode à l'intérieur du disque, alors que les deux autres méthodes n'ont pas pu séparer l'iode avec de l'eau ou du gadolinium de 2 $mg/cc$.

Pour les données in vivo, les résultats de décomposition des différentes méthodes sont présentés dans la Fig. 14. Notons que le calcium (Ca) dans la colonne vertébrale est décomposé sur la base de matériau iode, en raison de leur similitude de coefficients d'atténuation de masse dans notre réglage des seuils d'énergie. Pour le gadolinium, bien que la vérité de base soit inconnue dans les données in vivo, des tubes de dilutions de gadolinium à proximité du lapin ont été évalués alternativement. Clairement, les méthodes SVD et L1 montrent plus de bruit pour l'iode et le gadolinium. Au contraire, la méthode DSR proposée a une meilleure capacité de détection pour l'iode et le gadolin-

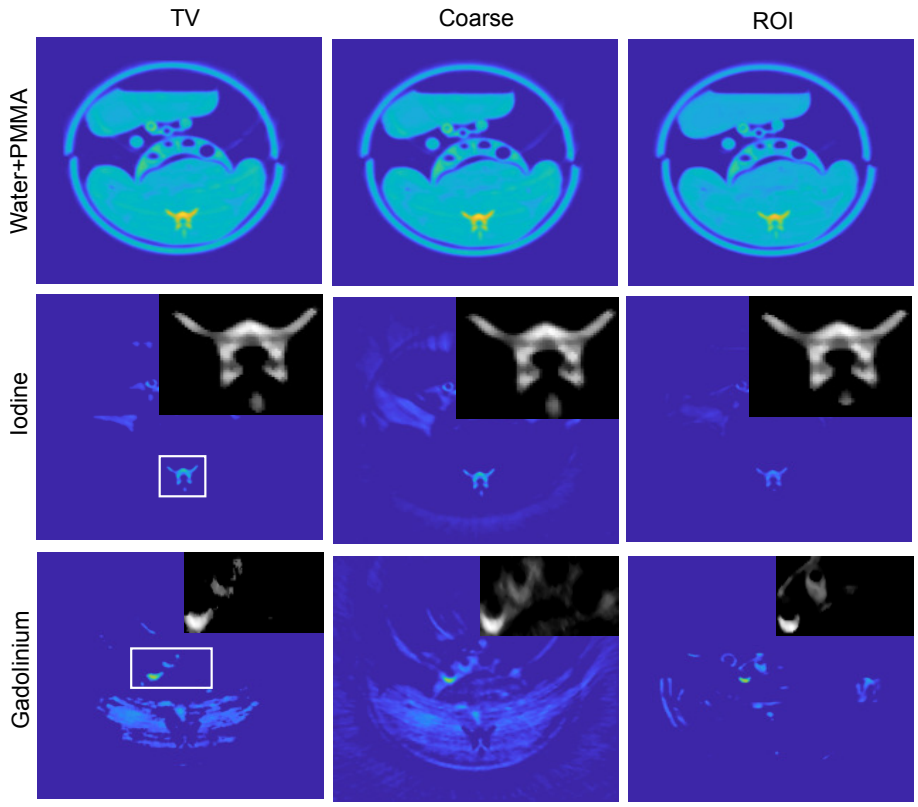


Figure 14: Les résultats de la décomposition de matériaux sur la base du fantôme physique. De gauche à droite: Pseudo-inverse avec TV, Coarse et ROI.

ium, surtout pour le gadolinium.

Nous avons proposé une méthode de décomposition de matériaux ROI par ROI. La méthode proposée permet de décomposer les matériaux de manière plus fiable et plus précise. Ceci est principalement dû à l'introduction de la segmentation spatio-spectrale qui permet d'extraire les caractéristiques pertinentes codées dans les images sCT multi-énergie pour l'optimisation des matériaux de base.

Les résultats montrent que la méthode de décomposition de matériaux par ROI favorise une plus grande fiabilité, alors que la sensibilité de la détection des matériaux est quelque peu sacrifiée en contrepartie. Cela peut expliquer en partie pourquoi seuls les matériaux ayant une concentration supérieure à une certaine limite ont pu être décomposés avec précision. C'est le cas de l'iode avec une concentration de 1 $mg/cc$ par rapport à des concentrations plus élevées (Fig. 13).

En fait, le compromis entre la sensibilité et la fiabilité de la méthode proposée en termes de ROI est régularisé par le seuil $T$ dans le seuillage de la population relative. Un $T$ trop petit ou trop grand a induit l'augmentation des erreurs de décomposition, car un $T$ plus petit entraîne une fiabilité médiocre (mais une sensibilité élevée). En d'autres

termes, lorsque $T$ est trop petit, le bruit et les erreurs de reconstruction auront un fort impact sur la précision de la décomposition. A l'inverse, un $T$ excessif dégradera la capacité de décomposition pour les matériaux de faible concentration. Heureusement, les résultats montrent une fourchette relativement large pour le choix de $T$ autour de la valeur optimale, ce qui implique que la méthode proposée est relativement peu sensible à $T$.

Enfin, il convient de noter que la qualité de la reconstruction de l'image a une influence considérable sur la performance de la décomposition de matériaux dans le domaine de l'image. En raison de la dose excessivement faible allouée aux détecteurs, la reconstruction par CT à chaque bande d'énergie est un problème de reconstruction par CT à faible dose, qui est également un problème difficile. Une qualité de reconstruction d'image plus mauvaise peut détériorer la performance de la segmentation du ROI, ce qui en retour peut influencer la précision de la méthode par ROI, particulièrement pour les images avec de petites structures ($p.ex.$ petits vaisseaux sanguins). Nous avons choisi un algorithme commun mais efficace dans le domaine de la reconstruction par CT à faible dose (SART-TV) pour reconstruire les images du sCT. Cependant, les résultats de la reconstruction montrent encore des artefacts et du bruit évidents. Néanmoins, même dans cette situation, les matériaux étaient encore correctement décomposés sur les fantômes numériques et physiques, ce qui démontre la robustesse et la fiabilité de la méthode proposée en termes de ROI.

En conclusion, nous avons proposé une méthode de décomposition de matériaux ROI par ROI pour le sCT en optimisant conjointement les matériaux de base et en réduisant le bruit. Ceci est réalisé par la segmentation spatio-énergétique et l'exploitation des informations morphologiques et spectrales dans les images sCT. Les résultats sur les fantômes numériques et physiques ont montré que la méthode de décomposition de matériaux ROI par ROI présente une précision et une fiabilité nettement supérieures à celles des méthodes de décomposition courantes basées sur la TV ou la régularisation *lasso*. Dans les travaux futurs, la capacité de détecter des matériaux à faible concentration sera étudiée plus en détail afin d'améliorer la sensibilité de la méthode tout en maintenant la fiabilité. Entre-temps, la capacité d'identifier de petites structures ayant une faible concentration de matériaux sera également étudiée.

**Chapitre5**, intitulé " *Super-Energy-Resolution Material Decomposition in Spectral Photon-counting CT Using Pixel-wise Learning* ", nous proposons la notion d'imagerie sCT à super-résolution énergétique (SER—super-energy-resolution), qui est réalisée en établissant la relation entre la simulation et les fantômes physiques au moyen d'un apprentissage par dictionnaire couplé, de manière pixel par pixel. L'efficacité de ces méthodes proposées a été validée sur des données de fantômes numériques, de fantômes physiques et in

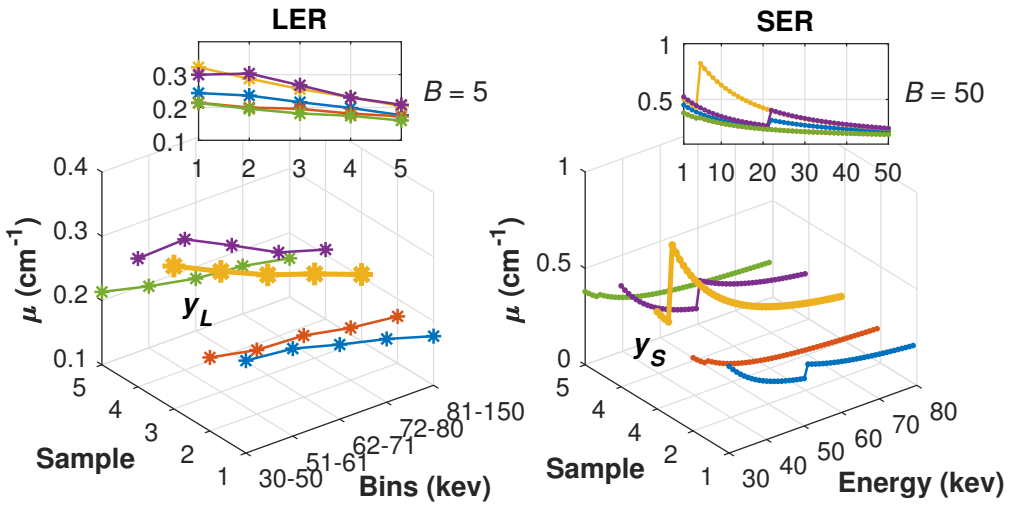


Figure 15: Coefficients d'atténuation linéaires: LER (gauche) et SER (droite). Les courbes de couleurs différentes indiquent des pixels différents; les pixels LER et SER correspondants ont la même couleur.

vivo. Les résultats montrent que, pour la même méthode de décomposition de matériaux utilisant la régularisation par lasso, l'imagerie à super-résolution énergétique proposée présente une précision de décomposition et un pouvoir de détection beaucoup plus élevs que ce que peut fournir la machine sCT actuelle.

Nous proposons d'améliorer la résolution de l'énergie restreinte en exploitant pleinement les fantômes de simulation et les fantômes physiques. Pour ce faire, l'imagerie à SER est introduite dans le sCT.

Les images SER sont des images virtuelles multi-énergie avec beaucoup plus de bandes mais sans bruit par rapport aux images sCT réelles. La figure 15 illustre la relation entre le sCT réelle, désignée par l'imagerie à basse résolution énergétique (LER—low-energy-resolution) dans le présent manuscrit, et l'imagerie SER en traçant respectivement les valeurs multi-énergétiques des pixels correspondants dans les images LER et SER. Pour un pixel dans les images LER reconstruites ($p.\ ex.$ astérisques jaunes à gauche de la Fig. 15, désignés par $\boldsymbol{y_L} \in \mathcal{R}^{B_L}$), il a 5 dimensions pour 5 bandes d'énergie, c.-à-d. $B_L = 5$. Alors que pour le pixel SER correspondant (points jaunes à droite de la Fig. 15, désigné par $\boldsymbol{y_S} \in \mathcal{R}^{B_S}$), il peut avoir des dimensions beaucoup plus élevées, $p.\ ex.$ 50 dimensions pour $B_S = 50$ (30 - 80 keV). Notons que la raison du réglage de 50-bins consiste en ce que le $\mu_m$ le plus précis que nous pouvons obtenir du NIST (National Institute of Standards and Technology) est celui avec l'intervalle de 1 keV [Saloman and Hubbell, 1986].

L'imagerie SER proposée est réalisée en introduisant l'hypothèse que si elle contient les mêmes matériaux de base et les mêmes concentrations, la correspondance entre les

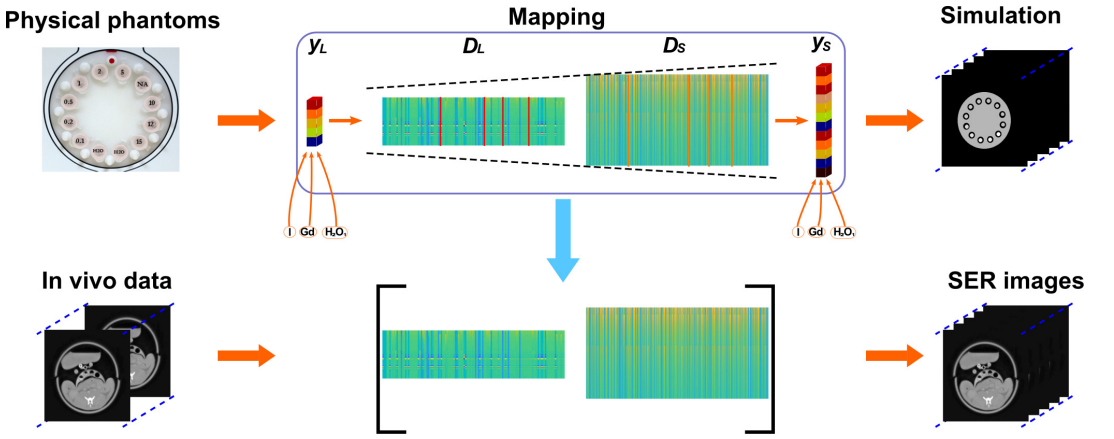


Figure 16: Illustration de l'imagerie du sCT basée sur la SER.

images LER et SER est déterminée et peut être apprise. On le réalise en apprenant la relation entre les fantômes physiques et les données de simulation, puis en l'appliquant à d'autres données physiques, comme l'illustre la Fig. 16. Les fantômes physiques sont mesurés et reconstruits en images LER, tandis que les versions SER correspondantes sont produites par simulation avec les mêmes formes et composants mais avec plus de bandes. Ensuite, les caractéristiques spectrales LER et SER sont extraites et leur relation sera apprise par une cartographie qui peut être utilisée pour synthétiser les images SER pour d'autres données in vivo.

(1) *SER image synthesis based on coupled dictionary learning*: Nous apprenons la correspondance entre les caractéristiques spectrales LER et SER en utilisant la méthode d'apprentissage par dictionnaire couplé (coupled dictionary learning—CDL) au niveau du pixel.

Il est inefficace d'apprendre directement la correspondance à partir de l'ensemble des images ou des patchs LER et SER en raison d'informations supplémentaires sur la morphologie et le spectre. En général, l'apprentissage des caractéristiques morphologiques de certains organes est un autre défi qui exige des images abondantes avec diverses informations spatiales. Nous le résolvons en apprenant la correspondance des paires de pixels LER et SER, plutôt que les images entières ou les patchs. Avec cette stratégie, les échantillons d'entraînement ne contiennent que des informations spectrales. En conséquence, les fantômes physiques utilisés dans notre travail peuvent avoir des formes simples, mais des composants matériels abondants.

La CDL est généralement utilisée dans le domaine de la super résolution spatiale [Yang et al., 2010,Wang et al., 2012,Hu et al., 2018]. Dans la théorie de l'apprentissage par dictionnaire, les caractéristiques d'un pixel $\boldsymbol{y}$ peuvent être représentées comme

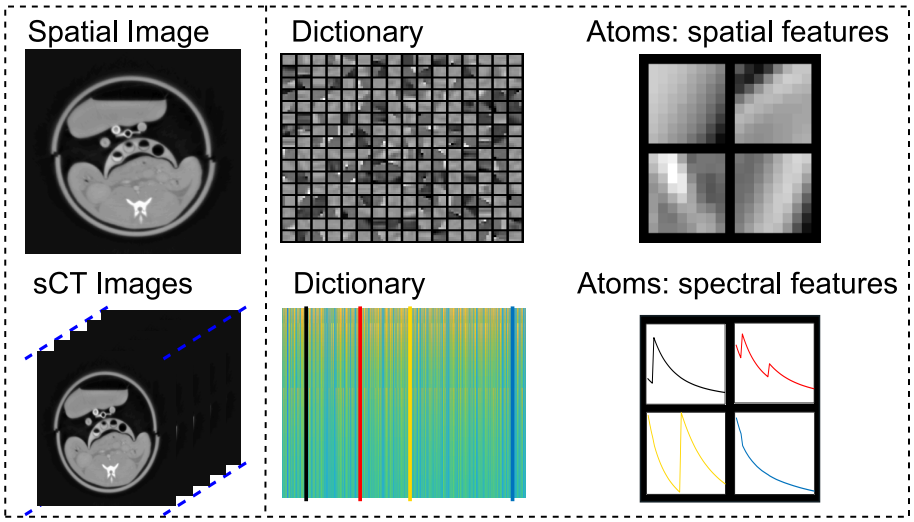


Figure 17: Caractéristiques apprises avec la méthode d'apprentissage par dictionnaire pour la super résolution spatiale et la super résolution énergétique. Notons que le dictionnaire pour les images sCT (en bas) est le dictionnaire SER.

une combinaison parcimonieuse d'atomes à l'intérieur d'un dictionnaire surcomplet $\boldsymbol{D}$.

Il est à noter que les atomes des dictionnaires appris à l'aide d'une stratégie par pixel sont dépendants de l'énergie, plutôt que des caractéristiques spatiales dans les applications traditionnelles de super-résolution spatiale. La figure 17 illustre la différence entre la super résolution spatiale et la super résolution énergétique en montrant les caractéristiques apprises. Les atomes appris à partir d'une image spatiale sont des caractéristiques morphologiques. Alors que pour la SER, les atomes du dictionnaire sont dépendants de l'énergie et ressemblent plus à des courbes $\mu$.

(2) *Material decomposition using SER images*: Les images SER synthétisées sont ensuite utilisées pour la décomposition des matériaux dans le domaine de l'image. Une matrice de décomposition plus précise $\boldsymbol{M}$ adaptée aux images SER est alors nécessaire. Pour le LER, $\boldsymbol{\mu_m}$ de chaque matériau de base (colonne à l'intérieur de $\boldsymbol{M}$ dans l'équation (5.2) désignée comme $\boldsymbol{M_L}$) est une valeur effective sur les bandes d'énergie $B_L$. En revanche, $\boldsymbol{M}$ pour SER (désigné par $\boldsymbol{M_S}$) a beaucoup plus de bandes, $p.\,ex.$ $B_S = 50$. Chaque colonne à l'intérieur de $\boldsymbol{M_S}$ est la valeur la plus précise directement récupérée du NIST, comme illustré dans la Fig. 18.

La performance de la méthode proposée de décomposition de matériaux ROI par ROI a été évaluée sur des données de fantômes numériques et physiques. Nous présentons ici principalement les résultats des expériences physiques.

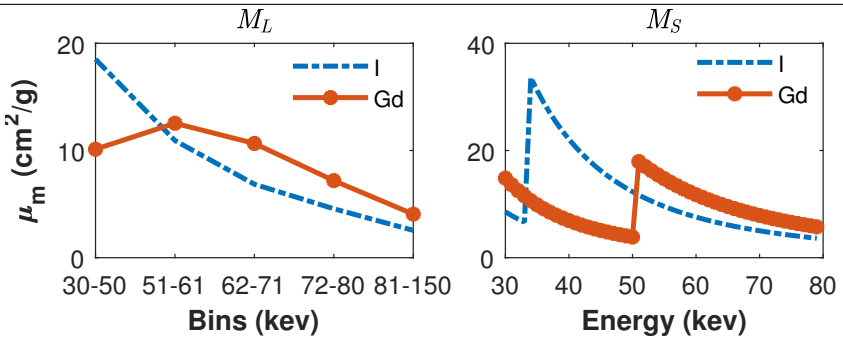


Figure 18: Coefficients d'atténuation massique en $\boldsymbol{M_L}$ et $\boldsymbol{M_S}$ pour l'iode et le gadolinium.

Les expériences physiques ont été réalisées sur un sCT prototype Philips [Si-Mohamed et al., 2018, Cormode et al., 2017]. Les données de projection ont été obtenues avec une tension de tube de 120 kVp et un courant de 220 mA. L'indice de dose volumétrique du CT ($CTDI_{vol}$) était de 22,2 mGy. Le balayage consiste en 2400 projections; chaque projection a 924 rayons; chaque rayon contient 5 bandes d'énergie. Les seuils d'énergie du sCT sont les mêmes pour toutes les données physiques de ce travail: 30, 51, 62, 72, 81 keV.

La performance de la méthode proposée de décomposition de matériaux basée sur la SER a été évaluée à la fois sur les données des fantômes physiques et sur les données in vivo. Les fantômes physiques sont représentés sur la figure 19a, dont les images sont le gadolinium reconstruit à un seul emplacement. Le fantôme supérieur sans grand anneau est destiné à l'entraînement, tandis que le fantôme inférieur avec grand anneau est destiné aux tests. Les images sCT du fantôme avec grand anneau présentent un bruit quantique plus fort et plus d'artéfacts, car moins de photons peuvent traverser le fantôme et être détectés. Des tubes amovibles contenant différentes dilutions d'iode ou de gadolinium sont insérés au centre des fantômes, comme le montre la Fig. 19b. Le numéro sur chaque disque fait référence à la concentration (mg/cc) qui couvre de 0.1 $mg/cc$ à 15 $mg/cc$. Dans nos expériences, l'iode (I) et le gadolinium (Gd) ont été mesurés pour l'entraînement et les tests.

Les résultats de la décomposition de matériaux des fantômes physiques à gros anneau sont présentés dans la figure 20. Contrairement à la méthode LER, la méthode SER proposée présente de meilleures performances en matière de quantification et de détection par rapport à la méthode LER. Premièrement, la méthode SER proposée donne une bien meilleure précision morphologique en termes de performance de préservation des bords et beaucoup moins de bruit, même pour les matériaux à faible concentration, par exemple 0.5 mg/cc pour l'iode et le gadolinium. Les arêtes sont substantiellement préservées par la méthode SER. Alors que pour la méthode LER, les zones sélectionnées des matériaux

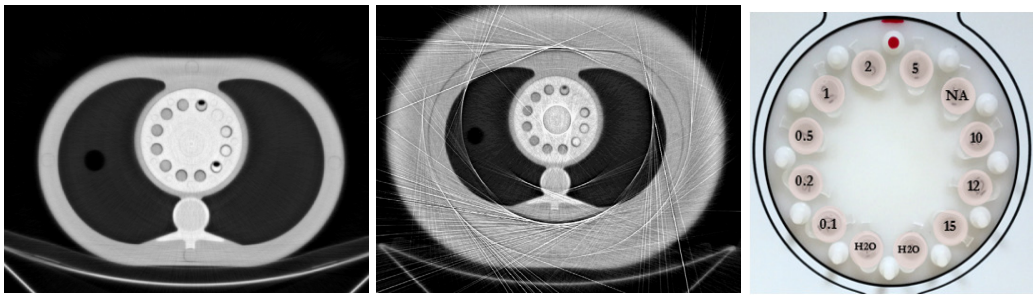


(a) (b)

Figure 19: (a) Fantômes physiques sans (gauche) et avec (droite) gros anneau: gadolinium au 4ème bande; (b) inserts: les étiquettes font référence à la concentration nominale présente dans chaque tube (mg/cc).

à faible concentration sont submergées par le bruit et ne peuvent pas être détectées.

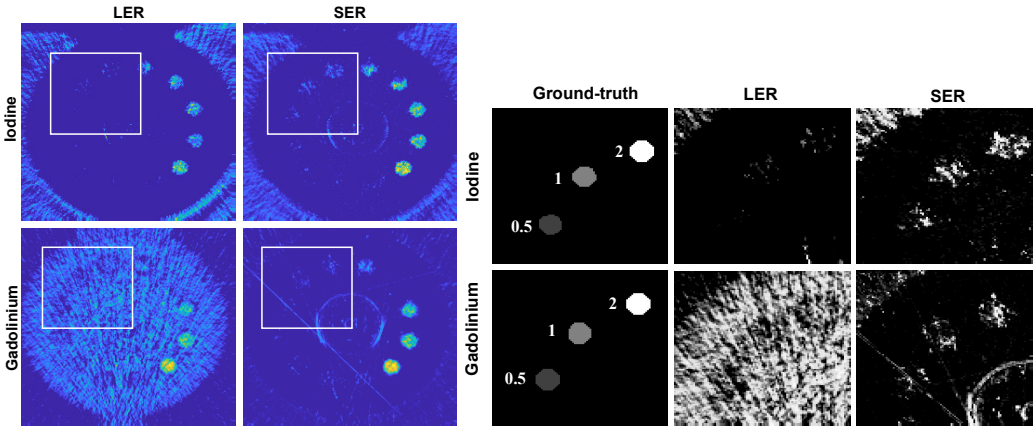


(a) (b)

Figure 20: (a) Les résultats des différentes méthodes de décomposition de matériaux sur les fantômes physiques dans les essais; (b) les ROIs en (a) pour les matériaux à faible concentration. Les étiquettes des ROI se rapportent à la concentration nominale présente dans chaque tube (mg/cc).

Deuxièmement, de façon plus quantitative, comme le montre la figure 21, les régressions linéaires de I et Gd illustrent que la méthode basée sur le SER a des erreurs beaucoup plus faibles. La méthode SER a une pente plus précise (pour l'iode: $a_{\mathrm{LER}} = 1.241$ et $a_{\mathrm{SER}} = 0.87$; pour le gadolinium: $a_{\mathrm{LER}} = 0.63$ et $a_{\mathrm{SER}} = 0.94$) et la valeur de l'ordonnée à l'origine (pour l'iode: $b_{\mathrm{LER}} = 3.28$ et $b_{\mathrm{SER}} = -0.09$; pour le gadolinium: $b_{\mathrm{LER}} = 2.08$ et $b_{\mathrm{SER}} = -0.51$).

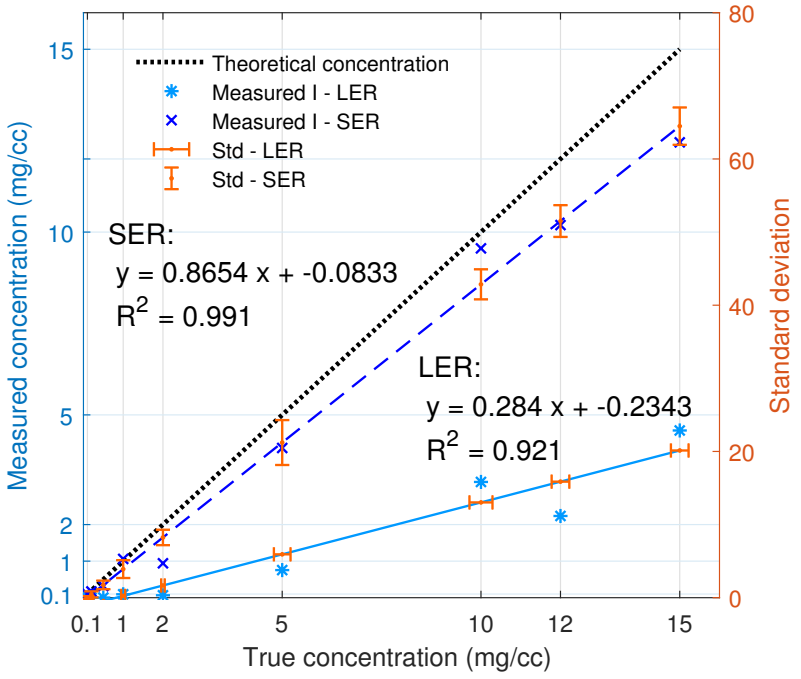


(a)

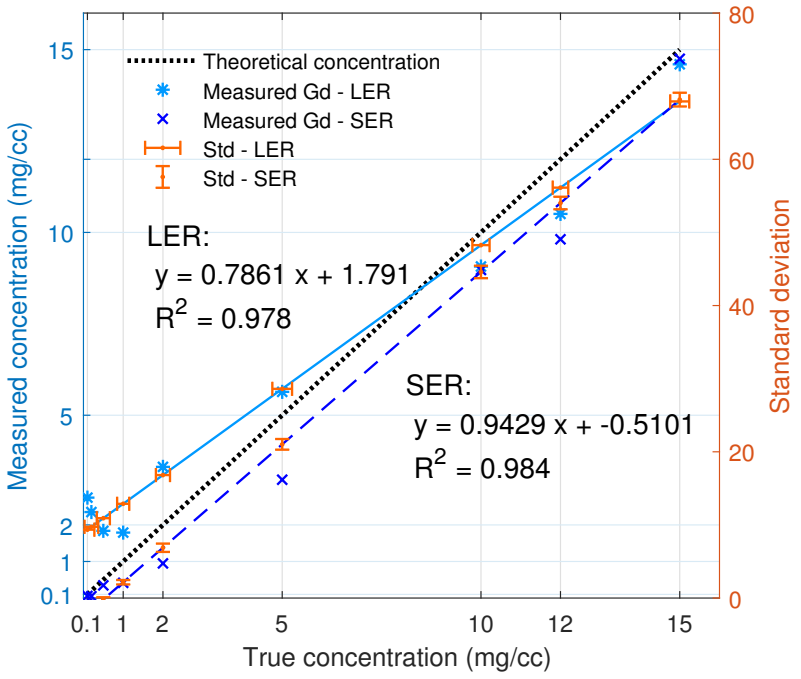


(b)

Figure 21: Les régressions linéaires de (a) l'iode et (b) du gadolinium pour différentes méthodes de décomposition des matériaux dans les essais : modèle de régression linéaire, R au carré ($R^2$) et écart-type (std).

En même temps, les résultats de décomposition des différentes méthodes sur les données in vivo sont présentés dans la figure 22. Notons que le calcium (Ca) dans la colonne vertébrale est décomposé sur la base de l'iode du matériau, en raison de leur similitude de coefficients d'atténuation de masse dans notre réglage des seuils d'énergie. Pour le gadolinium, bien que la vérité de terrain soit inconnue dans les données in vivo, des tubes de dilutions de gadolinium à proximité du lapin ont été évalués alternativement. Comme observé, la méthode LER ne peut pas séparer le gadolinium de l'iode et a plus de bruit pour l'iode et le gadolinium. Au contraire, la méthode SER proposée a une meilleure capacité de détection à la fois pour l'iode et le gadolinium, où l'iode est présent dans la colonne vertébrale et le gadolinium dans les tubes et les organes.

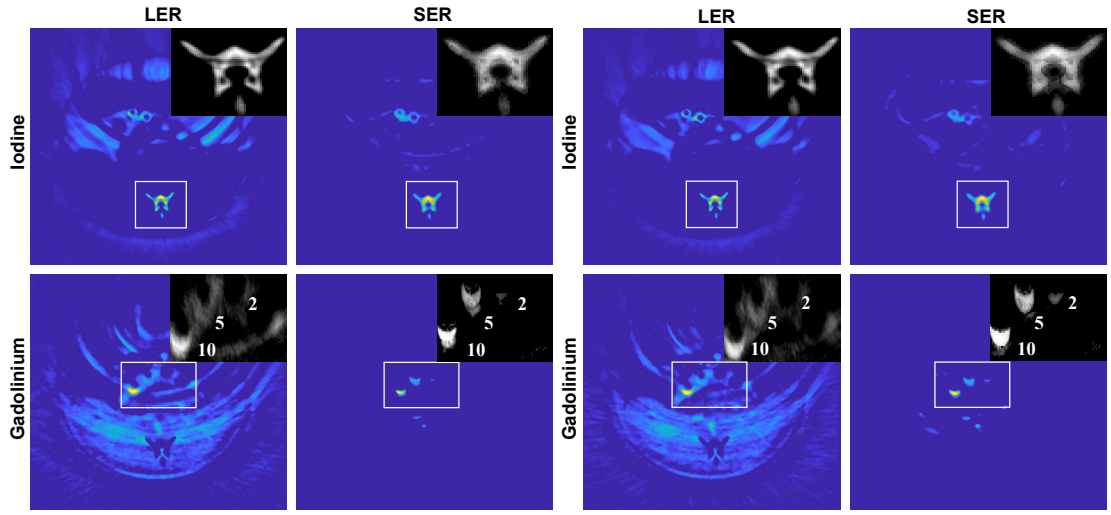


Figure 22: Les résultats des différentes méthodes de décomposition de matériaux sur les données in vivo dans les essais: a) 5 min après l'injection d'agents de contraste; b) 15 min après. Il est à noter que le calcium de la colonne vertébrale est décomposé sur la base de l'iode et que la base de gadolinium se trouve dans les tubes et les organes.

Notre objectif principal est d'améliorer la résolution en énergie du sCT afin d'améliorer la précision de la décomposition et la capacité de détection. Pour y parvenir, nous avons proposé une imagerie SER en exploitant pleinement les abondantes caractéristiques spectrales intégrées dans les fantômes de simulation et les fantômes physiques. Les résultats préliminaires ont révélé que la méthode SER proposée permet une décomposition précise et une grande capacité de détection, même pour les matériaux à faible concentration.

La méthode de décomposition de matériaux basée sur le SER est fiable. Tout d'abord, même dans des conditions plus bruyantes que l'entraînement, la méthode SER proposée permet une grande précision de décomposition et une grande capacité de détection. Dans

nos expériences, nous avons entraîné les dictionnaires sur les fantômes sans grand anneau, mais testé sur ceux avec grand anneau qui ont plus de bruit et d'artefacts. Cependant, les résultats montrent toujours une meilleure précision de décomposition et une meilleure capacité de détection par rapport à la méthode LER, en particulier pour l'iode. Deuxièmement, la décomposition précise des données in vivo polluées par le mouvement (5 min après l'injection) illustre également la fiabilité de notre méthode. De plus, les résultats de la décomposition de l'iode et du gadolinium sont toujours sous-estimés pour presque toutes les concentrations.

Chaque image de SER synthétisée est une image monochromatique virtuelle. En fait, pour DECT, il existe une méthode d'imagerie similaire mais différente appelée image monochromatique virtuelle (mono-E ou VMS) [Iyama et al., 2018, Matsumoto et al., 2011] qui vise à améliorer la visibilité de l'agent de contraste. Une image mono-E est généralement reconstruite à partir d'une paire d'images de matériaux de base décomposés (par exemple, un matériau de base semblable à un tissu mou et un agent de contraste) en DECT [Wu et al., 2016, McCollough et al., 2015]. La performance du mono-E est déterminée par la décomposition de matériaux qui est traitée uniquement sur les images réelles (images LER dans le travail présent). En revanche, les images LER sont directement synthétisées en utilisant les caractéristiques spectrales apprises à la fois des fantômes de simulation et des fantômes physiques. Par conséquent, notre méthode peut être considérée comme une nouvelle imagerie mono-E précise.

En conclusion, nous avons proposé une imagerie SER pour améliorer la résolution en énergie du sCT. Pour ce faire, nous apprenons à établir une correspondance entre la simulation et les fantômes physiques au niveau du pixel et nous l'appliquons à d'autres données physiques. Les résultats sur les fantômes physiques et les données in vivo ont montré que la méthode de décomposition de matériaux basée sur le SER présente une décomposition de matériaux et une capacité de détection nettement plus précises que la méthode basée sur le LER. Dans les travaux futurs, la performance d'autres méthodes de décomposition de domaine d'image utilisant des images SER sera étudiée.

# General Introduction

## Problem statement and objective

In 1971, Godfrey Hounsfield built the first X-ray computed tomography (CT) system. His co-inventor Allan McLeod Cormack, a few years earlier, had used the Radon transform and its inverse to theoretically describe a radiological x-ray scanning machine and image reconstruction method. For their research, Cormack and Hounsfield received the 1979 Nobel Prize in Physiology or Medicine.

Currently, conventional CT is a widely used x-ray scanning technique in both clinical and industrial areas. It provides answers to urgent diagnostic tasks such as oncology tumor staging, acute stroke analysis, or radiation therapy planning and industrial missions such as quality analysis and luggage scanning.

Dual-energy methods for CT (DECT) were subsequently investigated by Alvarez and Macovski in 1976 [Alvarez and Macovski, 1976, Macovski et al., 1976]. DECT devices were enabled to gain information on the energy-dependent (i.e., spectral but only two) attenuation properties of the object. Different technical realizations were employed. The straightforward solution is the so-called dual-kVp technique. Two CT scans with different x-ray tube acceleration voltages are performed. The two resulting data sets contain information on the spectral x-ray attenuation characteristics of the object. These spectral data can be used to obtain additional information on the object. Nevertheless, DECT systems only perform a two-point analysis of the X-ray attenuation, which improves tissue characterization and allows quite precise iodine quantification, but is insufficient to simultaneously discriminate between iodine and gadolinium, especially at low radiation dose [Si-Mohamed et al., 2017a]. In addition, many DECT systems expose the patient to two energy beams that can result in potentially high radiation exposure, and motion can create issues for aligning the two datasets.

Spectral CT (sCT) or multi-energy has recently received increasingly intensive attention, due to the new advances in photon-counting detector (PCD) technology. Compared to conventional energy integrating CT or DECT, spectral CT can count the number of photons in separated energy bins with one single exposure [Taguchi and Iwanczyk,

2013, Faby et al., 2015]. In this way, multiple materials can be simultaneously identified. A number of material decomposition methods have been reported and different experimental systems are under development for spectral CT. However, most researches focus on the imaging of contrast agents with high atomic numbers ($Z$ number), such as iodine, gadolinium and gold, which have unique K-edges within detection energy range. It is much more difficult to distinguish those having low atomic numbers, especially when their $Z$ numbers are close.

Targeting on medical application of spectral CT, our objective is to develop material decomposition methods to improve the performance of material decomposition, *e.g.* accuracy and reliability, *etc.*

## Main contributions

The main contributions of this thesis include: the proposal of new material decomposition methods, the validation and assessment of the proposed methods through both simulated and physical sCT data. In the following, we detail the contributions in the three aspects:

- Material Decomposition in X-ray Spectral CT Using Multiple Constraints in Image Domain (Chapter 3).

  X-ray spectral CT appears as a new promising imaging modality for the quantitative measurement of materials in an object, compared to conventional energy-integrating CT or dual energy CT. We consider material decomposition in spectral CT as an overcomplete ill-conditioned inverse problem. To solve the problem, we make full use of multi-dimensional nature and high correlation of multi-energy data and spatially neighboring pixels in spectral CT. Meanwhile, we also exploit the fact that material mass density has limited value. The material decomposition is then achieved by using bounded mass density, local joint sparsity and structural low-rank (DSR) in image domain. The results on numerical phantom demonstrate that the proposed DSR method leads to more accurate decomposition than usual pseudo-inverse method with singular value decomposition (SVD) and current popular sparse regularization method with L1-norm constraint.

- ROI-Wise Material Decomposition in Spectral Photon-counting CT (Chapter 4).

  Spectral photon-counting X-ray CT (sCT) opens up new possibilities for the quantitative measurement of materials in an object, compared to conventional energy-integrating CT or dual energy CT. However, achieving reliable and accurate mate-

rial decomposition in sCT is extremely challenging, due to photon-counting detector limitations and interference between different basis materials. To cope with that, we propose a novel material decomposition method that works in a region-wise manner. The method consists in optimizing basis materials based on spatio-energy segmentation of regions-of-interests (ROIs) in sCT images, reducing noise by averaging multi-energy spatial images, and performing a fine material decomposition involving optimized decomposition matrix, denoising regularization and sparsity regularization. The effectiveness of the proposed method was validated on both digital and physical data. The results showed that the proposed ROI-wise material decomposition method presents clearly higher reliability and accuracy compared to common decomposition methods based on total variation (TV) or L1-norm (lasso) regularization.

- Super energy resolution based material decomposition in spectral CT (Chapter 5).

  Spectral photon-counting X-ray CT (sCT) offers new possibilities for the quantitative decomposition of materials in an object, compared to conventional energy-integrating CT or dual-energy CT. However, achieving accurate material decomposition, especially for low-concentration materials, is still extremely challenging for current sCT, due to restricted energy resolution stemming from the trade-off between the number of energy bins and undesired factors such as random noise. We propose to improve material decomposition by introducing the notion of super-energy-resolution in sCT. The super-energy-resolution material decomposition consists in learning the relationship between simulation and physical phantoms. To this end, a coupled dictionary learning method is utilized to learn such relationship in a pixel-wise way. The results on both physical phantoms and in vivo data showed that for the same decomposition method using lasso regularization, the proposed super-energy-resolution method achieves much higher decomposition accuracy and detection ability compared to physical sCT imaging.

## Organization of thesis

The thesis manuscript is organized as follows:

In Chapter 1, entitled "**Principles of Spectral CT**", the principles of common X-ray CT are introduced, including X-ray source and interacting of X-ray with materials; the principle of different detectors for different X-ray CT are introduced, including conventional energy integrated CT, dual-energy CT and spectral CT; the applications of the new spectral CT are introduced.

In Chapter 2, entitled "**Models of Material Decomposition and Mathematical Foundations**", a review of the existing material decomposition methods for spectral CT is presented.The models of material decomposition based on different methods are described, including projection-domain, image-domain and one step methods; different optimization methods are discussed.

In Chapter 3, entitled "**Material Decomposition in X-ray Spectral CT Using Multiple Constraints in Image Domain** ", we have proposed a material decomposition method using bounded mass density, local joint sparsity and structural low-rank (DSR) in image-domain for spectral CT. The proposed method was evaluated on both digital and physical data.

In Chapter 4, entitled "**ROI-Wise Material Decomposition in Spectral Photon-counting CT**", we have proposed a ROI-wise material decomposition method for sCT by jointly optimizing basis materials and reducing noise. The effectiveness of the proposed method was validated on both digital and physical data.

In Chapter 5, entitled "**Super-Energy-Resolution Material Decomposition in Spectral Photon-counting CT Using Pixel-wise Learning**", we propose to directly improve the energy resolution by introducing a super-energy-resolution imaging in sCT.

# Chapter 1

# Principles of Spectral X-ray CT

## Contents

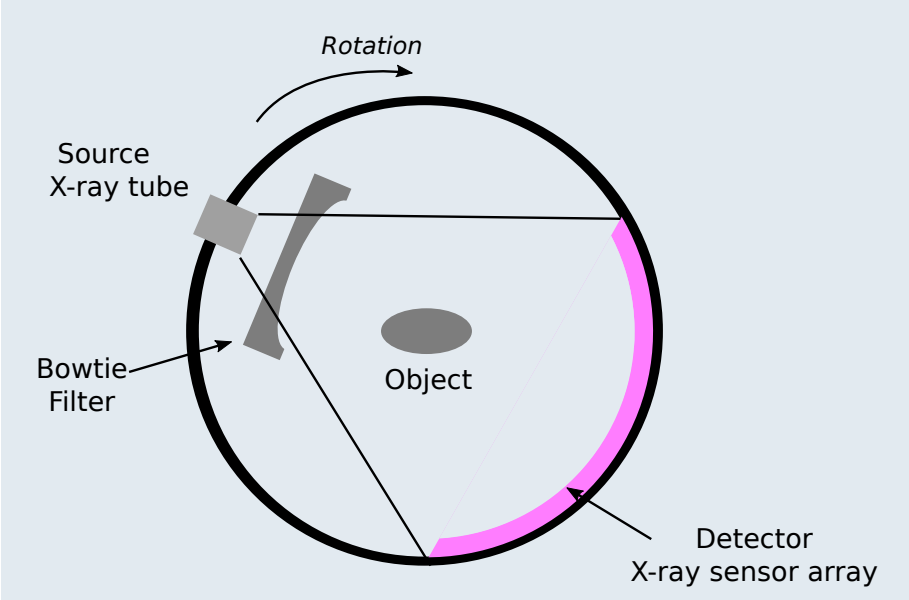


Figure 1.1: X-ray attenuation measurement in CT. The x-ray photons emitted by the source pass through the object which is usually a patient for clinical applications. The detector measures an intensity of x-ray quantum, spatially resolved over the x-ray fan-beam. Note that a bowtie filter in front of the X-ray tube before irradiating any object is usually applied to modulate the x-ray flux.

## 1.1 General introduction to spectral x-ray CT

Figure 1.1 illustrates the setup of a x-ray attenuation measurement in general x-ray computed tomography (CT). The source emits a flux of x-ray quantum at an object. The object consists of x-ray-attenuating materials that are described by their linear attenuation coefficient $\mu(\vec{x},E)$ at position $\vec{x}$. The detector registers the quantum passing through the object.

The main difference between spectral CT and conventional energy integrating CT or dual-energy CT is the detector. For conventional CT or dual-energy CT, detectors only count photons of different energy in one (Figure 1.2a) or two channels (Figure 1.2b). While for spectral CT, the new photon-counting detector (PCD) can register photons in multiple channels (Figure 1.2c). In the following, we briefly review the spectral characteristics of the source, attenuations in the object and detectors for different CT imaging.

### 1.1.1 Source

The x-ray sources are resulted from an electron beam striking a metal target. The electrons are accelerated in a vacuum tube with a high voltage $U_{\text{acc}}$, and then bombard a metal target (usually tungsten, alloy of rhenium and tungsten, molybdenum or copper) with a high velocity. The deceleration of electrons will lead to the emission of Bremsstrahlung, where the lost kinetic energy is converted into photons with continuous spectrum. On the other hand, the incident electrons can also interact with the orbital electrons. When

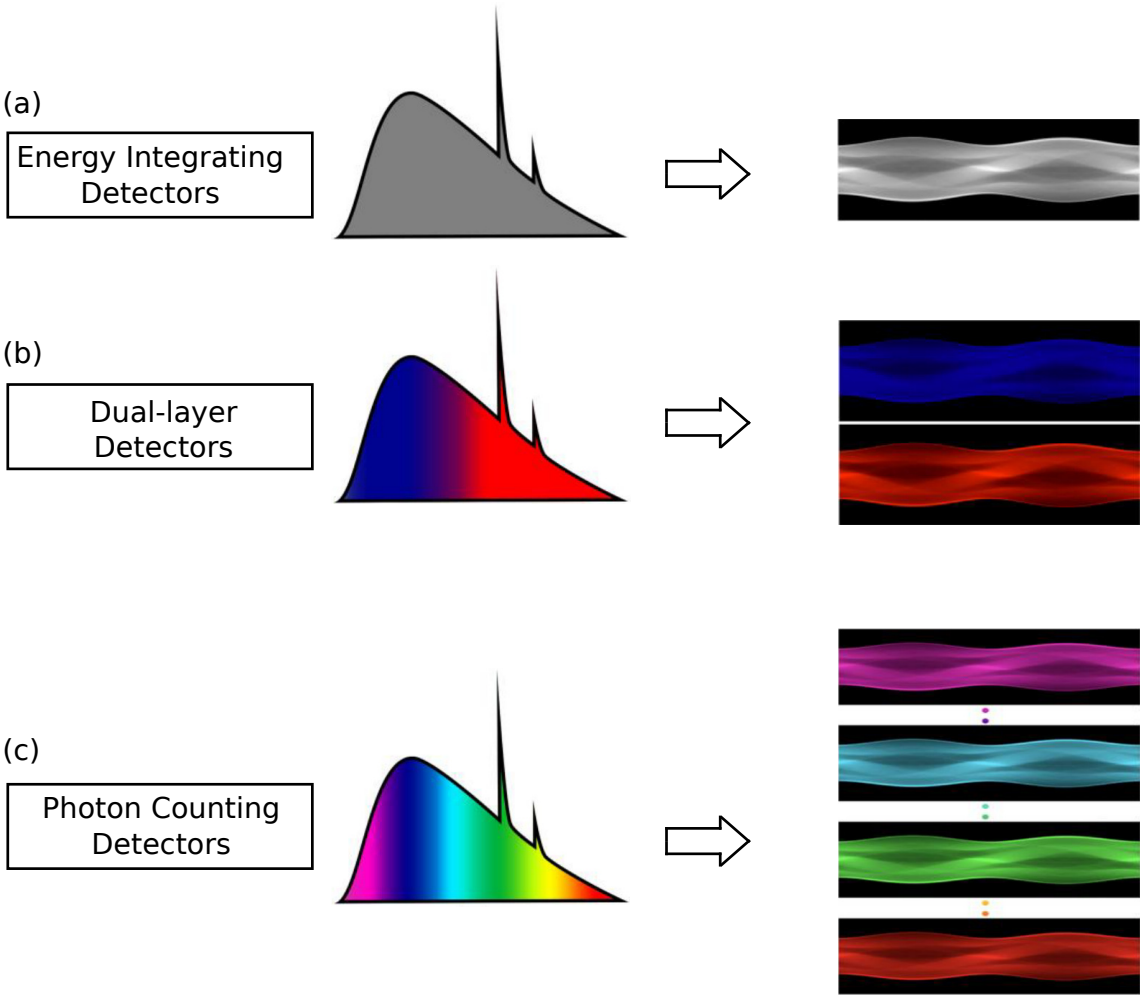


Figure 1.2: Representation of the information provided by different detectors in X-ray CT. (a) Energy integrating detectors; (b) Dual-layer detectors; (c) photon-counting detectors. (Adapted form [Si-Mohamed et al., 2017a])

an orbital electron is knocked out of the inner shell of the target metal atom, the electron from higher energy levels will fill the inner shell vacancy, resulting in emission of x-ray. Usually the transitions are from upper shells into K shell (called K lines), into L shell (called L lines). The wavelength of X-rays emitted through this process depends on the type of metal material and the energy gap between the respective electron orbital shells. Thus the X-rays have several specific discrete energies, called characteristic X-ray.

Meanwhile, bowtie filters are widely applied in current x-ray CT to modulate the output of the radiation source. Filtering the x-ray beam can reduce the radiation dose to the patient and help to minimize image artifact. The filters reduce the range of x-ray energies that reach the patient by removing the low-energy x-rays. Low-energy (or 'soft') x-rays are readily absorbed by the patient, therefore they do not contribute to the CT image but do contribute to the radiation dose to the patient. In addition, creating a more uniform beam intensity improves the CT image by reducing artifacts that result from

beam hardening [Mail et al., 2008, Heismann, Björn J., Bernhard T. Schmidt and Flohr., 2012].

The physical unit of this spectrum is quanta per energy, *i.e.* the number of quantum per kiloclectron volts (keV). The maximum of the emitted quantum energy $E$ is limited by the voltage used for the acceleration of the x-ray-generating electrons. Figure 1.3 shows a x-ray source spectrum (filtered by a bowtie filter) for the tube voltage 120 kV. The Bremsstrahlung emission and characteristic X-rays can be observed in this spectrum.

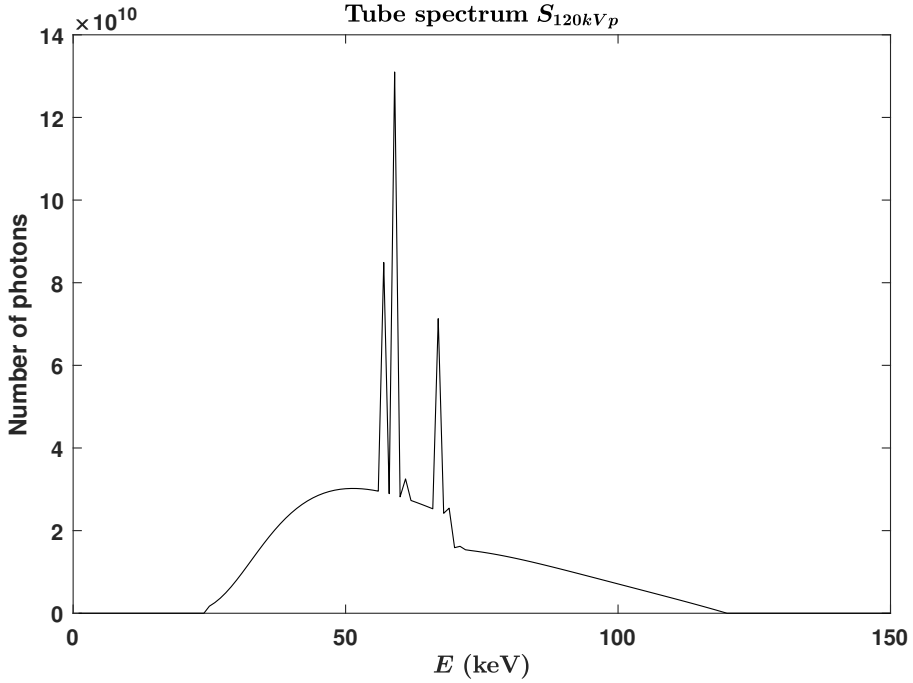


Figure 1.3: X-ray tube spectrum for the tube acceleration voltage U =120 kV. The spectrum is mainly composed of a broad quantum distribution caused by Bremsstrahlung in the x-ray tube anode material. The characteristic lines are due to inner electron shell transitions during a photoelectric effect event in the anode material atoms. Measured on Philips spectral CT prototype [Cormode et al., 2017, Si-Mohamed et al., 2018]

The intensity of emitted X-rays are determined by photon flux and the energy of photons. The photon flux is defined as the number of photons per second per unit area and it is proportional to the tube current. In clinical applications, it is important to evaluate the dose of x-ray. Multiple metrics has been proposed for the quantitative measurement of x-ray dose, *e.g.* water equivalent diameter ($\boldsymbol{D_W}$), CT dose index ($\boldsymbol{CTDI_{vol}}$) and size-specific dose estimation $\boldsymbol{SSDE}$.

### 1.1.2 Attenuation

X-ray attenuation is characterized by Lambert-Beer's Law and is primarily a function of beam energy and the density and composition of the material of the object being scanned.

For a monochromatic X-ray beam of energy $E$, Lambert-Beer's law gives the beam intensity value $I$ after crossing a thickness $\Delta x$ of matter as:

$$I = I_0 e^{-\int_{L(u)} \mu(\vec{x}) dx}, \tag{1.1}$$

where $I_0$ is the initial X-ray intensity, $\mu(\vec{x}, E)$ the linear attenuation coefficient at position or pixel $\vec{x}$ for energy $E$, in units of $cm^{-1}$, and $L(u)$ the $u$-th ray. In the case of polychromatic x-ray beam, equation (1.1) becomes:

$$I = \int_{E_{min}}^{E_{max}} I_0(E) e^{-\int_{L(u)} \mu(\vec{x}, E) dx} dE, \tag{1.2}$$

where $[E_{min}, E_{max}]$ is the energy range of the x-ray spectrum.

The linear attenuation coefficient $\mu$ of all materials depends on the photon energy of the beam and the atomic number of elements in the material. Since it is the mass of the material itself that is providing the attenuation, linear attenuation coefficients are often characterized by $\mu/\rho$, the mass attenuation coefficient $\mu_{\mathrm{m}}$ in units of $cm^2/g$, as:

$$\mu_{\mathrm{m}}(E) = \mu/\rho, \tag{1.3}$$

where $\rho$ is the mass density.

**Physical mechanisms of x-ray attenuation**

The mass attenuation coefficient $\mu_{\mathrm{m}}(E)$ is a characteristic function for all chemical elements indexed by the atomic number Z in the periodic table of elements. In the clinical range below 200 keV, $\mu_{\mathrm{m}}$ is determined by three mechanisms: coherent (Rayleigh) scatter, photoelectric absorption, and Compton scatter. Figure 1.4 shows the relative strengths of these three interactions (and their total) over the diagnostic range of energies for water and lead.

*Coherent* or *Rayleigh scattering* is the apparent deflection of x-ray beams caused by atoms being excited by the incident radiation and then re-emitting waves at the same wavelengths. This phenomenon is useful in x-ray diffraction studies, where the x-ray energies are of the order of a few kiloelectron volts and thus the wavelengths arc the same order of magnitude as atomic dimensions. It is relatively unimportant in the energies used in diagnostic radiology, as is seen by the plots of $\mu_r/\rho$ in Figure 1.4.

*Photoelectric effect* is the absorption of a photon by a tightly bound electron, as seen by the plots of $\mu_p/\rho$ in Figure 1.4. The electron is ejected from the atom with enough kinetic energy, then a vacancy left behind in the shell. Often an electron in a outer shell falls into the inner shell to fill the vacancy, releasing energy in the form of a photon. This is accompanied by the emission of characteristic x-ray photons called fluorescence radiation. Lower-energy excitation is absorbed in the M and L shells, while higher-energy radiation is absorbed in the inner K shell. For X-ray energies, electrons in the K shell are predominantly involved. Especially, the attenuation coefficient undergoes a sharp increase in the energy region corresponding to the K shell. This is known as the K absorption edge (i.e. K-edge). This absorption becomes particularly important with the high-atomic-number (high-Z) materials because their binding energies are closer to x-ray energy range. For the lower-atomic-number elements, such as are found in water and organic material, this

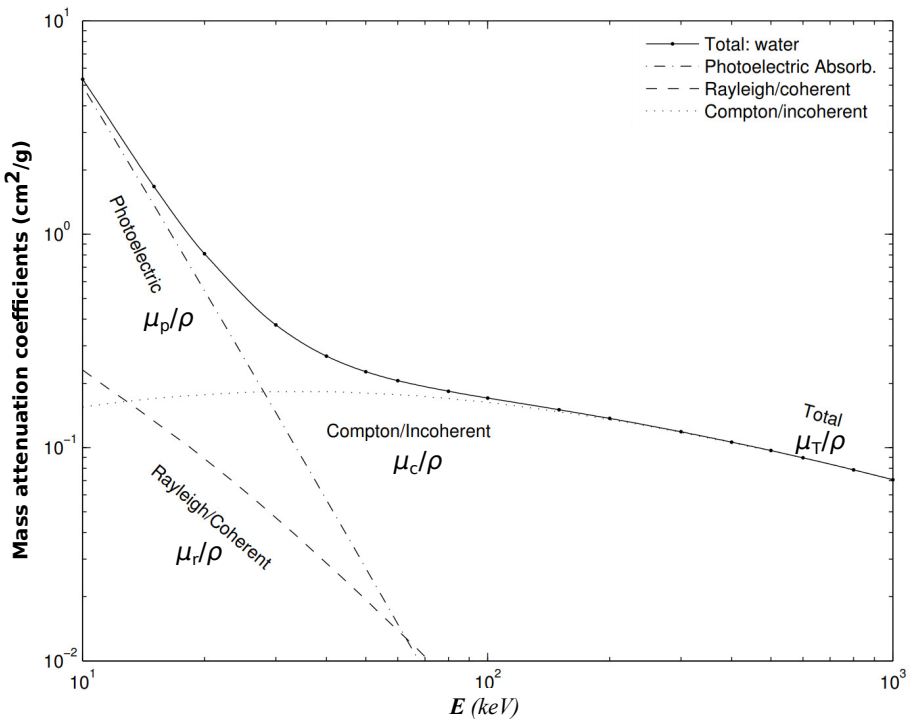


(a)

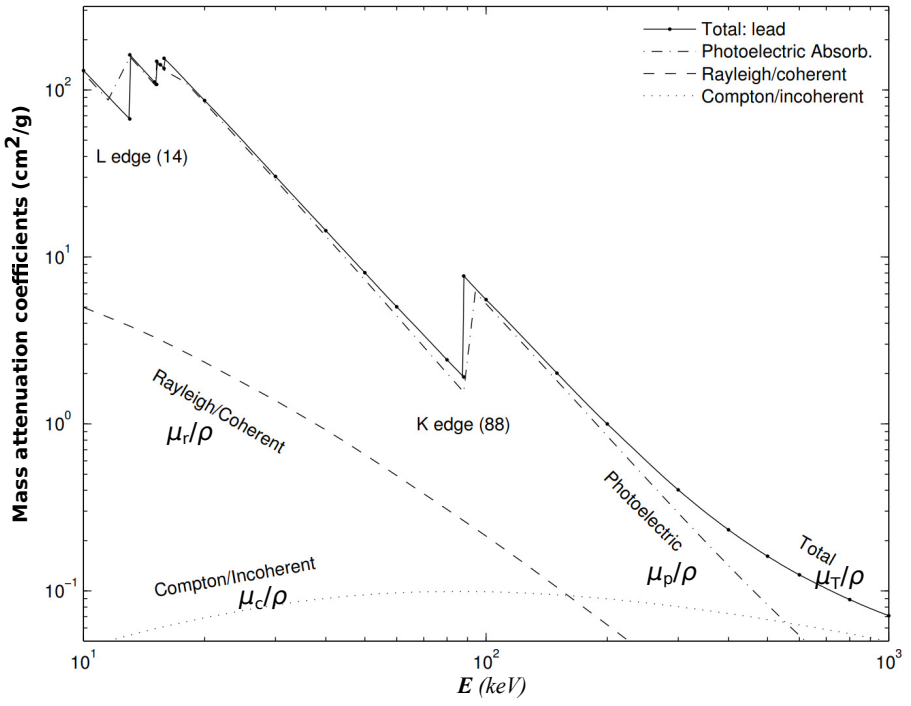


(b)

Figure 1.4: Total and components of mass attenuation coefficients of (a) water and (b) lead ($\rho = 11.5\ g/cm^2$).

K edge occurs below the diagnostic energy spectrum being used. However, for high-Z materials, such as lead shown in Figure 1.4b, this K edge occurs within the spectrum of interest.

*Compton effect* consists of a collision between an x-ray photon and either a free or a loosely bound electron in an outer shell. It occurs when the incident photon has energy that is much more than the binding energy. As seen in Figure 1.4a, Compton scattering ($\mu_c/\rho$) is the largest component for water in most of the energy range. In clinical applications, Compton scattering is the most significant and most troublesome source of tissue attenuation.

Higher atomic-number elements will experience primarily photoelectric absorption, while those of lower atomic numbers will be dominated by Compton scattering. Since each interaction is independent, the total attenuation coefficient is the sum of that due to photoelectric, Rayleigh, and Compton coefficients, as is seen by the plots of $\mu_T/\rho$ in Figure 1.4.

**Mass attenuation coefficients of mixtures**

For mixtures, the mass attenuation coefficient is given by:

$$\mu_m = \sum_i w_i \frac{\mu_i}{\rho_i}, \tag{1.4}$$

where $\rho$ is the density of the mixture, $\mu_i$ the linear attenuation coefficient of element $i$, $\rho_i$ the density of element $i$, and $w_i$ the fraction by weight of the element in the material. Precise measurement data of the mass attenuation coefficient is available in numerous literature sources. The U.S. National Institute of Standards and Technology (NIST) hosts the constantly updated XCOM source at www.nist.gov [Saloman and Hubbell, 1986]. Figure shows four categories of materials existed in human body: soft tissue, bone material, contrast agents and metallic implants, and associated materials.

*Soft tissue* has elemental compositions close to water, *i.e.*, it mainly contains hydrogen and oxygen atoms. Soft tissue has typical densities between 0.9 and 1.1 $g/cm^3$. Healthy and pathogenic tissue types usually differ by 10 to 20 $mg/cm^3$ in density. Note that $\mu_m$ of water is very similar with soft tissue, which are usually treated in one category.

*Bone material* as the second group contains the bone mineral hydroxyapatite in varying concentrations. It generally has significantly higher densities than soft tissue, around 1.5 to 2 $g/cm^3$. Both the elevated density and the calcium and phosphorus mass contributions lead to a comparably strong x-ray attenuation of bone material, in particular for low energies. CT imaging benefits greatly from the generally high contrast between bone material and soft tissue.

*Contrast agents* containing iodine, gadolinium *etc*, which has K-edge within the clinical x-ray tube spectrum. In conventional CT, these agents are administered to the patient to increase contrast in soft tissue exams or CT angiograms. Statistically, contrast agents are used in more than 50% of CT exams. In most cases, iodine (I) based contrast agents are used. Gadolinium (Gd) based substances, which are the standard contrast agent in MRI, are rarely administered in conventional CT exams. The injection of the contrast agent into a blood vessel generates a so-called contrast bolus that travels through the

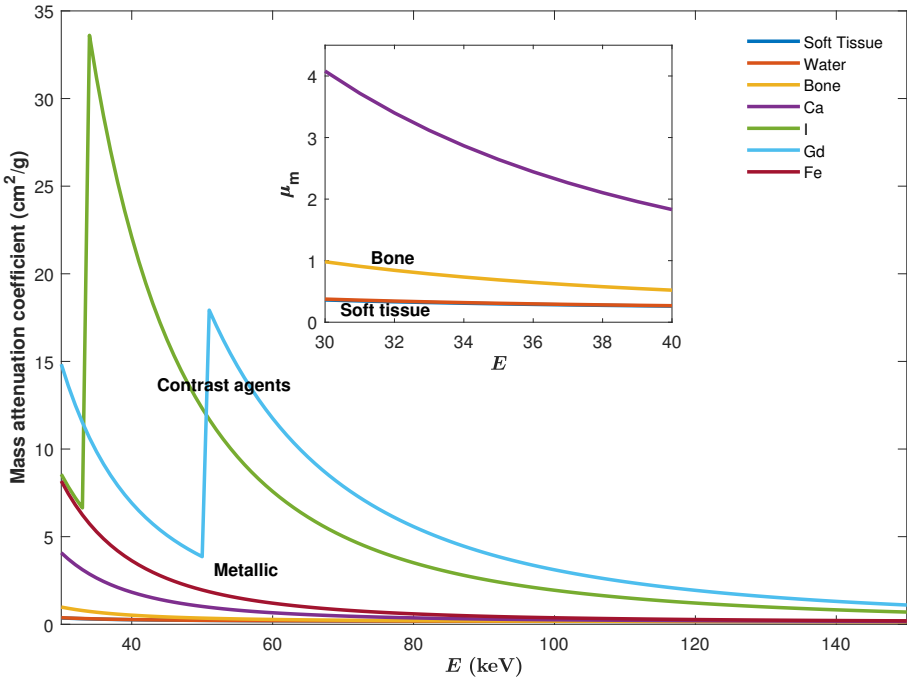


Figure 1.5: Mass attenuation coefficients of the chemical elements and compounds marked in the legend.

blood vessel system. The contrast between blood and surrounding tissue in simultaneously acquired CT images is strongly increased. CT angiography, the representation of the human blood vessel system, is performed in this fashion. Unlike conventional CT, sCT uses energy-resolving detectors that can simultaneously sample the energy spectrum at multiple regions. This allows a higher spectral resolution, enabling the identification of material-specific spectral characteristics, such as the K-edge signature of the contrast agent. This is particularly interesting as the K-edge energies of contrast agents that contain heavy elements such as gadolinium, ytterbium, bismuth or gold nanoparticles (AuNPs) are within the clinical x-ray tube spectrum [Schlomka et al., 2008, Pan et al., 2010, Schirra et al., 2014, Pan et al., 2014, Si-Mohamed et al., 2017b, Si-Mohamed et al., 2018].

*Metallic* implants such as iron (Fe), titanium (Ti) hip joint replacements or gold (Au) tooth fillings might be present in some scanning regions and patients. They might be a source of strong streak-like artifacts in CT images since the localized strong decrease in projection signal emphasizes the limits of linear projection mathematics. Metallic implants are usually not part of diagnostic tasks and are neglected in the following discussion.

### 1.1.3 Detectors

**Detectors of conventional CT and dual-energy CT**

Conventional CT devices are equipped with energy integrating detectors (EIDs) in which the detected signal is proportional to the total energy deposited by all photons without specific information about an individual photon or its energy. EIDs use a two-step process to convert the incoming X-ray intensity into an electronic signal, as shown in Figure 1.6. First, the X-rays are converted into visible light in a scintillator layer. Below, the figure shows a photodiode array that converts the emitted light into an electric current that is digitized in dedicated application-specific integrated circuit (ASIC). The scintillator layer is made of a ceramic material that is mechanically structured into pixels. Septa of finite width separate the individual pixels in order to suppress optical cross-talk. The effective detector pixel sizes range from 0.5 to 0.625 mm at the isocenter for the commercial EIDs.

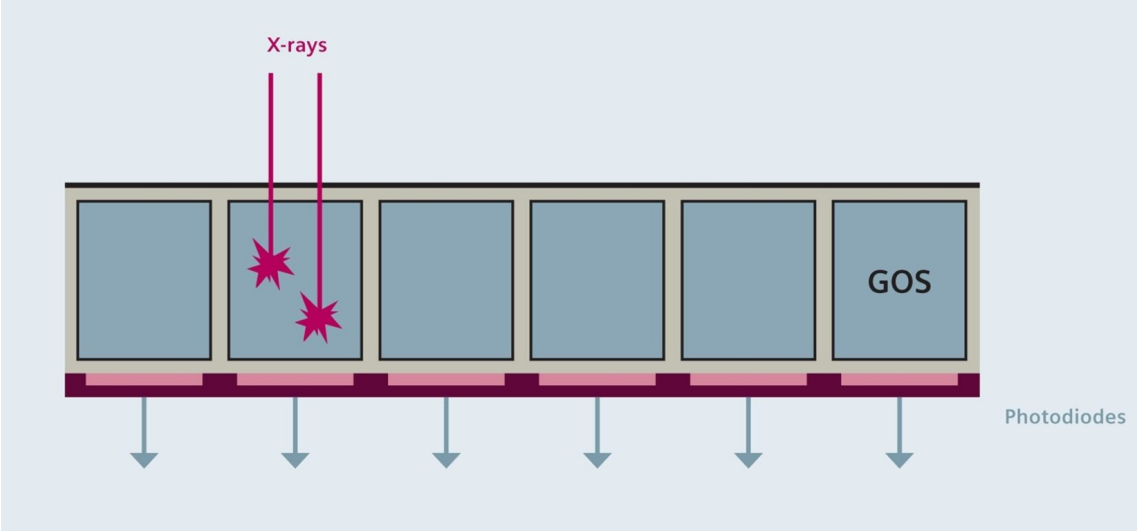


Figure 1.6: Energy integrating detectors convert x-ray into an electrical signal in a two-step process: first, a scintillator layer (GOS) converts x-ray into visible light. Photodiodes then convert light into an electrical current.

In dual-energy CT, an additional attenuation measurement is obtained at a second energy. A number of technical approaches have been developed to realize dual-energy CT: *e.g.* two temporally sequential scans, rapid switching of x-ray tube voltage, dual x-ray sources and dual-layer detector, *etc*, as shown in Figure 1.7.

*Sequential acquisition*: The approach that requires the least hardware effort is the sequential acquisition of two datasets at different tube voltages. Sequential acquisition can be achieved either as two subsequent helical scans or as a sequence with subsequent rotations at alternating tube voltages and stepwise table feed. This approach may make sense in systems with broad detectors, but a disadvantage is the rather long delay between both acquisitions. The delay is too long to preclude artifacts from cardiac or respiratory motion or changes in contrast material opacification.

*Rapid voltage switching* (Figure 1.7a): Another approach with very little technical effort

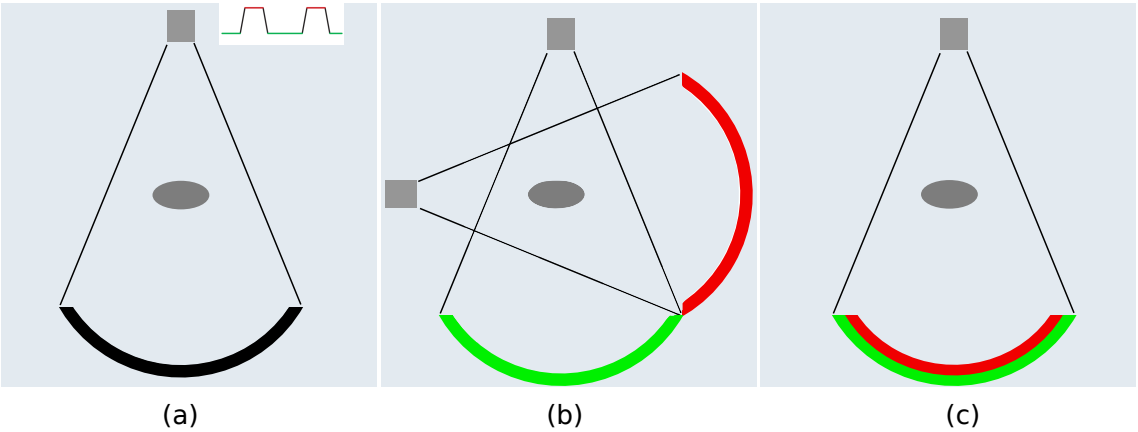


Figure 1.7: (a) Rapid kilovoltage-switching system containing only one tube and one detector. Voltage is switched rapidly between two levels; (b) dual-source CT system with two tubes and detectors mounted orthogonally in one gantry. Tubes are operated at different tube voltages; (c) dual-layer detector system with one x-ray tube running at constant voltage. Dual-energy information is derived from two layers of detector with different sensitivity profiles.

is rapid voltage switching. With this method, the tube voltage alternates between a high value and a low value, and transmission data are collected twice for every projection or, in practice, for immediately adjacent projections. However, the tube current could not be increased quickly enough for the low tube potential measurements to achieve comparable noise levels in both the low and high tube potential data sets. This difference in noise limited extension of the technique beyond bone densitometry applications. Still, the spectral resolution of rapid voltage-switching systems remains limited and usually requires additional dose.

*Dual-source CT* (Figure 1.7b): Dual-source CT is a CT system where two x-ray sources and two data acquisition systems are mounted on the same gantry, positioned orthogonally to one another. This setup requires nearly twofold investments in hardware but offers important advantages: the voltage, current, and filter can be chosen independently for both tubes to achieve an optimal spectral contrast with sufficient transmission and the least overlap. The data are acquired simultaneously by both orthogonal systems. However, because both tubes are simultaneously energized, scattered radiation whose original primary photon came from one tube may be detected by the detector for the other tube, and vice versa. This degrades spectral separation and requires the implementation of an appropriate scatter-correction algorithm.

*Dual-layer detector* (Figure 1.7c): Another approach for acquiring du- al-energy CT projection data uses a single high tube potential beam and layered or "sandwich" scintillation detectors, as shown in Figure 1.8. The low-energy data are collected from the front or innermost detector laye+r and the high-energy data are collected from the back or outermost detector layer. An advantage to this approach is that the low- and high-energy data sets are acquired simultaneously, and the data from the inner and outer detector layers are recorded at all times. whereas, with this setup, the scintillator materials determine

the spectral resolution, and the sensitivity profiles of the available materials have a rather broad overlap. Therefore, the contrast of the spectral information is limited or requires a relatively high additional dose.

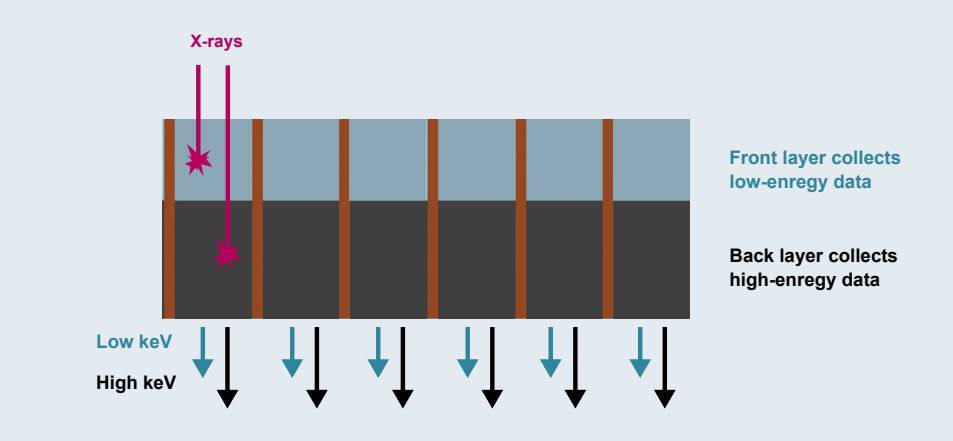


Figure 1.8: In a dual-layer detector, low-energy quanta are predominantly collected in the front layer. X-rays capable of passing through the front layer are predominantly of higher energy and are collected in the back detector layer.

Table 1.1 lists the compares of different technical approaches of dual-energy CT.

Table 1.1: Technical approaches of dual-energy CT.

| Technology | Strengths | Weaknesses |
|---|---|---|
| Sequential Acquisition | No special detectors required | Long acquisition time: sensitive to movements and more artifacts. |
| Rapid Voltage Switching | Near-simultaneous acquisition of low- and high-energy data | Requires specialized hardware; Noise level may differ between low- and high-energy images; Relatively high overlap of spectrum. |
| Dual-Source CT | Independent tube current and filtration optimization; Relatively low degree of spectral overlap. | Requires specialized hardware; Scatter-correction. |
| Dual-layer Detector | Simultaneous acquisition of low- and high-energy data | Requires specialized hardware; Relatively high spectrum overlap; Noise level may differ between low- and high-energy images. |

**Photon-counting detector of spectral CT**

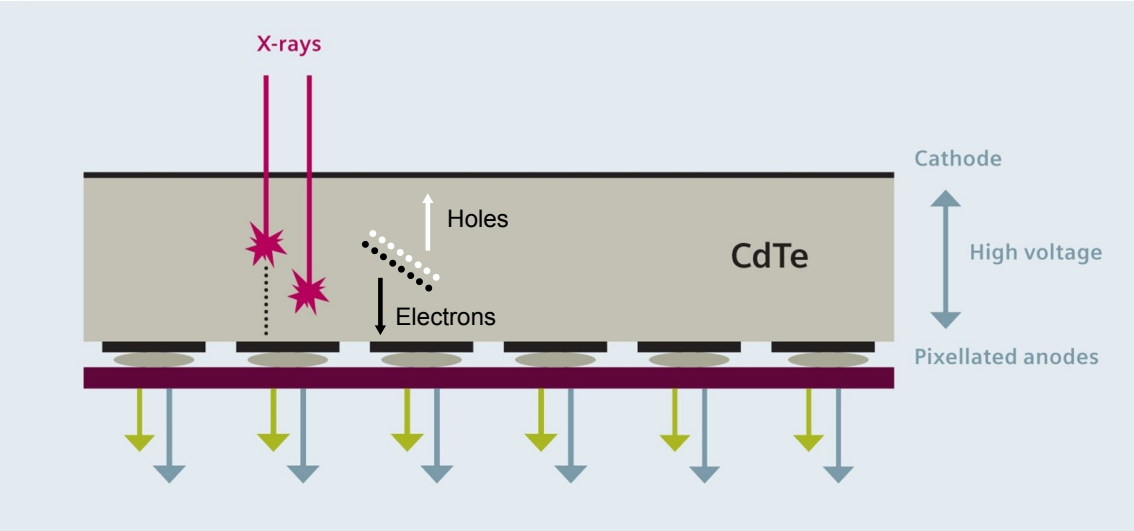


Figure 1.9: Photon-counting detector can directly convert x-ray into an electrical current. Each photons can be detected individually and its energy can be measured.

Spectral CT imaging is realized by photon-counting detectors (PCD). This new generation of detectors measures and analyzes incident photons individually and produces a digital measure of photon energy through pulse height analysis. Each photon impacting the detector is counted and its energy determined. As shown in Figure 1.9, semiconductor materials such as cadmium telluride (CdTe) are able to convert X-rays directly into electric signal pulses. Each incoming X-ray quantum generates a number of electron-hole pairs; then the electrons and the holes move to the opposite directions, the anode and the cathode respectively, under a strong electrical field inside the detector material; the moving charge carriers induce the signals on the electrodes. Highly integrated circuits transform these charge pulses into voltage pulses of a few nanoseconds duration that can be counted digitally.

The direct conversion of the photon signal into a digital measurement eliminates electronic noise, which offers the opportunity to acquire data at lower noise levels and in turn to use lower radiation doses. Meanwhile, instead of being less weighted, low-energy photons can be counted in order to bring valuable information, e.g. more contrast to the image. Furthermore, PCDs can eliminate the septa between adjacent detector pixels required by EIDs to avoid cross-talk and maintain spatial resolution. This feature leads to a PCD detector size of 0.25 mm at the isocenter (compared with 0.5–0.6 mm for EIDs) [Zhou et al., 2018].

However, PCDs are not flawless, the measurement of PCDs may deviate from the truth for several reasons [Taguchi and Iwanczyk, 2013]:

- Pulse pileup. When several photon interactions occur at the same time, multiple pulses may be piled up and be counted as one event, resulting in wrong recorded energy and counts loss.

- Charge sharing. When the generated electron charge cloud reaches the anode near the pixel boundary, they maybe divided and counted by the neighboring pixels to a smaller energy level.
- K-escape X-rays. X-ray fluorescence or Auger electrons may be generated during the photoelectric effect. The fluorescent X-ray photons can either be absorbed by the PCD pixel with the primary interaction again, be detected by an adjacent pixel, or leave the PCD completely.
- Compton scattering. The photon energy is not fully transmitted to electrons, resulting in energy loss.
- Charge trapping. The electron or hole is trapped by a trapping center and is thermally re-emitted with a delay. This will result in lower-energy counting.
- Polarization and long-term reliability.

As a consequence, two adjacent energy bins are not sharply separated by the energy threshold at their common boundary. Their sensitivities are described by so-called *detector response function* $d(E)$ and the effects contributing to the degradation of the energy resolution lead to an overlap of the detector response function. $d(E)$ yields the relative signal amount generated by a specific x-ray quantum of energy $E$. For an ideal integrating detector, often $d(E) = E$ is assumed. However, considering the aforementioned physical effects, $d(E)$ has a more sophisticated structure. Figure 1.10 shows the experimented $d(E)$ function, which measured by illuminating PCD under constant flux conditions with monochromatic photons of energy $E$. Considering the detector response function, a more general form of Lambert-Beer's law, equation (1.2), is given by:

$$\bar{I}_i(u) = \int_{\mathbb{R}} I_0(E) d(E) e^{-\int_{L(u)} \mu(\vec{x},E) \mathrm{d}l} \mathrm{d}E, \tag{1.5}$$

where $\bar{I}_i(u)$ is the mean measured signal (number of photons penetrating materials) recorded by a PCD for the $u$-th ray within the $i$-th energy bin, $\mathbb{R}$ the energy range of the $i$-th bin, and $d(E)$ the detector response function.

Meanwhile, sCT suffers from severe quantum noise problem because of the limited photon flux, as an immediate consequence of preventing the pileup effect. Specifically, the limited photons can lead to worse signal-to-noise ratio (SNR) in sCT images than in traditional CT images, considering image noise is inversely related to the square root of the total number of photons used for reconstruction [Leng et al., 2011]. Noises at different energy bins are independent when the charge sharing effect of PCD can be ignored. Due to the severe quantum noise, the measured signal is assumed to be corrupted by independent Poisson:

$$I_i(u) = \mathcal{P}(\lambda = \bar{I}_i(u)), \tag{1.6}$$

where $\mathcal{P}(\lambda)$ denotes the Poisson distribution of mean $\lambda$, and $I_i(u)$ the measured number of photons for the $u$-th ray in the $i$-th energy bin.

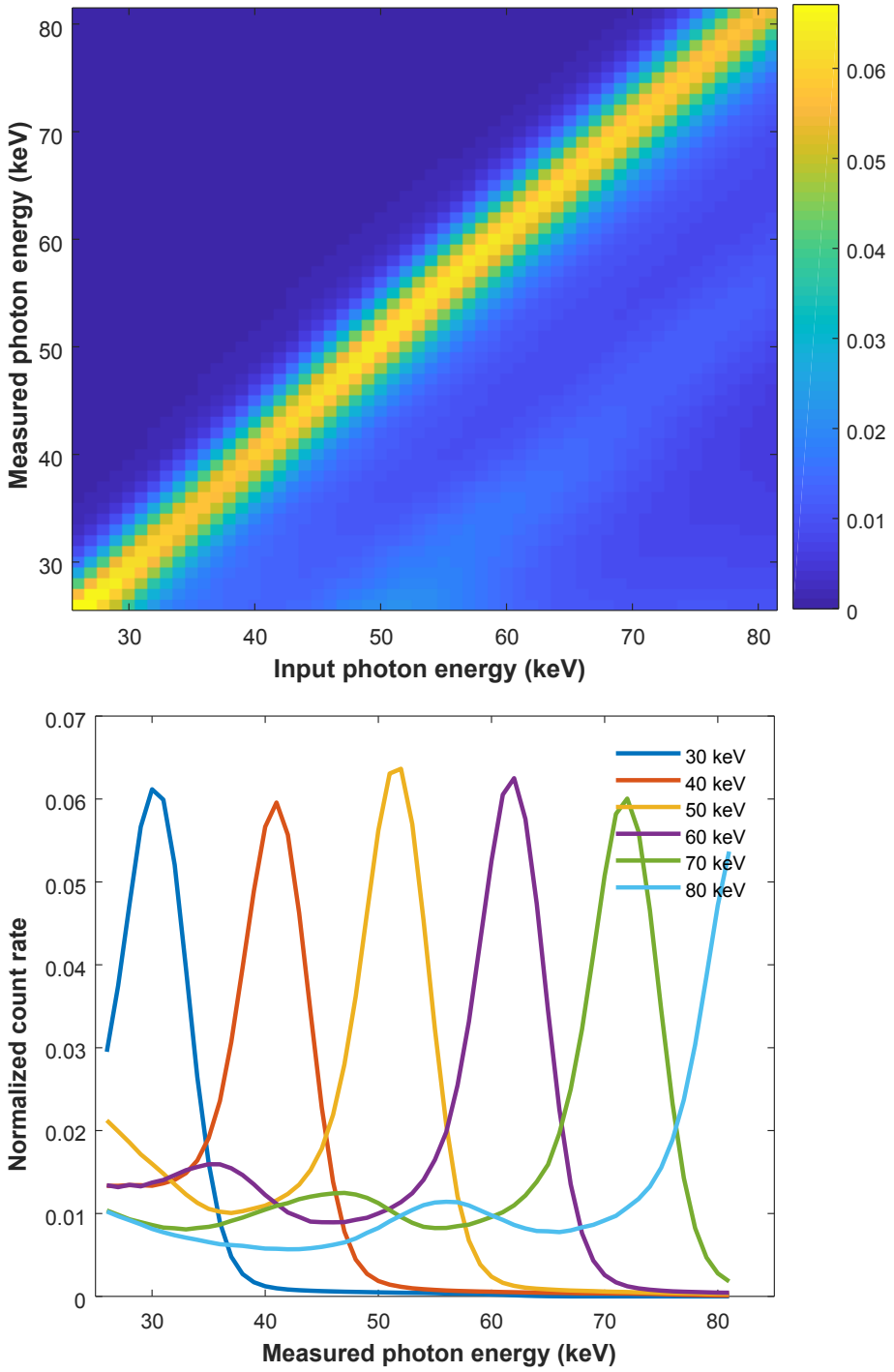


Figure 1.10: (a) Measured detector response function one threshold in one detector pixel resulting from monochromatic illumination with photon energies ranging from 25 keV to 80 keV. The count rate in the detector was about 105 photons pixel$^{-1}$ s$^{-1}$. The data are normalized to an integrated count rate of 1 cts s$^{-1}$ above 20 keV and (b) measurements of input monochromatic photons of 30, 40, 50, 60, 70 and 80 keV.

## 1.2 Spectral CT image reconstruction

The aim of reconstruction is to obtain the linear attenuation coefficients at each energy bin:

$$\mu(\vec{x},i) = \underset{\mu}{\operatorname{argmin}} \mathcal{D}(I_i(u), \mu(\vec{x},i)), \tag{1.7}$$

where $\mu(\vec{x},i)$ denotes the reconstructed linear attenuation coefficients at the $i$-th energy bin, which also represents the reconstructed spatial image at the $i$-th energy bin, and $\mathcal{D}$ the discrepancy function.

For sCT, there are two strategies to reconstruct the spatial images: separately reconstruct image at each bin (**separate reconstruction**), or jointly reconstruct by exploiting the information of all bins (**joint reconstruction**).

### 1.2.1 Separate reconstruction

Separate reconstruction is to independently form images at each energy bin using common reconstruction methods. In traditional CT, image reconstruction is an important step to retrieve the cross sectional attenuation coefficients from the measured X-ray data, which is the transmitted beam intensity along a line between X-ray source and detector. Specifically, reconstruction aims to reconstruct the spatial distributed $\mu(\vec{x},E)$ from its line integrals $\int_{L(u)} \mu(\vec{x},E)dx$.

For monochromatic radiation of energy $E = E_0$, the line integral given by the ratio of the two intensities $I$ and $I_0$ as:

$$-\ln(\frac{I_0}{I}) = \int_{L(u)} \mu(\vec{x},E_0)dx, \tag{1.8}$$

which is equivalent to a Radon transform. However, x-ray spectrum in practice is usually polychromatic, which means the line integral is not directly measured and the resultant behavior is nonlinear. Generally, the reconstruction model of polychromatic radiation assumes that we can calculate the an effective value of $\mu(\vec{x},\bar{E})$, where $\bar{E}$ is the average energy on the range of the x-ray beam. As a consequence, the line integral is:

$$-\ln(\frac{I_0}{I}) = \int_{L(u)} \mu(\vec{x},\bar{E})dx. \tag{1.9}$$

This assumption yields some artifacts in the CT reconstruction due to beam hardening. In this case, the x-ray photons passing through the object are considered to have an effective detected energy. When quantum pass through thick or high-atomic-number-object regions such as bone, the average energy of the detected quantum increases due to the lower energy photons are more likely to be absorbed. In other words, the beam spectrum is 'hardened.' As a result, the model separate reconstruction is formulated as:

$$\mu(\vec{x},i) = \underset{\mu}{\operatorname{argmin}} \mathcal{D}(ln(\frac{I_i(u)}{\int_{\mathbb{R}} n_0(E)d_i(E)\mathrm{d}E}), \mu(\vec{x},i)). \tag{1.10}$$

To solve the minimization problem of (1.10), we briefly introduce two common reconstruction methods in traditional CT: filtered back-projection (FBP) method and iterative reconstruction method.

**Filtered back-projection reconstruction method**

The filtered back-projection algorithm is one of the most commonly used algorithms for tomographic image reconstruction. As the name implies, there are three steps in the filtered back-projection algorithm: the transform part which transforms projection data into frequency domain with Fourier transform; the filtering part, which can be visualized as a simple weighting of each projection in the frequency domain; the back-projection part which consists of projecting back each view along a line corresponding to the direction in which the projection data were collected, as:

① Calculate Fourier transform of line integral $-\ln(\frac{I_0}{I})$, get $F(u,v)$;

② Multiply $F(u,v)$ with transfer function of ramp filter $|\omega|$, get $Q_\beta$;

③ Back-project $Q_\beta$, get image $\mu(x,y)$;

In details, we generalize $\mu(x,y)$ with $f(x,y)$, the path that the X-ray crosses in the object can be given by:

$$x\cos\beta + y\sin\beta = t, \tag{1.11}$$

in which $\beta$ and $t$ are polar coordinates of the path that the X-ray beam crosses through the object. Given $F(u,v)$ the Fourier transform of the projection data (line integral) with $u$ and $v$ representing two spatial frequencies, the object function $f(x,y)$ may then be obtained from$F(u,v)$ by the inverse Fourier transform:

$$f(x,y) = \int_{-\infty}^{+\infty}\int_{-\infty}^{+\infty} F(u,v)\mathrm{e}^{2\pi i(ux+vy)}\,du\,dv. \tag{1.12}$$

Knowing that the Fourier slice theorem relates the parallel projections to object data which are collected in the polar coordinates, we change in equation (1.12) from Cartesian coordinates $(u,v)$ to polar coordinates $(\beta,\omega)$ as follows:

$$\begin{cases} u = \omega\cos\beta \\ v = \omega\sin\beta \\ dudv = \omega d\omega d\beta, \end{cases} \tag{1.13}$$

to get

$$f(x,y) = \int_0^{2\pi}\int_0^{+\infty} F(\omega\cos\beta,\omega\sin\beta)\mathrm{e}^{2\pi\omega i(x\cos\theta+y\sin\theta)}\omega\,d\omega\,d\beta. \tag{1.14}$$

We substitute the two-dimensional Fourier transform $F(\omega\cos\beta,\omega\sin\beta)$ of object with the Fourier transform of the projection data at angle $\beta$, and the above equation can be expressed as:

$$\begin{aligned} f(x,y) &= \int_0^{\pi}\left[\int_0^{+\infty} F(\omega\cos\beta,\omega\sin\beta)w\mathrm{e}^{2\pi i(x\cos\beta+y\sin\beta)}\,dw\right]d\beta \\ &= \int_0^{\pi}\left[\int_{-\infty}^{+\infty} F(\omega\cos\beta,\omega\sin\beta)|w|\mathrm{e}^{2\pi i(x\cos\beta+y\sin\beta)}\,dw\right]d\beta \\ &= \int_0^{\pi} Q_\beta(x\cos\beta + y\sin\beta)\,d\beta, \end{aligned} \tag{1.15}$$

where

$$Q_\beta(x\cos\beta + y\sin\beta) = Q_\beta(t) = \int_{-\infty}^{+\infty} F(\omega\cos\beta, \omega\sin\beta)|w|e^{j2\pi t}\,dw. \tag{1.16}$$

As we can see, this algorithm consists of three main steps. The first step is to do a Fourier transform to projection data (line integral). Then, to filter the projections by a kernel whose frequency domain response is $|\omega|$ and known as the ramp filter. At last, these filtered projections $Q_\beta$ are back-projected to recover the object function $f$ (equation (1.15)). In practical applications, the ramp filter significantly amplifies the statistical noise existing in the projection data. To minimize this problem, the ramp kernel is usually associated with an apodization window. The most common window functions used are: i) sinc (Shepp-Logan filter), ii) cosine, iii) Hamming and iv) Hanning window functions.

**Iterative reconstruction method**

Iterative reconstruction method is another category of image reconstruction method for X-ray CT that begins with an image assumption, and compares it to real time measured values while making constant adjustments until the two are in agreement, by the following different steps:

① Set the reconstruction image an initial value $f^{(0)}$;

② Calculate the forward projection of the $f^{(k-1)}$ (for the first iteration $k = 1$, the second iteration $k = 2$, and so on);

③ Compare the difference between real measured data and calculated projection by step ②;

④ Correct reconstruction image by back-projection and obtain $f^{(k)}$;

⑤ Increase $k$ by 1 ($k = k + 1$) and repeat step ②, ③ and ④ until the stopping criterion is satisfied ;

The initial image $f^{(0)}$ is arbitrary, but usually we make it 0, or an image reconstructed by another method such as FBP. The stopping criterion can either be the maximum number of iterations, or the small enough update of current image estimate , or the predefined quality criterion [Beister et al., 2012]. A set of iterative reconstruction methods has been proposed, such as the algebraic reconstruction technique (ART) [Gordon et al., 1970], simultaneous iterative reconstruction technique(SIRT) [Gilbert, 1972], simultaneous algebraic reconstruction technique (SART) [Andersen and Kak, 1984], maximum likelihood expectation-maximization (ML-EM) algorithm [Shepp and Vardi, 1982], and so on. Here we introduce in detail the most basic and popular ART method.

In ART reconstruction, the projection process of CT imaging system can be represented by:

$$b_i = \sum_j a_{i,j} f_j, \tag{1.17}$$

where $b_i$ is the integration data measured with the $i_{\text{th}}$ ray (total number of rays $M$ =No.rotation angles $\times$ No.detectors); $a_{i,j}$ is the weighting factor that represents the contribution of the $j_{\text{th}}$ voxel to ray $i$; $f_j$ is the attenuation coefficient of voxel $j$ in our case. Therefore, we have:

$$A\boldsymbol{f} = \boldsymbol{b}, \tag{1.18}$$

where $A = a_{i,j}$ is the system matrix, $\boldsymbol{f} = [f_1, f_2 ..., f_N]$ is the image vector where $N$ is the total number of voxels in the reconstruction image, and $\boldsymbol{b} = [b_1, b_2 ..., b_M]$ is the measurement vector. To solve $\boldsymbol{f}$, the Kaczmarz method [KACZMARZ, 1993] is applied and the following iterative formula is obtained:

$$\boldsymbol{f}^{(k)} = \boldsymbol{f}^{(k-1)} + \lambda_{k-1} \frac{b_i - \boldsymbol{f}^{(k-1)} \boldsymbol{a}_i^T}{\boldsymbol{a}_i \boldsymbol{a}_i^T} \boldsymbol{a}_i, \tag{1.19}$$

where $k$ is the number of iterations and $\lambda_{k-1}$ is the relaxation parameter, $i = k \bmod M + 1$, $\boldsymbol{a}_i$ is a vector made of the $i_{\text{th}}$ row of $A$, .

Compared to analytical FBP method, iterative reconstruction has advantage to reduce noise and improve image quality by integrating various physical models and incorporating prior information. It outperforms FBP method especially with sparse and incomplete data. Specifically, additional regularization term can be processed using iterative reconstruction method, as

$$\mu(\vec{x}, i) = \underset{\mu}{\operatorname{argmin}} \mathcal{D}(ln(\frac{I_i(u)}{\int_{\mathbb{R}} n_0(E) d_i(E) \mathrm{d}E}), \mu(\vec{x}, i)) + \mathcal{R}, \tag{1.20}$$

where $\mathcal{R}$ denotes the regularization term. Typically, total variation (TV) methods [Rudin et al., 1992] have demonstrated their power in CT reconstruction with only a few x-ray projections [LaRoque et al., 2008, Song et al., 2007, Sidky and Pan, 2008, Chen et al., 2008] and low-dose CT [Tian et al., 2011]. In such approaches, the energy function of a TV form is minimized subject to a data fidelity condition posed by the x-ray projections. Since this energy term corresponds to image gradient, minimizing it will effectively remove those high spatial gradient parts such as noise and streaking artifacts in the reconstructed CT images. However, the most serious disadvantage of iterative reconstruction is its huge computational costs, since each iteration involves forward projections.

### 1.2.2 Joint reconstruction

The main objective of joint reconstruction is to mitigate artifacts by exploiting the information of multi bins. Specifically, the combination of multi-bin information can be realized during or after reconstruction (post-process). For methods during reconstruction, additional prior was exploited, such as sparsity and/or low-rank ( [Gao et al., 2011]), full-spectrum image reconstructed using conventional filtered back-projection [Yu et al., 2016, Liu et al., 2016], or features learned by tensor-based dictionary learning method [Zhang et al., 2017].

For post-process, redundant information embedded in reconstructed sCT images was utilized. For example, S. Leng proposed a method to denoise at each single bin with the help of a low-noise composite image which is produced by averaging images of all energy bins [Leng et al., 2011]. Z. Li proposed a multi-energy non-local means method to exploit spatio-spectral features in order to achieve noise reduction [Li et al., 2017]

## 1.3 Applications of spectral CT imaging

SCT can count the number of photons in multi separated energy bins with one single exposure, which is conceptually advantageous when compared to dual-energy CT. Dual-energy CT, at present, has a greater range of clinical applications, *e.g*. virtual monoenergetic imaging, automated bone/plaque removal in CT angiography, virtual non-contrast-enhanced/non-calcium imaging, kidney stone characterization, and discrimination of gout from pseudo gout [Kalender et al., 1988, Wu et al., 2009, Matsumoto et al., 2011, Yu et al., 2012, Mendonca et al., 2014, McCollough et al., 2015, Zhao et al., 2016, Iyama et al., 2018]. Although sCT is not currently used in clinical practice, it provides promising perspectives for many vitally important applications and opens up many new application possibilities. The main advantage of sCT technology is better sampling of the spectral information from the transmitted spectrum. Among the applications of using spectral information, quantitative material decomposition is the hottest topic, including K-edge imaging of contrast materials and selective imaging of other previously indistinguishable materials. In addition, virtual monochromatic imaging is another method of using spectral information to improve image quality. Other improvements of sCT compared to conventional CT, such as higher spatial resolution, lower radiation exposure and lower noise are also expected to provide benefits for diagnostic imaging.

### 1.3.1 Quantitative material decomposition

The attenuation of x-rays by matter is dependent on the energy of the photons. SCT can count the number of photons in different energies (*i.e*. separated energy bins) with one single exposure. Thanks to this advantage, it becomes possible to efficiently decompose different effects or materials (so-called basis materials) present in a pixel of spectral CT images.

Material decomposition can be realized by the means of separating different effects. For DECT, Alvarez and Macovski proposed to extract energy-dependent information by represent the total attenuation with functions correspond to two effects, photoelectric and Compton effect, and the energy-independent parts of the two effects were then reconstructed [Alvarez and Macovski, 1976]. The reconstructed photoelectric image provides composition information of object while the reconstructed Compton image provides mass density information of object. Although the Alvarez–Macovski dual-energy approach successfully offers a quantitative method for the characterization of tissue composition and eliminates beam-hardening, the benefits from the additional spectral information are limited. With sCT, whereas, more than two effects can be separated. Roessl and Proksa developed this idea by adding the K-edge terms on the photoelectric and Compton effect decomposition formula and gadolinium was discriminated from normal tissues in the thorax phantom in their simulation study [Roessl and Proksa, 2007]. Their results were further validated by CT system experiments where the contrast agents (gadolinium and iodine) were well quantified [Schlomka et al., 2008]. This technique was named K-edge imaging and it enables multi-agent imaging [Cormode et al., 2010, Pan and Yang, 2010, Panta et al., 2015, Si-Mohamed et al., 2017a, Lee et al., 2016a, Lee et al., 2016b].

Meanwhile, material decomposition can also be realized by directly recognizing different materials. A pixel can contain several materials. To decompose these materials, the

materials in the pixel can be considered as a mixture and the latter can be decomposed into different basis materials. Basis materials here and 'materials' in general are not the same notion. For example, water and PMMA (water-like materials) can be considered a whole and is identified as the basis material water; calcium (Ca) in the spine can be identified as the basis material iodine under certain energy-bin setting, *e.g.* 30-50 kev, 51-61 kev, 62-71 kev, 72-82 kev and 83-130 kev. e et al. proposed a calibrated least squares fitting technique to decompose hydroxyapatite and iodine by a simulation study [Le and Molloi, 2011]. Based on this work, Alessio et al. made further improvement and their decomposition results with carotid endarterectomy specimens suggested the presence of water, lipid, and calcium deposits in the plaque walls [Alessio and MacDonald, 2013]. Zainon et al. used small animal spectral micro-CT with Medipix3 detector (thresholds: 10, 16, 22 and 28keV) to scan the carotid atherosclerotic plaque; water-like, calcium-like and lipid-like tissues were well separated according to histology comparison, but iron was not distinguished from calcium [Zainon, 2012].

### 1.3.2 Virtual monochromatic imaging

Virtual monochromatic spectral images (VMS) or virtual mono-energetic images (MonoE) are reconstructed from a accurately decomposed material images and mass attenuation coefficients [Matsumoto et al., 2011, Wu et al., 2009], which can be calculated in the projection domain or in the image domain. For a given kilo-electron voltage, the object is depicted as if it is imaged with a monochromatic beam at the same kilo-electron voltage. VMS imaging has the potential to reduce beam-hardening artifacts and improve contrast to noise ratio (CNR). Hard X-rays attenuate less than soft X-rays, thus VMS images of higher energy have the potential to reduce beam-hardening [Neuhaus et al., 2017, Yu et al., 2012] and metal artifacts [Wang et al., 2013]. Such VMS images also have the advantage to improve CNR, since the low-energy attenuation carries more contrast [Zhao et al., 2012] and contrast agents at energy around absorption edge (i.e. k-edge in clinical applications) change greatly [Yu et al., 2011].

### 1.3.3 High spatial resolution imaging

PCDs can provide improved spatial resolution and reduced radiation dose compared to conventional CT, because of small charge cluster size and the absence of electronic noise allowing reduced pixel size, the size compared to scintillator and photodiode conventional CT detectors, the absence of dead space between detectors [Iwanczyk et al., 2009]. Consequently, this is leading to sharper edges and better delineation of structures in reconstructed images, with the additional value of decreasing the partial volume effects from small objects [Si-Mohamed et al., 2017a].

### 1.3.4 High contrast imaging

sCT is expected to require less contrast material to be administered to patients than the currently used amounts due to a better CNR (particular at low current dose) [Taguchi and Iwanczyk, 2013, Schirra et al., 2014]. Importantly, sCT provides additional energy information and will allow enhanced contrast of different materials in the body.

There are mainly three enhancement cases in CT imaging: integrating, counting and energy weighting. The first case uses weighting factors that are proportional to the energy of photon; the second case sums up the number of interacting photons with constant weighting factor; and in the third case, the energy-bin data are weighted by energy dependent factor to obtain better CNR and signal-to-noise Ratio (SNR) [Carramate et al., 2011]. By giving lower-energy data more weight, the dose efficiency is effectively improved and enables a higher CNR at a constant patient dose, or a lower dose at a constant CNR [Berglund et al., 2014]. Energy weighting can be performed both in projection domain or image domain data. In the research of Giersch el al., by using weighting factor $E^{-3}$, the SNR can be enhanced by up to from 1.3 to 1.9 or reduce the dose by factor of 2.5 without losing image quality [Giersch et al., 2004]. An "image-based" weighting method by Schmidt shows that the CNR is improved by factors of 1.0 to 1.3 compared to photon counting weighting with negligible beam-hardening artifacts [Schmidt, 2009].

## 1.4 Summary

This chapter presents the general principles of spectral CT, including the following sections:

1. Spectral CT imaging system. Spectral CT system contains three parts: source emitting a flux of x-ray quantum at an object, object interacting with X-ray and detector counting the quantum. The main difference between spectral CT and conventional energy integrating CT or dual-energy CT is the detector. For conventional CT or dual-energy CT, detectors only count photons of different energy in one or two channels. While for spectral CT, the new photon-counting detector (PCD) can register photons in multiple channels.

2. Spectral CT images reconstruction. Reconstruction aims to obtain the spatial-dependent linear attenuation coefficients, which can be performed independently at each bin (separate reconstruction) or jointly by exploiting all spectrum information (joint reconstruction).

3. Applications of spectral CT. Spectral CT employs PCDs and is able to obtain spectral information of several energy bins with single acquisition. PCDs are semiconductor based detectors that have the ability to discriminate transmitted photons corresponding to selected energy bins. Spectral CT imaging enables to overcome many limitations of the previous techniques and opens up many new applications, such as quantitative material decomposition, virtual monochromatic imaging, high spatial resolution imaging and high contrast imaging.

# Chapter 2

# Model of Material Decomposition and Mathematical Foundations

## Contents

## 2.1 State of the art

Compared to conventional energy-integrating CT or dual energy CT, sCT can count the number of photons in multiple energy bins with one single exposure, *i.e.* utilizing spectral information. This advantage enables efficient material decomposition that aims to quantitatively separate different materials present in a pixel.

Different approaches were developed to realize material decomposition: decompose projection data acquired at different energy bins into different material sinograms, each of which corresponds to a material (*i.e.* the so-called basis material), or different physical effects (*e.g.* photoelectric effect, Compton effect and extended K-edge components) based on their energy-dependent characteristics, and then reconstruct individually each spatial material image containing one single material (**projection-domain** approach) [Schlomka et al., 2008, Zimmerman and Schmidt, 2015, Ducros et al., 2017]; or firstly reconstruct the spatial image from each energy bin sinogram and then decompose the reconstructed spatial images corresponding to different energy bins into spatial material images (**image-domain** approach) [Le Huy and Molloi, 2011, Taguchi et al., 2007, Li et al., 2015, Li et al., 2017]; or directly reconstruct spatial material images from projection data (**one-step** approach) [Foygel Barber et al., 2016, Mechlem et al., 2018, Hou et al., 2018].

There is actually another commonly used standard to categorize the material decomposition methods for spectral CT. According to the type of decomposition basis, material decomposition can be divided into two categories: **effect based** and **material based** methods. Effect based approaches aims to decompose data into different physical effects (Figure 1.4a), where the attenuation is considered as a linear combination of the photoelectric effect, Compton effect and extended K-edge components if there are materials with their K-edge within the CT energy range. Material based method is to decompose data into different basis materials (Figure 1.4b), which describes the linear attenuation coefficient by the contributions of a basis of materials.

### 2.1.1 Projection-domain material decomposition

For CT images, the object model of material decomposition is described by:

$$\mu(\vec{x}, E) = \sum_{\alpha=1}^{M} f_\alpha(E) p_\alpha(\vec{x}), \tag{2.1}$$

where $M$ denotes the number of decomposition basis in use, $p_\alpha(\vec{x})$ the physico-chemical or quantity property (depending on the concrete formulation of Equation (2.1)) of the unknown object, and $f_\alpha(E)$ a known function that varies with energy.

#### Projection-domain effect based method (k-edge imaging)

For decomposition using basis effects, $p_\alpha(\vec{x})$ is the physico-chemical property and $f_\alpha(E)$ the energy-dependent characteristic of different physical effect. In the work of [Roessl and Proksa, 2007], $\mu(\vec{x}, E)$ is taken as the combination of photoelectric absorption, Compton scattering and extra K-edge components if there is any K-edge material in the object:

$$\mu(\vec{x}, E) = f_{\text{ph}}(E) p_{\text{ph}}(\vec{x}) + f_{\text{KN}}(E) p_{\text{Co}}(\vec{x}) + \sum_{\alpha=1}^{M-2} \mu_{\text{m}\alpha}(E) \rho_\alpha(\vec{x}), \tag{2.2}$$

where $p_{\mathrm{ph}}(\vec{x})$ and $p_{\mathrm{Co}}(\vec{x})$ represent location dependency of photoelectric absorption and Compton scattering, respectively. $f_{\mathrm{ph}}(E)$ denotes the cross section of photoelectric absorption that can be approximated by $E^{-3}$. $f_{\mathrm{KN}}(E)$ is the cross section of Compton scattering, namely Klein-Nishina function. $\rho_\alpha(\vec{x})$ denotes the density of K-edge material $\alpha$ at point $\vec{x}$ and $\mu_{\mathrm{m}\alpha}(E)$ the mass attenuation coefficient of K-edge material $\alpha$ at energy $E$. $(M-2)$ represents the number of K-edge materials inside the object.

Considering both the measurement process described by Beer-Lambert law and Equation (2.2), we have

$$n_i(p_\alpha) = \sum_{E=E_{\mathrm{s}}(i)}^{E_{\mathrm{f}}(i)} d(E)n_0(E)\exp[-\int \sum_{\alpha=1}^{M} f_\alpha(E)p_\alpha(\vec{x})\,\mathrm{ds}], \tag{2.3}$$

where $n_i$ denotes the expected number of photons at the $i$-th energy bin, $d(E)$ the detector response function, $n_0$ the number of photons in the initial spectrum at energy $E$, and $[E_{\mathrm{s}}(i), E_{\mathrm{f}}(i)]$ the start and final energies of the $i$-th bin, respectively. Equation (2.3) can be rewritten as:

$$\begin{aligned} n_i(P_\alpha) &= \sum_{E=E_{\mathrm{s}}(i)}^{E_{\mathrm{f}}(i)} d(E)n_0(E)\exp[-\sum_{\alpha=1}^{M} f_\alpha(E)\int p_\alpha(\vec{x})\,\mathrm{ds}] \\ &= \sum_{E=E_{\mathrm{s}}(i)}^{E_{\mathrm{f}}(i)} d(E)n_0(E)\exp[-\sum_{\alpha=1}^{M} f_\alpha(E)P_\alpha(sx,sy)] \qquad (2.4) \\ &= \boldsymbol{\mathcal{F}}(\boldsymbol{P}), \qquad (2.5) \end{aligned}$$

with

$$P_\alpha(sx,sy) = \int p_\alpha(\vec{x})\,\mathrm{ds}, \tag{2.6}$$

where $P_\alpha(sx,sy)$ is the line integral of location-dependent parameter $p_\alpha(\vec{x})$ along the measured projection path, $(sx,sy)$ the location of the measured projection in the sinogram, with $sx$ denoting detector pixels and $sy$ denoting measurement angles, and $\boldsymbol{\mathcal{F}}(\boldsymbol{P})$ the forward model of projection-domain decomposition model. To estimate $P_\alpha(sx,sy)$, maximum-likelihood (ML) method is used in [Roessl and Proksa, 2007, Schlomka et al., 2008]. Firstly suppose the detected number of photons $M_i$ form a set of independent Poisson random variables,

$$M_i \sim \mathrm{Poisson}(\mathrm{mean} = n_i(P_\alpha)), \tag{2.7}$$

then the likelihood function as the possibility of measurement result $(M_1 = m_1, M_2 = m_2, \ldots M_N = m_N, )$ can be calculated:

$$P(m_1, ..., m_N | n_1(P_\alpha), ..., n_N(P_\alpha)) = \prod_{i=1}^{N} \frac{n_i(P_\alpha)^{m_i}}{m_i!} \mathrm{e}^{-n_i(P_\alpha)}. \tag{2.8}$$

For computational convenience in seeking the extremum, Equation (2.7) is simplified by applying a negative logarithm operator on both sides and dropping the term that is

unrelated to $P_\alpha$. Then calculating the negative logarithm likelihood function, we will obtain:

$$\begin{aligned} L(P_\alpha) &= -\ln[P(m_1, ..., m_N | n_1(P_\alpha), ..., n_N(P_\alpha)] \\ &= \sum_{i=1}^{N} [n_i(P_\alpha) + \ln m_i! - m_i \ln n_i(P_\alpha)] \\ &\cong \sum_{i=1}^{N} [n_i(P_\alpha) - m_i \ln n_i(P_\alpha)]. \end{aligned} \tag{2.9}$$

By minimizing the above negative log-likelihood function, the line integral of object density $P_\alpha$ can be solved. As we can see in Equation (2.9), $P_\alpha$ is the line integral of $p_\alpha$, thus $p_\alpha$ can be obtained by applying a conventional reconstruction on $P_\alpha$.

The K-edge imaging technology enables specific imaging of high-Z K-edge materials, such as iodine bismuth, gold and gadolinium. These materials are good candidates of contrast agents. In the work of Feuerlein, a partially occluded stent was simulated by using a calcified plaque isoattenuated to a surrounding gadolinium chelate solution. By K-edge imaging, the separated gadolinium image clearly shows perfused lumen of vessel [Feuerlein et al., 2008]. In the work of Pan et al., fibrin-specific bismuth-enriched K-edge nanocolloid (nanoK (Bi)) particles are well enhanced in both spectral CT scans of a blood vessel phantom and carotid artery endarterectomy specimens [Pan and Yang, 2010]. Cormode et al. made *in vivo* experiments using rabbits after injections of gold nanoparticles and iodinated contrast agent, their results show that gold and iodine distributions are clearly differentiated [Cormode et al., 2017].

#### Projection-domain material based method

We have introduced that the attenuation coefficient can be considered as the linear combination of the basis material mass attenuation coefficients weighted by their densities. So we have

$$\begin{aligned} \mu(\vec{x}, E) &= \mu_{\mathrm{m}1}(E)\rho_1(\vec{x}) + \mu_{\mathrm{m}2}(E)\rho_2(\vec{x}) + ... + \mu_{\mathrm{m}M}(E)\rho_M(\vec{x}) \\ &= \sum_{\alpha=1}^{M} \mu_{\mathrm{m}\alpha}(E)\rho_\alpha(\vec{x}), \end{aligned} \tag{2.10}$$

where $\rho_\alpha(\vec{x})$ denotes the density of material $\alpha$ at point $\vec{x}$. Material $\alpha$ is not exclusive to K-edge materials, but also applicable for lighter materials. $\mu_{\mathrm{m}\alpha}(E)$ designates the mass attenuation coefficient of material $\alpha$ at energy $E$, which can be found in NIST database [Saloman and Hubbell, 1986]. $M$ should be smaller than or equal to $N$, otherwise the problem will be under-determined and an infinite number of solutions exist if there are no other equality constraints. The types of materials chosen for decomposition depend on the application and prior knowledge of the scanned objects. Material based decomposition can be solved with the same method of effect based decomposition.

### 2.1.2 Image-domain material decomposition

Image-domain material decomposition works on conventionally reconstructed images $\mu(i, \vec{x})$ for each energy bin $B_i$, which represents energy-resolved linear attenuation co-

efficient. The reconstructed multi-energy images are decomposed into the linear combination of mass attenuation coefficients weighted by the corresponding mass density, described by:

$$\begin{aligned}\mu(\vec{x},i) &= \dot{\mu}_{\mathrm{m}1}(i)\rho_1(\vec{x}) + \dot{\mu}_{\mathrm{m}2}(i)\rho_2(\vec{x}) + ... + \dot{\mu}_{\mathrm{m}M}(i)\rho_M(\vec{x}) \\ &= \sum_{\alpha=1}^{M} \dot{\mu}_{\mathrm{m}\alpha}(i)\rho_\alpha(\vec{x}), \quad i = 1,...,B, \end{aligned} \tag{2.11}$$

where $\dot{\mu}_{m\alpha}(i)$ designates the calculated effective mass attenuation coefficient of the $\alpha$-th basis material at the $i$-th energy bin, $M$ the total number of basis materials, $B$ the total number of energy bins, and $\rho_\alpha(\vec{x})$ the mass density of the $\alpha$-th basis material at pixel $\vec{x}$. The aim of material decomposition is to solve $\rho_\alpha$ from the Equation (2.11).

$$\underbrace{\begin{bmatrix} \mu(\vec{x}_1,1) & \dots & \mu(\vec{x}_{N_P},1) \\ \vdots & \ddots & \vdots \\ \mu(\vec{x}_1,B) & \cdots & \mu(\vec{x}_{N_P},B) \end{bmatrix}}_{\boldsymbol{Y}} = \underbrace{\begin{bmatrix} \dot{\mu}_{m1}(1) & \dots & \dot{\mu}_{mM}(1) \\ \vdots & \ddots & \vdots \\ \dot{\mu}_{m1}(B) & \cdots & \dot{\mu}_{mM}(B) \end{bmatrix}}_{\boldsymbol{M}} \cdot \underbrace{\begin{bmatrix} \rho_1(\vec{x}_1) & \dots & \rho_1(\vec{x}_{N_P}) \\ \vdots & \ddots & \vdots \\ \rho_M(\vec{x}_1) & \cdots & \rho_M(\vec{x}_{N_P}) \end{bmatrix}}_{\boldsymbol{X}}, \tag{2.12}$$

where $\boldsymbol{M}$ denotes the decomposition matrix, each column of which represents the effective mass attenuation coefficients of one basis material for the $B$ energies, $\boldsymbol{Y} \in \mathcal{R}^{B\times N_P}$ and $\boldsymbol{X} \in \mathcal{R}^{M\times N_P}$ the reconstructed multi-energy spatial images containing linear attenuation coefficients $\boldsymbol{\mu}$ and the mass densities $\boldsymbol{\rho}$ of basis materials with $N_p$ indicating the total number of pixels or voxels, respectively. Furthermore, considering the noise, Equation (2.12) can be rewritten as:

$$\begin{aligned}\boldsymbol{Y} &= \boldsymbol{M}\boldsymbol{X} + \boldsymbol{N}, \\ &= \boldsymbol{\mathcal{F}}(\boldsymbol{X}), \end{aligned} \tag{2.13}$$

where $\boldsymbol{N}$ denotes the noise and $\boldsymbol{\mathcal{F}}(\boldsymbol{X})$ the forward model of image-domain decomposition. Theoretically, the decomposition matrix can be initialized by the effective mass attenuation coefficients, calculated using [Le Huy and Molloi, 2011]:

$$\dot{\mu}_{m\alpha}(i) = \frac{\int_{E\in E_i} n_0(E)d(E)\mu_{m\alpha}(E)dE}{\int_{E\in E_i} n_0(E)d(E)dE}, \quad i = 1,...,B, \tag{2.14}$$

where $\mu_{m\alpha}(E)$ is the theoretical mass attenuation coefficient at energy $E$ retrieved from NIST [Saloman and Hubbell, 1986], and $\int_{E\in E_i} n_0(E)dE$ the total number of incident photons belonging to the $i$-th energy bin of width $E_i$. In other words, $\dot{\mu}_{m\alpha}(i)$ represents the averaged value of all the theoretical mass attenuation coefficients inside each single energy bin, which is an estimate of the true mass attenuation coefficient corresponding to that energy bin.

Material-based decomposition has wider applications and also presents the potential to be optimized. Le and Molloi used a calibrated least squares fitting technique in image domain to quantify calcium and iodine [Le Huy and Molloi, 2011] for breast imaging. To assess tissue composition of atherosclerotic plaque, Alessio and and MacDonald used

weighted least-squares method, which assumes that the materials are limited at a certain location to only those contained in one of the pre-selected classes. Therefore, this method firstly segments the image into pre-selected classes, then decomposes the pixel into corresponding materials contained in the class [Alessio and MacDonald, 2013]. Zeng et al. proposed a reconstruction method that uses penalized weighted least-squares scheme incorporating the structure tensor total variation regularization to gain better material decomposition quality [Zeng et al., 2016]. Ducros et al. uses a regularized weighted least squares Gauss-Newton algorithm to decompose the spectral X-ray projection images of a thorax phantom into soft tissue, bone and gadolinium bases [Ducros et al., 2017].

### 2.1.3 One-step material decomposition

Recently, several methods have been proposed which reconstruct material-specific volumes directly from the photon counts. They are commonly referred to as "one-step inversion", or simply "one-step" methods [Cai et al., 2013, Long and Fessler, 2014, Weidinger et al., 2016, Foygel Barber et al., 2016, Mechlem et al., 2018]. All of these methods are iterative: there is currently no analytical inversion formula for the material decomposition problem, let alone for one-step inversion. They consist in combining the forward models of the tomographic reconstruction and the material separation inverse problems, yielding a single (but more complex) forward model, which takes as input a set of material volumes, and yields photon counts as output. In discrete form, the forward model reads

$$\begin{aligned} n &= \sum_{E=E_s(i)}^{E_f(i)} d(E) n_0(E) \exp[-\sum_j a_{ij} \sum_{\alpha=1}^{M} \mu_{m\alpha}(E) \rho_\alpha(\vec{x})], \\ &= \boldsymbol{\mathcal{F}}(\boldsymbol{\rho}), \end{aligned} \tag{2.15}$$

where $a_{ij}$ is the coefficient of the forward projection matrix $A$ at row $i$ and column $j$ (discussed in Equation (1.12)), and $\boldsymbol{\mathcal{F}}(\boldsymbol{\rho})$ the forward model of one-step decomposition. One-step inversion then means finding $\rho_\alpha(\vec{x})$ for which the forward model yields photon counts $n$ as similar as possible to those measured by the scanner.

By construction, the drawbacks of two-step methods are circumvented, and there is no risk of losing information. One-step methods therefore have the potential to yield higher image quality than their two-step counterparts, but they are also slower to converge. This is likely to prevent their use in many applications, as it happened for regularized iterative reconstruction techniques on standard CT. Since in the multi-energy CT case the amount of data contained in a single acquisition is multiplied by the number of energy bins, and the one-step problem is more complex than the reconstruction problem alone, the need for fast methods is even more acute than for standard CT.

## 2.2 Inverse problem of image-domain material decomposition

In this work, we mainly focus on the image-domain material based material decomposition. The problem of solving the image-domain material based material decomposition described in Equation (2.13) is an ill-posed linear inverse problem. A number of methods to solve this kind of problem were reported in the literature. They can be categorized into

two main types: optimization without and with regularization, as:

$$\begin{aligned} \boldsymbol{X} &= \underset{\boldsymbol{X}}{\operatorname{argmin}} \mathcal{D}(\boldsymbol{Y}, \boldsymbol{X}), \\ \boldsymbol{X} &= \underset{\boldsymbol{X}}{\operatorname{argmin}} \mathcal{D}(\boldsymbol{Y}, \boldsymbol{X}) + \lambda \mathcal{R}, \end{aligned} \tag{2.16}$$

where $\boldsymbol{Y} \in \mathbb{R}^{B \times N_P}$ denotes the reconstructed multi-energy spatial images with $N_P$ indicating the total number of pixels or voxels and $B$ the total number of energy bins, $\boldsymbol{M} \in \mathbb{R}^{B \times N_M}$ the decomposition matrix with $N_M$ the total number of basis materials, $\boldsymbol{X} \in \mathbb{R}^{N_M \times N_P}$ the decomposed basis material images of mass densities $\boldsymbol{\rho}$, $\mathcal{D}$ the discrepancy function, $\mathcal{R}$ the regularization term, and $\lambda$ a global regularization parameter. Generally, $\mathcal{D}$ is calculated using Euclidean distance:

$$\mathcal{D} = \|\boldsymbol{Y} - \boldsymbol{\mathcal{F}}(\boldsymbol{X})\|_F^2, \tag{2.17}$$

where $\|\cdot\|_F$ denotes Frobenius norm for Euclidean distance. The Frobenius norm is matrix norm of a $m \times n$ matrix $A$ defined as the square root of the sum of the absolute squares of its elements:

$$\|A\|_F = \sqrt{\sum_{i=1}^{m} \sum_{j=1}^{n} |a_{ij}|^2}. \tag{2.18}$$

Note that for projection-domain material decomposition, some literatures reported that $\mathcal{D}$ can use weighted Euclidean distance adapted to data corrupted by Poisson noise:

$$\mathcal{D} = \|\boldsymbol{n}_i - \boldsymbol{\mathcal{F}}(\boldsymbol{P})\|_W^2. \tag{2.19}$$

Considering the more complex noise condition of reconstructed sCT images, we choose Euclidean distance in our proposed image-domain material decomposition.

The pseudo-inverse method with singular value decomposition (SVD) is a usual optimization method without regularization [Faby et al., 2014], as:

$$\boldsymbol{X} = \boldsymbol{M}^{+} \boldsymbol{Y}, \tag{2.20}$$

where $\boldsymbol{M}^{+}$ is the pseudo-inverse of $\boldsymbol{M}$ solved by SVD. The SVD of a matrix $A$ is the factorization of $A$ into the product of three matrices $A = UDV^T$ where the columns of $U$ and $V$ are orthonormal and the matrix $D$ is diagonal with positive real entries. The following formula can be used to find the pseudo-inverse of $A$: $A^{+} = VD^{+}U^T$.

In the optimization method with regularization, sparse representation was often employed as that multi-energy data often has high correlation. The major motivation of sparse representation is to make use of the sparsity nature of multi-dimensional data. An appropriate sparse representation can give an accurate material decomposition with few energy bins. Typically, sparse representation via L1 norm minimization is considered efficient in many areas [Donoho, 2006, Candes et al., 2006] to prevent oversmoothing,

$$\|\boldsymbol{Y} - \boldsymbol{\mathcal{F}}(\boldsymbol{X})\|_F^2 + \|\boldsymbol{X}\|_1, \tag{2.21}$$

where $\|\cdot\|_1$ is L1 norm, *i.e.* $\|\boldsymbol{X}\|_1 = \sum_{i=1}^{m} \sum_{j=1}^{n} |x_{ij}|$. Other methods based on sparse representation were also studied for material decomposition, including gradient sparsity via bilateral total variation (BTV) [Touch et al., 2016] and sparse transform via tight frame [Gao et al., 2011].

### 2.2.1 Unreliability in image-domain material decomposition

The performance of the image-domain material decomposition (2.15) is influenced by both the quality of the reconstructed spatial images $\boldsymbol{Y}$ and the separation ability of $\boldsymbol{M}$. The quality of spatial images $\boldsymbol{Y}$ is deteriorated by data inconsistency stemming from the aforementioned PCD limitations and artifacts associated with reconstruction algorithm. Reconstruction being a preliminary step to image-domain material decomposition, errors in the reconstructed spatial images can degrade the subsequent decomposition, *e.g*. severe noise and beam-hardening artifacts, *etc* [Elbakri and Fessler, 2002]. The separation ability of $\boldsymbol{M}$ is limited by the interference between its basis materials, which is caused by the presence of similar basis materials having close $\mu_m$ and their low estimation precision. The data inconsistency causes false pixel similarity, called $\mu$-similarity in spatial images, while the basis material interference causes false basis materials similarity, called $\mu_m$-similarity.

More precisely, $\mu$-similarity implies that distinction between different mixtures in spatial images can be rendered difficult by data inconsistency. To explain the similarity between basis materials, we illustrate in Fig. 2.1 two linear attenuation coefficient ($\mu$) curves corresponding respectively to mixtures 1 and 2 (which have different components or different mass densities; for instance, in this figure, mixtures 1 and 2 correspond respectively to the dilutions of gadolinium (mass density 2 mg/cc) and iodine (1 mg/cc)). The five circle points indicate the theoretical values at five different energy bins (*i.e*. 30-50 keV, 51-61 keV, 62-71 keV, 72-82 keV and 83-130 keV). Even in the ideal case, mixtures 1 and 2 cannot be totally distinguished due to their low mass densities. Moreover, data inconsistency, related to the strong quantum noise, can make that the measured $\mu$ value is not exactly equal to the theoretical one at a given energy bin. On the contrary, the measured value for the same mixture at the same energy bin can vary with pixel position. In other words, in the same image region containing the same mixture, different pixels that contain the same mixture can have different $\mu$ values. This is reflected in Fig. 2.1 by the observation that the $\mu$ value (blue or red points) at a given energy bin slips vertically around the theoretical value, thus creating an uncertainty interval. In the interval where blue and red points overlap, we can no longer distinguish which $\mu$ value corresponds to which mixture. Such $\mu$-similarity between different mixtures (materials) can degrade the subsequent decomposition.

$\mu_m$-similarity results from material interference between the basis materials inside $\boldsymbol{M}$, which makes it difficult to reliably separate basis materials having close $\mu_m$. Moreover, the interference is more severe for image-domain material decomposition considering that the effective mass attenuation coefficient $\dot{\mu}_m$ involved in (2.7) is an averaged value and the low precision can magnify the similarity between basis materials. It is then necessary to obtain $\dot{\mu}_m$ from calibration phantom containing materials of known concentrations [Clark and Badea, 2014], which is adopted in the present study. However, while this approach helps to improve the precision of $\dot{\mu}_m$, the material interference stemming from close $\mu_m$ is still obvious. Actually, $\mu_m$-similarity leads material decomposition to an ill-conditioned problem. To cope with this ill-conditioned problem, existing basis material optimization methods, *e.g*. $\mu_m$-preconditioning methods, utilize linear combination of original basis materials to create synthetic materials, such that $\widetilde{\boldsymbol{M}} = \boldsymbol{MP}$, where $\boldsymbol{P}$ represents the transform matrix and $\widetilde{\boldsymbol{M}}$ the synthetic materials. $\mu_m$-preconditioning strategy

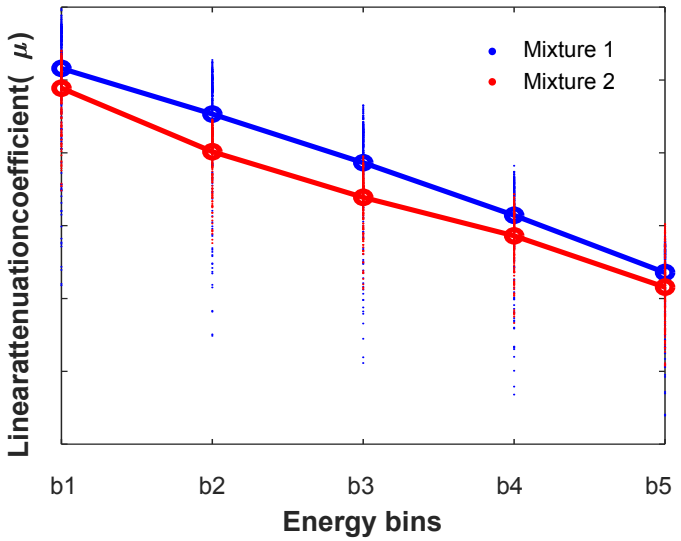


Figure 2.1: Similarity attenuation coefficient curves of two basis materials. The two curves represent two different mixtures, where mixture 1 and mixture 2 are respectively dilutions of gadolinium (2 mg/cc) and iodine (1 mg/cc). The circle points represent theoretical values of the mixtures at five different energy bins. At each energy bin, the blue or red points slip vertically around their theoretical value, thus creating an overlapped interval.

aims to improve the overall condition of material decomposition to increase the algorithm efficiency [Foygel Barber et al., 2016] rather than the reliability of material decomposition.

In short, the unreliability of material decomposition resulting from both $\mu$- and $\mu_m$-similarity still remains a persistent problem.

In this thesis, we proposed three different methods for reliable and accurate material decomposition, respectively discussed in Chapter III, IV and V.

### 2.2.2 Optimization method of material decomposition

All of the proposed methods are solved by alternating direction method of multipliers (ADMM) [Boyd et al., 2010], a simple but powerful algorithm that is well suited to distributed convex optimization, and in particular to problems arising in applied statistics and machine learning.

ADMM is an algorithm that is intended to blend the decomposability of dual ascent with the superior convergence properties of the method of multipliers. The algorithm solves problems in the form

$$\begin{aligned} &\text{minimized} f(x) + g(x), \\ &s.t. \quad Ax + Bz = c, \end{aligned} \tag{2.22}$$

with variable $x \in \mathcal{R}^n$ and $z \in \mathcal{R}^m$, where $A \in \mathcal{R}^{p\times n}$, $B \in \mathcal{R}^{p\times m}$, and $c \in \mathcal{R}^p$. We will assume that $f$ and $g$ are convex. The optimal value of the problem (2.22) will be denoted

by

$$p^* = \inf\{f(x) + g(x) | Ax + Bz = c\}. \tag{2.23}$$

As in the method of multipliers, we form the augmented Lagrangian

$$L_p(x,z,y) = f(x) + g(x) + y^T(Ax + Bz = c) + (\rho/2)\|Ax + Bz = c\|_2^2. \tag{2.24}$$

ADMM consists of the iterations

$$x^{k+1} = \underset{x}{\operatorname{argmin}}\, L_p(x,z^k,y^k), \tag{2.25}$$

$$z^{k+1} = \underset{z}{\operatorname{argmin}}\, L_p(x^{k+1},z,y^k), \tag{2.26}$$

$$y^{k+1} = y^k + \rho(Ax^{k+1} + Bz^{k+1} - c), \tag{2.27}$$

where $\rho$. The algorithm is very similar to dual ascent and the method of multipliers: it consists of an x-minimization step (2.25), a z-minimization step (2.26), and and a dual variable update (2.27). As in the method of multipliers, the dual variable update uses a step size equal to the augmented Lagrangian parameter $\rho$. In ADMM, $x$ and $z$ are updated in an alternating or sequential fashion, which accounts for the term alternating direction.

## 2.3 Summary

This chapter presents the principles of material decomposition in spectral CT, including the following sections:

1. State of the art of material decomposition. Different approaches were developed to realize material decomposition: projection-domain approach - decompose projection data acquired at different energy bins into different material sinograms, each of which corresponds to a material (*i.e*. the so-called basis material), or different physical effects (*e.g*. photoelectric effect, Compton effect and extended K-edge components) based on their energy-dependent characteristics, and then reconstruct individually each spatial material image containing one single material; image-domain approach - firstly reconstruct the spatial image from each energy bin sinogram and then decompose the reconstructed spatial images corresponding to different energy bins into spatial material images; one-step approach - directly reconstruct spatial material images from projection data.

2. Inverse problem of image-domain material decomposition. Solving material decomposition is an inverse problem. Common methods were introduced, e.g pseudo-inverse method with singular value decomposition, method with sparsity regularization, and method with total variation (TV) regularization, *etc*. Meanwhile, the bottlenecks of image-domain material decomposition were introduced, including $\mu$-similarity and $\mu_m$-similarity. At last, the optimization method utilized in our works was discussed.

# Chapter 3

# Material Decomposition in Spectral Photon-Counting CT Using Multiple Constraints in Image Domain

## Contents

## 3.1 Introduction

sCT has recently received increasingly intensive attention, due to the new advances in photon-counting detector technology. Compared to conventional energy integrating CT or dual-energy CT, spectral CT can count the number of photons in separated energy bins with one single exposure [Faby et al., 2015]. Thanks to this advantage, it becomes possible to decompose efficiently different materials (basis materials) present in the same pixel of spectral CT images, which provides promising perspectives for both medical applications and industrial nondestructive evaluation.

According to the type and number of basis materials, material decomposition in spectral CT can be an ill-posed, or even ill-conditioned inverse problem. Such problem can arise before [Schlomka et al., 2008, Zimmerman and Schmidt, 2015, Ducros et al., 2017], during [Foygel Barber et al., 2016, Mechlem et al., 2018, Hou et al., 2018], or after [Taguchi et al., 2007, Le Huy and Molloi, 2011, Faby et al., 2014, Li et al., 2015, Li et al., 2017] image reconstruction process. A number of material decomposition methods were reported in the literature. They can be categorized into two main types: optimization without and with regularization. The pseudo-inverse method with singular value decomposition (SVD) is a usual optimization method without regularization [Faby et al., 2014]. In the optimization method with regularization, sparse representation was often employed as that multi-energy data often has high correlation. The major motivation of sparse representation is to make use of the sparsity nature of multi-dimensional data. An appropriate sparse representation can give an accurate material decomposition with few energy bins. Typically, sparse representation via L1-norm minimization is considered efficient in many areas [Candes et al., 2006, Donoho, 2006] to prevent oversmoothing. Other methods based on sparse representation were also studied for material decomposition, including gradient sparsity via bilateral total variation (BTV) [Clark and Badea, 2014] and sparse transform via tight frame [Gao et al., 2011]. All the above-cited methods were developed in overdetermined cases; no work is available for material decomposition in underdetermined cases where the number of basis materials is greater than that of energy bins.

Actually, in practice an object always contains multiple materials and we do not know a priori what exactly the number of materials in it is. Therefore, material decomposition in underdetermined cases remains a practical problem. The fact that basis materials with close atomic numbers have similar mass attenuation coefficients comes to worsen the problem. To cope with these problems, we propose to use the joint sparsity [Nie et al., 2010] characteristics of both spectrum and space information. Moreover, since neighboring pixels have similar materials, we exploit the joint sparsity in local small patches. Meanwhile, we also make use of the structural low-rank property that the decomposed materials in the corresponding local small patch should share the same edge, due to the local property that, in a local patch, a decomposed material is either present or absent at each pixel of the patch. Finally, since the mass density of materials has always limited value, we introduce a bound constraint on mass density. All that leads us to propose a material decomposition method based on bounded mass Density, local joint Sparsity and structural low-Rank (DSR).

## 3.2 Material decomposition using multiple constraints

For spectral CT images, basis materials with close atomic numbers have similar mass attenuation coefficients, and this is the source of ill-conditioned problems and constitutes the main bottleneck that limits the performance of material decomposition methods. To cope with this problem, we propose to find the main features by exploiting the similarities in multi-dimensional data. To this end, we use a sparse representation method that allowing processing the high correlation of both spectral and spatial dimensions. Such joint sparsity of spectral and spatial dimensions would be interesting for decomposing similar materials in a robust way.

Such joint sparsity of spectral and spatial dimensions would be interesting for decomposing similar materials in a robust way. We then adopt the mixed L2,1-norm that is particularly suitable for small patches to combine the information. The norm L2,1 is defined by:

$$\|\boldsymbol{X}\|_{2,1} = \sum_{i=1}^{I} \sqrt{\sum_{j=1}^{J} x_{ij}^2}, \tag{3.1}$$

where $x_{ij}$ is the mass density of the $i$-th basis material at the $j$-th pixel in $\boldsymbol{X}$.

L2,1-norm can enforce a small number of nonzero rows in $\boldsymbol{X}$, compared to usual L1-norm that tends to give sparse solution pixel by pixel. In other words, L1-norm limits the number of basis materials exiting in one pixel, while L2,1-norm enforces pixels to share the same atoms of basis materials in each local small patch. For the present application of spectral CT images, the L2,1-norm allows us to combine space (rows in X) and spectrum (columns in X) information.

At the same time, in addition to the spectral and spatial similarities, multi-energy images also present the structural coherence, which reflects the fact that the decomposed materials should share the same edges in the same small patch due to their local property in the image. Such edge information in a material image is also sparse and can be captured by gradient operator. To process the edge similarities, we utilize low-rank representation on the gradient matrices of all the decomposed materials. The low-rank constraint is realized via nuclear norm that is the convex envelope of matrix rank [Candès et al., 2011]. As a result, the structural low-rank (SL) is calculated using:

$$\|\bigtriangledown \boldsymbol{X}\|_* = \sum_{i=1}^{I} \sigma_i(\Delta \boldsymbol{X}), \tag{3.2}$$

where $\bigtriangledown \boldsymbol{X}$ is the gradient matrix of X and $\|\bigtriangledown \boldsymbol{X}\|_*$ is the nuclear norm equal to the sum of its singular values $\sigma_i(\Delta \boldsymbol{X})$. Actually, this kind of rank-sparsity encouraging norm has also been discussed in color image denoising, with the name total nuclear variation (TNV) [Holt, 2014]. However, in the present study, it is utilized to process the structural similarity that existing material images Xi (nonzero rows in X of equation (2)) should share the same edges. A cost function containing the joint sparsity and low-rank regularizations and a data-fidelity term may give an optimal solution to the problem of material decomposition. We then formulate our material decomposition method based on local

joint sparsity and structural low-rank as:

$$\underset{X}{\operatorname{argmin}} \frac{1}{2}\|\boldsymbol{Y_P} - \boldsymbol{M}\boldsymbol{X_P}\|_F^2 + \lambda_1\|\boldsymbol{X_P}\|_{2,1} + \lambda_2\|\bigtriangledown \boldsymbol{X_P}\|_*, \tag{3.3}$$

where $\boldsymbol{Y_P}$ and $\boldsymbol{X_P}$ denote the patches extracted respectively from the reconstructed images and the decomposed material images $\lambda_1$ and $\lambda_2 > 0$ are the scalar regularization parameters. At the same time, since the mass density of materials always has limited value, we introduce the bound constraints into equation (3.3). In other words, the mass densities of materials should be lower bounded by a nonnegative number and upper bounded by a reasonable limit. Thus, after taking into account the multiple constraints of bounded mass Density, local joint Sparsity and structural low-Rank (DSR), our material decomposition model becomes:

$$\underset{X}{\operatorname{argmin}} \frac{1}{2}\|\boldsymbol{Y_P} - \boldsymbol{M}\boldsymbol{X_P}\|_F^2 + \lambda_1\|\boldsymbol{X_P}\|_{2,1} + \lambda_2\|\bigtriangledown \boldsymbol{X_P}\|_* + \text{bound}_l(\boldsymbol{X_P}) + \text{bound}_u(\boldsymbol{X_P}), \tag{3.4}$$

where $\text{bound}_l(\boldsymbol{X_P})$ and $\text{bound}_u(\boldsymbol{X_P})$ denote the lower and upper mass density bounds, respectively.

## 3.3 DSR: solution algorithm by ADMM

The minimization problem of (3.4) is solved by the alternating direction method of multipliers (ADMM) [Boyd et al., 2010]. Firstly, we form the augmented Lagrangian for problem (3.4):

$$\begin{aligned}
&L_\lambda(\boldsymbol{V_1}, \boldsymbol{V_2}, \boldsymbol{V_3}, \boldsymbol{V_4}, \boldsymbol{X}) = \\
&\underset{\boldsymbol{V_1},\boldsymbol{V_2},\boldsymbol{V_3},\boldsymbol{V_4},\boldsymbol{X}}{\arg\min} \frac{1}{2}\|\boldsymbol{Y_P} - \boldsymbol{V_1}\|F^2 + \lambda_1\|\boldsymbol{V_2}\|_{2,1} + \lambda_2\|\boldsymbol{V_3}\|_* + \text{bound}_l(\boldsymbol{V_4}) + \text{bound}_l(\boldsymbol{V_5}) \\
&+ \frac{\tau}{2}\|\boldsymbol{M}\boldsymbol{X_P} - \boldsymbol{V_1} - \boldsymbol{D_1}\|_F^2 + \frac{\tau}{2}\|\boldsymbol{X_P} - \boldsymbol{V_2} - \boldsymbol{D_2}\|_F^2 \\
&+ \frac{\tau}{2}\|\nabla \boldsymbol{X_P} - \boldsymbol{V_3} - \boldsymbol{D_3}\|_F^2 + \frac{\tau}{2}\|\boldsymbol{X_P} - \boldsymbol{V_4} - \boldsymbol{D_4}\|_F^2 + \frac{\tau}{2}\|\boldsymbol{X_P} - \boldsymbol{V_5} - \boldsymbol{D_5}\|_F^2,
\end{aligned} \tag{3.5}$$

where $\tau > 0$ is the augmented Lagrangian parameter.

ADMM consists of the following iterations:

$$\boldsymbol{X_P}^{t+1} \leftarrow \arg\min_{\boldsymbol{X_P}} \frac{\tau}{2}\left\|\boldsymbol{M}\boldsymbol{X_P} - \boldsymbol{V_1}^t - \boldsymbol{D_1}^t\right\|_F^2 + \frac{\tau}{2}\left\|\boldsymbol{X_P} - \boldsymbol{V_2}^t - \boldsymbol{D_2}^t\right\|_F^2 + \frac{\tau}{2}\left\|\nabla\boldsymbol{X_P} - \boldsymbol{V_3} - \boldsymbol{D_3}\right\|_F^2$$
$$+ \frac{\tau}{2}\left\|\boldsymbol{X_P} - \boldsymbol{V_4}^t - \boldsymbol{D_4}^t\right\|_F^2 + \frac{\tau}{2}\left\|\boldsymbol{X_P} - \boldsymbol{V_5}^t - \boldsymbol{D_5}^t\right\|_F^2, \tag{3.6}$$

$$\boldsymbol{V_1}^{t+1} \leftarrow \arg\min_{\boldsymbol{V_1}} \frac{1}{2}\left\|\boldsymbol{Y_P} - \boldsymbol{V_1}\right\|_F^2 + \frac{\tau}{2}\left\|\boldsymbol{M}\boldsymbol{X_P}^t - \boldsymbol{V_1} - \boldsymbol{D_1}^t\right\|_F^2, \tag{3.7}$$

$$\boldsymbol{V_2}^{t+1} \leftarrow \arg\min_{\boldsymbol{V_2}} \lambda_1\left\|\boldsymbol{V_2}\right\|_{2,1} + \frac{\tau}{2}\left\|\boldsymbol{X_P}^t - \boldsymbol{V_2} - \boldsymbol{D_2}^t\right\|_F^2, \tag{3.8}$$

$$\boldsymbol{V_3}^{t+1} \leftarrow \arg\min_{\boldsymbol{V_3}} \lambda_2\left\|\boldsymbol{V_3}\right\|_* + \frac{\tau}{2}\left\|\nabla\boldsymbol{X_P} - \boldsymbol{V_3} - \boldsymbol{D_3}\right\|_F^2, \tag{3.9}$$

$$\boldsymbol{V_4}^{t+1} \leftarrow \arg\min_{\boldsymbol{V_4}} \text{bound}_l(\boldsymbol{V_4}) + \frac{\tau}{2}\left\|\boldsymbol{X_P}^t - \boldsymbol{V_4} - \boldsymbol{D_4}^t\right\|_F^2, \tag{3.10}$$

$$\boldsymbol{V_5}^{t+1} \leftarrow \arg\min_{\boldsymbol{V_5}} \text{bound}_u(\boldsymbol{V_5}) + \frac{\tau}{2}\left\|\boldsymbol{X_P}^t - \boldsymbol{V_5} - \boldsymbol{D_5}^t\right\|_F^2. \tag{3.11}$$

Equations (3.6) to (3.11) aim to solve primal variables $\boldsymbol{X_P}$, $\boldsymbol{V_1}$, $\boldsymbol{V_2}$, $\boldsymbol{V_3}$, $\boldsymbol{V_4}$ and $\boldsymbol{V_5}$. Equation (3.8) is processed by the algorithm FOCUSS [Kowalski et al., 2009, Rao and Kreutz-Delgado, 1999], and equation (3.9) by the singular value thresholding (SVT) method [Cai et al., 2010]. The solutions of $\boldsymbol{X_P}$, $\boldsymbol{V_1}$, $\boldsymbol{V_2}$, $\boldsymbol{V_3}$, $\boldsymbol{V_4}$ and $\boldsymbol{V_5}$ are given by:

$$\boldsymbol{X_P}^{t+1} = (\boldsymbol{M^T M} + \nabla^T\nabla + 3\boldsymbol{I})^{-1}[\boldsymbol{A^T}(\boldsymbol{V_1}^t + \boldsymbol{D_1}^t) + (\boldsymbol{V_2}^t + \boldsymbol{D_2}^t)$$
$$+ \nabla^T(\boldsymbol{V_3}^t + \boldsymbol{D_3}^t) + (\boldsymbol{V_4}^t + \boldsymbol{D_4}^t) + (\boldsymbol{ub} - \boldsymbol{V_5}^t - \boldsymbol{D_5}^t)], \tag{3.12}$$

$$\boldsymbol{V_1}^{t+1} = \frac{1}{1+\tau}\left[\boldsymbol{Y_P} + \tau(\boldsymbol{M}\boldsymbol{X_P}^t - \boldsymbol{D_1}^t)\right], \tag{3.13}$$

$$\boldsymbol{V_2}^{t+1} = (\boldsymbol{X_P}^t - \boldsymbol{D_2}^t)\cdot(\boldsymbol{I} - \frac{\lambda_1/\tau}{\left\|\boldsymbol{X_P}^t - \boldsymbol{D_2}^t\right\|_2})^+, \tag{3.14}$$

$$\boldsymbol{V_3}^{t+1} = SVT(\nabla\boldsymbol{X_P} - \boldsymbol{D_3}, \frac{\lambda_2}{\tau}), \tag{3.15}$$

$$\boldsymbol{V_4}^{t+1} = (\boldsymbol{X_P}^t - \boldsymbol{D_4}^t)^+, \tag{3.16}$$

$$\boldsymbol{V_5}^{t+1} = (\boldsymbol{ub} - \boldsymbol{X_P}^t - \boldsymbol{D_5}^t)^+, \tag{3.17}$$

where $\boldsymbol{ub}$ is the upper bound vector and $(\boldsymbol{x})^+ = \max(\boldsymbol{x}, 0)$.

For clarity, the detail of ADMM for the DSR decomposition method is given in Algorithm 1. The iteration will stop when the criterion of ADMM is satisfied, e.g. the residuals are small enough.

## 3.4 Experiments and results

Two methods were compared with the proposed DSR method: (a) pseudo-inverse with SVD, (b) regularization method with L1-norm constraint (L1). For clarity, we rewrite the models of the three methods as below:

**Algorithm 1 ADMM for the DSR decomposition method**

**Input:** $\boldsymbol{Y_P}, \boldsymbol{M}$

**Initialization:** $\lambda_1$, $\lambda_2$, $\tau$, $\boldsymbol{V_1}$, $\boldsymbol{V_2}$, $\boldsymbol{V_3}$, $\boldsymbol{V_4}$ , $\boldsymbol{V_5}$, $\boldsymbol{D_1}$, $\boldsymbol{D_2}$, $\boldsymbol{D_3}$, $\boldsymbol{D_4}$, $\boldsymbol{D_5}$

**Repeat:**

**Calculate:** $\boldsymbol{X_P}^{t+1} = (\boldsymbol{M^T M} + \nabla^T\nabla + 3\boldsymbol{I})^{-1}[\boldsymbol{A^T}(\boldsymbol{V_1}^t + \boldsymbol{D_1}^t) + (\boldsymbol{V_2}^t + \boldsymbol{D_2}^t) + \nabla^T(\boldsymbol{V_3}^t + \boldsymbol{D_3}^t) + (\boldsymbol{V_4}^t + \boldsymbol{D_4}^t) + (\boldsymbol{ub} - \boldsymbol{V_5}^t - \boldsymbol{D_5}^t)]$

**Calculate:** $\boldsymbol{V_1}^{t+1} = \frac{1}{1+\tau}\left[\boldsymbol{Y_P} + \tau(\boldsymbol{M X_P}^t - \boldsymbol{D_1}^t)\right]$

**Calculate:** $\boldsymbol{V_2}^{t+1} = (\boldsymbol{X_P}^t - \boldsymbol{D_2}^t) \cdot (\boldsymbol{I} - \frac{\lambda_1/\tau}{\left\|\boldsymbol{X_P}^t - \boldsymbol{D_2}^t\right\|_2})^+$

**Calculate:** $\boldsymbol{V_3}^{t+1} = SVT(\nabla \boldsymbol{X_P} - \boldsymbol{D_3}, \frac{\lambda_2}{\tau})$

**Calculate:** $\boldsymbol{V_4}^{t+1} = (\boldsymbol{X_P}^t - \boldsymbol{D_4}^t)^+$

**Calculate:** $\boldsymbol{V_5}^{t+1} = (\boldsymbol{ub} - \boldsymbol{X_P}^t - \boldsymbol{D_5}^t)^+$

**Update Lagrange multipliers:** $\boldsymbol{D_1}$, $\boldsymbol{D_2}$, $\boldsymbol{D_3}$, $\boldsymbol{D_4}$, $\boldsymbol{D_5}$

**Output:** $\boldsymbol{X_P}$

- Pseudo-inverse with SVD:

  $\boldsymbol{X} = \boldsymbol{M}^+\boldsymbol{Y}$,

- L1:

  $\underset{\boldsymbol{X}}{\operatorname{argmin}} \frac{1}{2}\|\boldsymbol{Y} - \boldsymbol{M X}\|_F^2 + \lambda\|\boldsymbol{X}\|_1 + \text{bound}_l(\boldsymbol{X_P}) + \text{bound}_u(\boldsymbol{X_P})$,

- DSR:

  $\underset{\boldsymbol{X}}{\operatorname{argmin}} \frac{1}{2}\|\boldsymbol{Y_P} - \boldsymbol{M X_P}\|_F^2 + \lambda_1\|\boldsymbol{X_P}\|_{2,1} + \lambda_2\|\bigtriangledown \boldsymbol{X_P}\|_* + \text{bound}_l(\boldsymbol{X_P}) + \text{bound}_u(\boldsymbol{X_P})$.

**Image quality metrics**

The performance of the proposed material decomposition was quantitatively evaluated using different metrics. The normalized Euclidean distance was utilized for the accuracy [Ducros et al., 2017], considering its better evaluation for various concentrations compared to the common metric mean squared error. Given both the $m$-th decomposed basis materials $\boldsymbol{x}_m$ and ground-truth $\boldsymbol{x}_m^{gt}$, the normalized Euclidean distance is:

$$error_m = \frac{\|\boldsymbol{x}_m - \boldsymbol{x}_m^{gt}\|_2}{\|\boldsymbol{x}_m^{gt}\|_2}. \tag{3.18}$$

The smaller the normalized Euclidean distance, the more accurate the decomposition precision.

The performance of the proposed DSR method was evaluated on both digital and physical data.

### 3.4.1 Digital data

The projection data of spectral CT was simulated using INSA software Virtual X-ray Imaging (VXI) [Duvauchelle et al., 2000] and then reconstructed by the method FBP. The

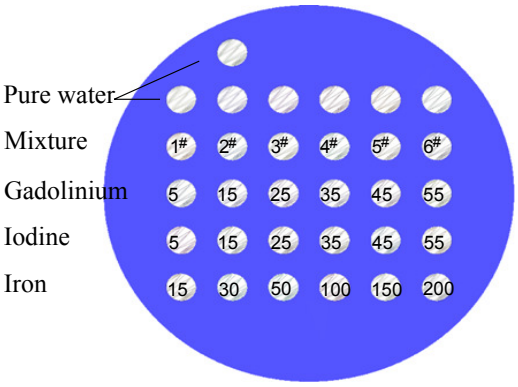


Figure 3.1: Digital phantom.

reconstructed phantom has 800 * 800 pixels and contains five materials: water, Polymethyl Methacrylate (PMMA), gadolinium (Gd), iodine (I) and iron (Fe), as shown in figure 3.1. The number on each disk designates the concentration of materials (mg/cc). Note that the disk with # stands for mixture inserts that contain three basis materials (Gd, I and Fe) with the same concentration in each column. The X-ray energy bins were set as: 30-40kev, 40-50kev, 50-60kev, 60-70kev and 70-80kev. The number of energy bins 5 are selected in terms of the setting of Philips prototype.

To fully evaluate the impacts of noise, we list the results of material decomposition based on reconstructed image without and with Poisson noise. Meanwhile, decomposition on different basis materials were tested, in terms of the enormous effects of category and number of basis materials. Furthermore, the impacts of low-energy bins were evaluated, on which the decomposition results are shown.

**Without Poisson noise**

The decomposition results of five existing basis materials (water, PMMA, iron, iodine and gadolinium) are shown in figure 3.2. Note that in the present study, the lower mass density bound is set as 0 and the upper bound as 10 times of the maximum mass density value of existing materials. The method pseudo-inverse with SVD can not quantify the 5 existing basis materials. It can be partly explained by the condition number $\kappa(A)$ of matrix, which is equal to the ratio of the largest to smallest singular value, and is used to measure how sensitive a function is to errors in the input [Vacca, 1981]. A problem with a high condition number is ill-conditioned. In our experiments, there are 20 similar basis materials, leading to a big condition number $\kappa(A) = 1.7 \times 10^5$, which implies that the result of usual pseudo-inverse with SVD is not reliable for our ill-condition problem. Therefore, we will focus on the other two methods.

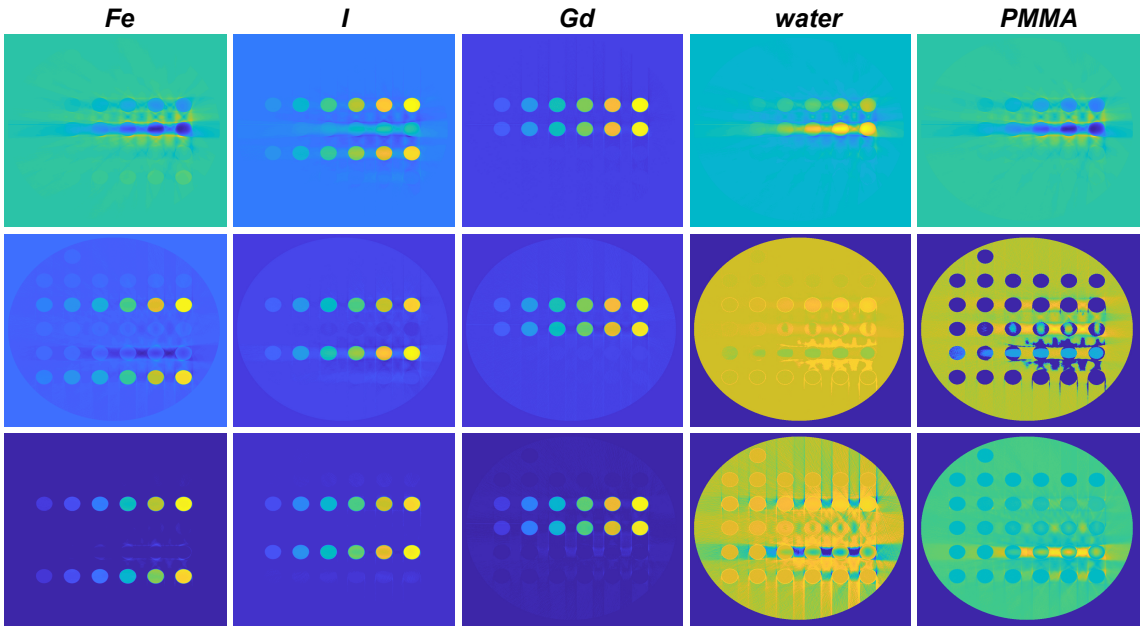


Figure 3.2: The results of material decomposition based on reconstructed sTC images without Poisson noise for the three methods: 5 energy bins, 5 basis materials. Top to bottom: Pseudo-inverse with SVD, L1 and DSR.

As can be seen in figure 3.2, the proposed DSR method has higher decomposition accuracy compared to the L1 method. Even for the material without k-edge (Fe), DSR shows good ability in detection and quantification. For more quantitative analysis, we compare the mass density of Fe, I and Gd in the corresponding rows. The results indicate that DSR has good decomposition ability for all of iron, iodine and gadolinium, as shown in figure 3.3. In contrast, L1 yields much lower density of iron and higher density of iodine compared to the theoretical values.

**Effects of basis materials**

To evaluate the impacts of basis materials for the proposed decomposition methods, we considered 20 materials as basis materials divided into 4 categories, including the five materials (bold ones) present in the phantom, as listed in Table 3.1. Because most elements in the human body have relatively small atomic numbers, we put low-Z elements: sodium (Na), magnesium (Mg), aluminum (Al), silicon (Si), phosphorus (P), sulfur (S), chlorine (Cl), argon (Ar) and potassium (K) into the basis materials as category 1. Manganese (Mn), cobalt (Co), copper (Cu) and zinc (Zn) were selected for comparison with Fe, as category 2. To test the accuracy of I and Gd, another common contrast agent xenon (Xe) was also added, as category 3. Bone was selected to test the accuracy of water and PMMA because of their similar attenuation coefficients. The mass attenuation coefficients were retrieved from National Institute of Standards and Technology (NIST) [Saloman and Hubbell, 1986].

To make a comprehensive evaluation of the proposed DSR, the results of material decomposition for the remaining categories of basis materials in Table 3.1 are given in

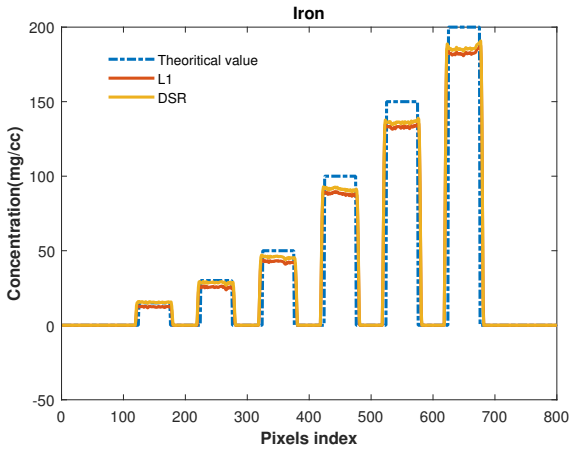


(a)

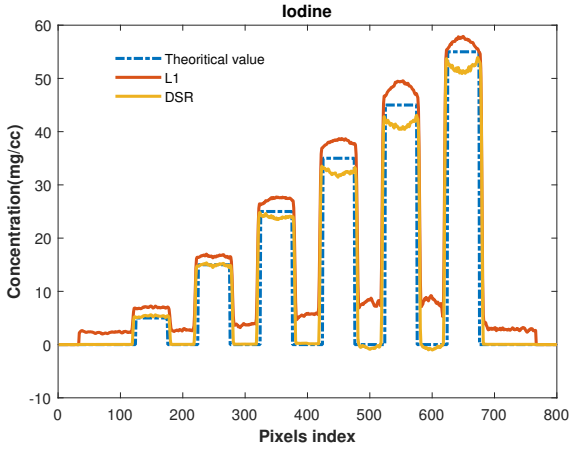


(b)

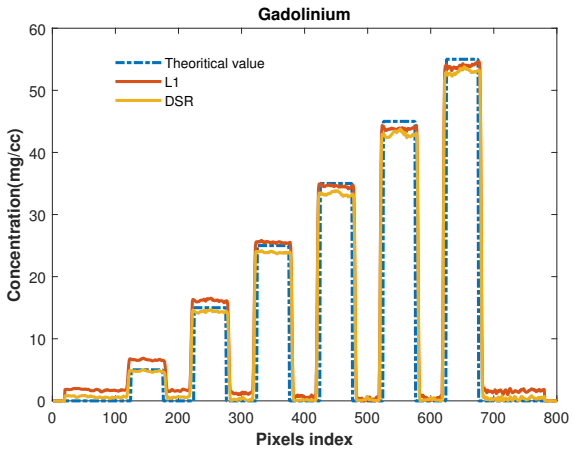


(c)

Figure 3.3: The mass densities of iron, iodine and gadolinium: 5 energy bins.

Table 3.1: Basis materials and the corresponding atomic numbers.

| | | | | | | | | | | |
|---|---|---|---|---|---|---|---|---|---|---|
| Category 1 | M | Na | Mg | Al | Si | P | S | Cl | Ar | K |
| | Z | 11 | 12 | 13 | 14 | 15 | 16 | 17 | 18 | 19 |
| Category 2 | M | Mn | ***Fe*** | Co | Cu | Zn | | | | |
| | Z | 25 | 26 | 27 | 29 | 30 | | | | |
| Category 3 | M | ***I*** | Xe | ***Gd*** | | | | | | |
| | Z | 53 | 54 | 64 | | | | | | |
| Category 4 | M | ***water*** | ***PMMA*** | bone | | | | | | |
| | Z | | mixture | | | | | | | |

the following. The decomposition results of five existing materials are shown in figure 3.4. All of the three methods has worse decomposition performance compared to the condition that only 5 basis materials exists in the decomposition matrix. Even though, our proposed DSR method shows better accuracy for gadolinium and some better detection ability of iron and iodine. For the other materials, we use the mean absolute error (MAE $= \frac{\sum_{i=1}^{N} |theoritical\ value - pratical\ value|_i}{N}$) to quantify the accuracy. The MAEs of the other basis materials are plotted in N logarithmic coordinates, as shown in figure 3.5. Compared to L1, DSR method has smaller MAE for most materials in Table 3.1.

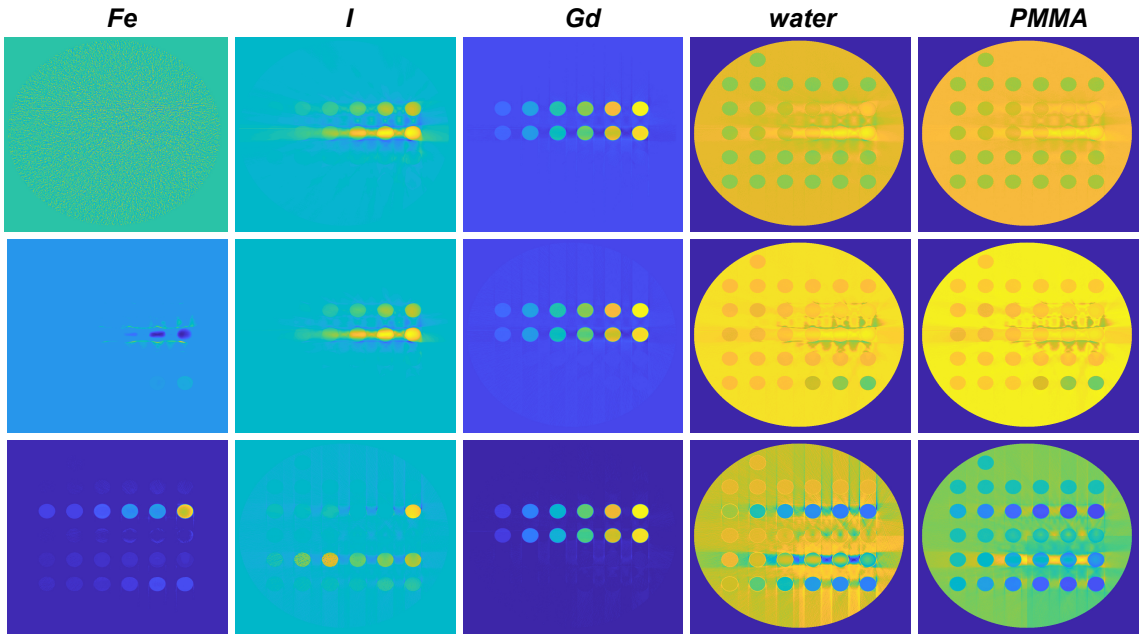


Figure 3.4: The results of material decomposition based on reconstructed sTC images without Poisson noise for the three methods: 5 energy bins, 20 basis materials. Top to bottom: Pseudo-inverse with SVD, L1 and DSR.

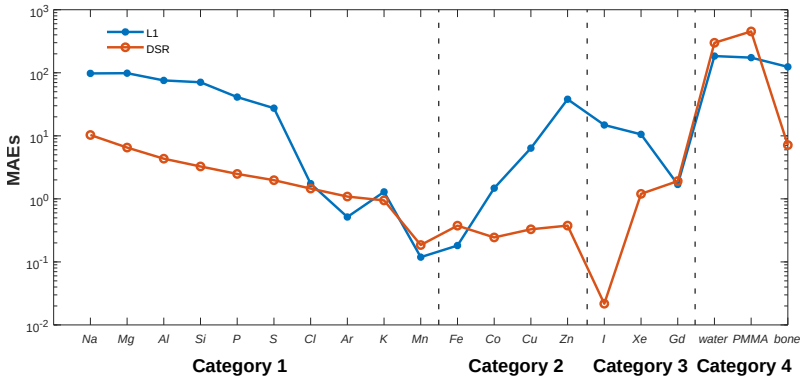


Figure 3.5: The MAEs of materials in Table 3.1.

### Effects of low-energy bins

To evaluate the impacts of bins with lower energy, decomposition performance in terms of different number of energy bins, we add the 6-th energy bin: 20-30 keV. The decomposition results of five existing basis materials are shown in figure 3.6. Visually, there is no obvious difference with 5 bins for the methods SVD and L1. For the proposed DSR method, decomposition result of iron and gadolinium has more cross-contamination with water and PMMA. To further quantitatively evaluate the impacts of the 6-th bin, we compare the mass density of Fe, I and Gd in the corresponding rows. For iodine, the results of DSR method is overestimated for all the concentrations, while for iron and gadolinium underestimated. The results indicate that with the 6-bin, DSR method has worse stability in terms of the decomposition results of 5-bins were always underestimated for all the three materials (as shown in figure 3.3).

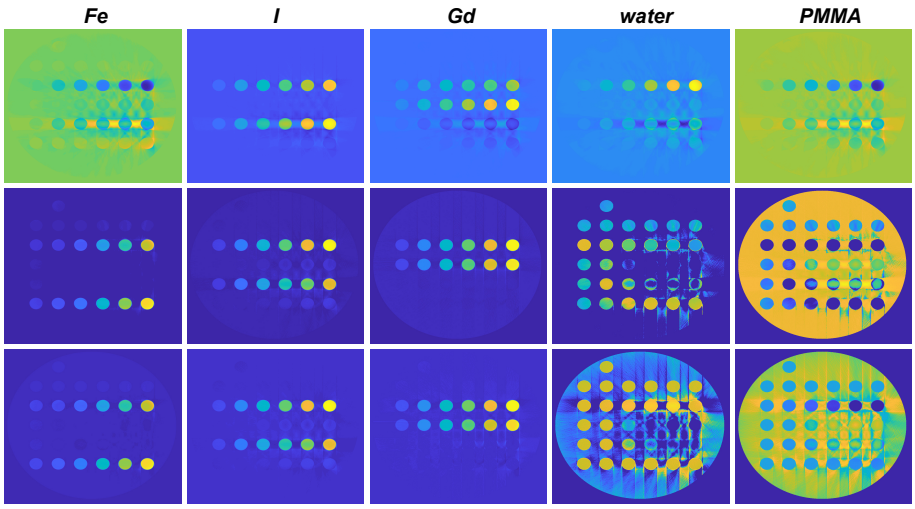


Figure 3.6: The results of material decomposition based on reconstructed sTC images without Poisson noise for the three methods: 6 energy bins, 5 basis materials. Top to bottom: Pseudo-inverse with SVD, L1 and DSR.

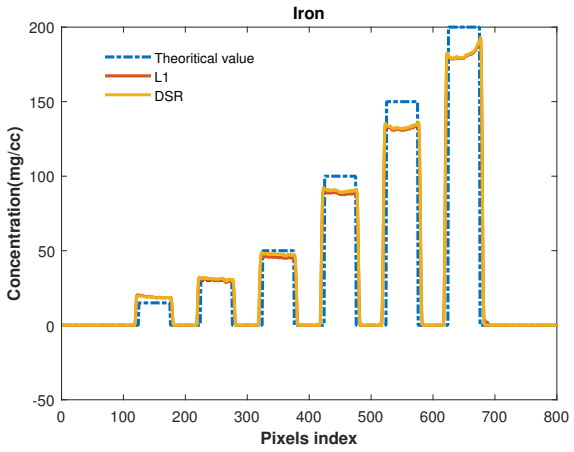


(a)

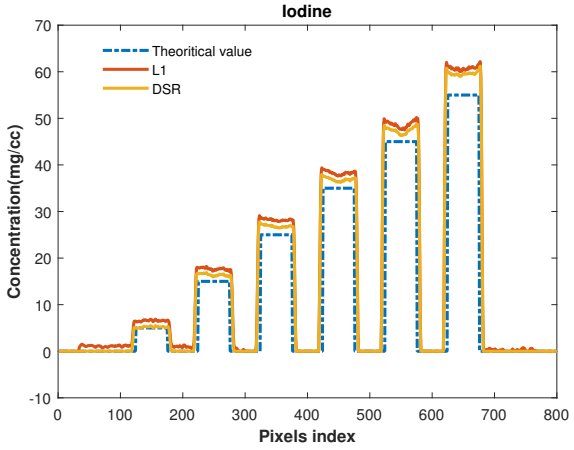


(b)

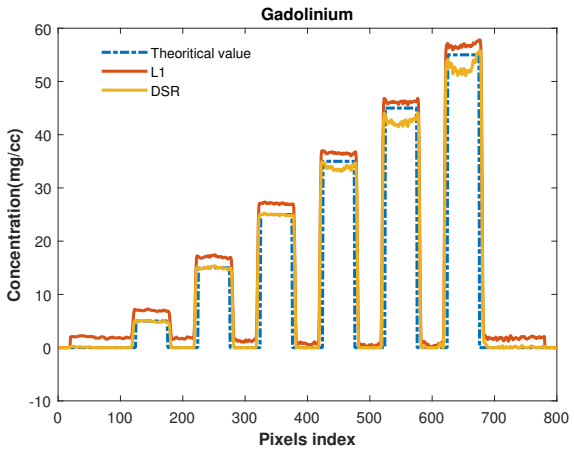


(c)

Figure 3.7: The mass densities of iron, iodine and gadolinium: 6 energy bins.

**With Poisson noise**

The decomposition results of five existing basis materials with Poisson noise are shown in figure 3.8. Even for the material without k-edge (Fe), DSR shows good ability in detection and quantification, which is similar to the results without Poisson noise. Visually, there are obviously more errors for water-like materials than for iron, iodine and gadolinium. Fortunately in practical applications, the quantitative information of the last three materials are more useful, as a result of which we will pay more attention to the materials of interest: iron, iodine and gadolinium. As an illustration, we list $error_m$ of iron, iodine and gadolinium for the three methods in Table 3.2. Clearly, DSR method has smaller $error_m$ for all the three materials compared to L1 method.

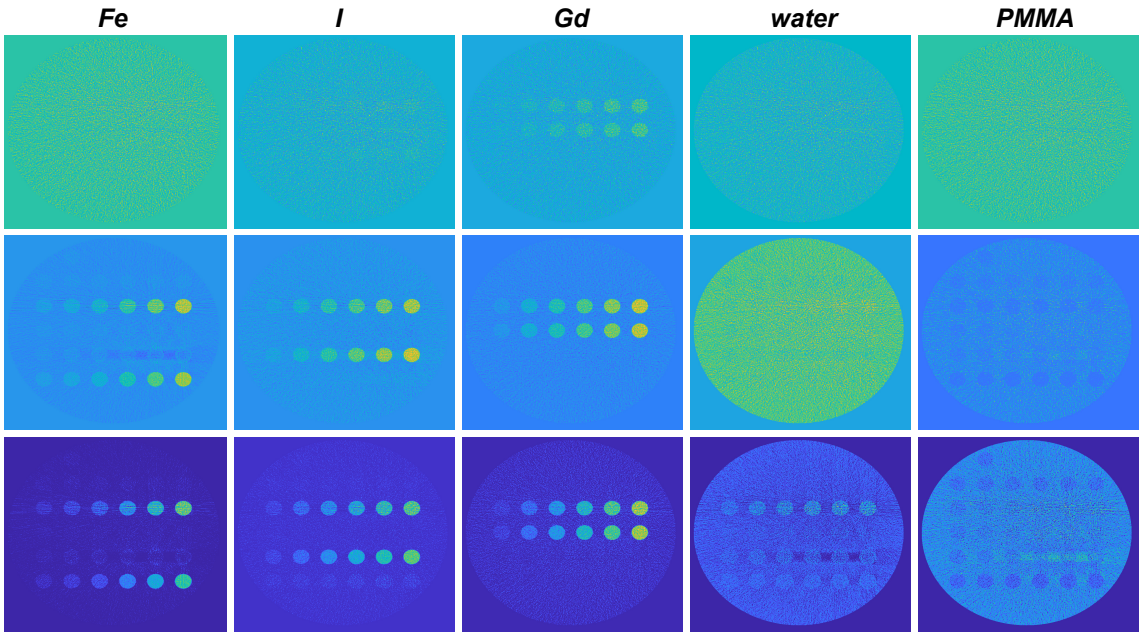


Figure 3.8: The results of material decomposition based on reconstructed sTC images with Poisson noise using the three methods: 5 energy bins, 5 basis materials. Top to bottom: Pseudo-inverse with SVD, L1 and DSR.

Table 3.2: The normalized Euclidean distance $error_m$ of different decomposition methods on digital phantom.

| Materials \ Methods | SVD | L1 | DSR |
|---|---|---|---|
| Iron | 49.03 | 0.23 | 0.16 |
| Iodine | 1.91 | 0.37 | 0.18 |
| Gadolinium | 0.36 | 0.31 | 0.30 |

### 3.4.2 Physical data

The physical phantom was acquired on a Phillips sCT prototype [Si-Mohamed et al., 2018, Cormode et al., 2017]. The scan consists of 2400 projections; each projection has 643 parallel rays; each ray contains 5 energy bins: 30-50 kev, 51-61 kev, 62-71 kev, 72-82 kev and 83-130 kev. The incident photons $n_0(E)$ and detector bin response function $d_i(E)$ were provided by the manufacturer of the sCT prototype. The physical phantom is shown in Fig. 3.9a. The annotation is the same as for digital phantom. We reconstructed the spatial image at each energy bin via SART-TV, and the reconstructed image of the first bin is shown in Fig. 3.9b, where ring artifacts are obvious. The image reconstructed at each bin has a size of 380*380.

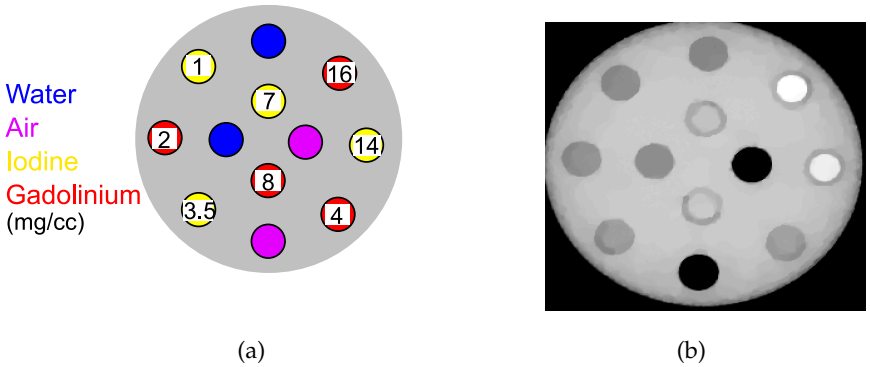


(a) (b)

Figure 3.9: (a) Physical phantom; (b) the reconstructed image of physical phantom at the first energy bin.

Meanwhile, we have another in vivo data to further evaluate the proposed method. Reconstructed images of a rabbit 15 min after injection of gadolinium are shown in Fig. 3.10. Note that calcium (Ca) in the spine is decomposed on the basis material iodine, due to their similarity of mass attenuation coefficients in our energy thresholds setting. For gadolinium, although the ground-truth is unknown in the in vivo data, tubes of gadolinium dilutions nearby the rabbit were evaluated alternatively.

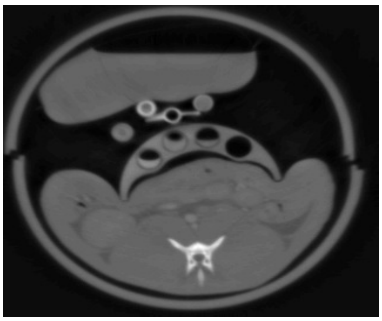

Figure 3.10: The reconstructed image of in vivo data at the first energy bin 15 min after the injection of gadolinium.

Table 3.3: The normalized Euclidean distances $error_m$ of different decomposition methods on physical phantom.

| Materials \ Methods | SVD | L1 (positive) | DSR |
|---|---|---|---|
| Iodine | 1.96 | 0.46 | 0.36 |
| Gadolinium | 1.03 | 0.98 | 0.21 |

The results of material decomposition on the physical phantom are shown in Fig. 3.11. In terms of the worse ability of separating water and PMMA and less interests of them in clinical applications, we only considered three basis materials, water, iodine and gadolinium, in the physical phantom. The proposed DSR material decomposition method has clearly better performance in detection and quantification compared to SVD and L1 methods. Firstly, our method shows much better morphological accuracy, especially for gadolinium which are obviously overwhelmed for both SVD and L1 methods but are more accurate for DSR method. Secondly, more quantitatively as shown in Table 3.3, DSR method has clearly smaller normalized Euclidean distance. Specially, gadolinium exhibits higher accuracy compared to iodine with DSR method.

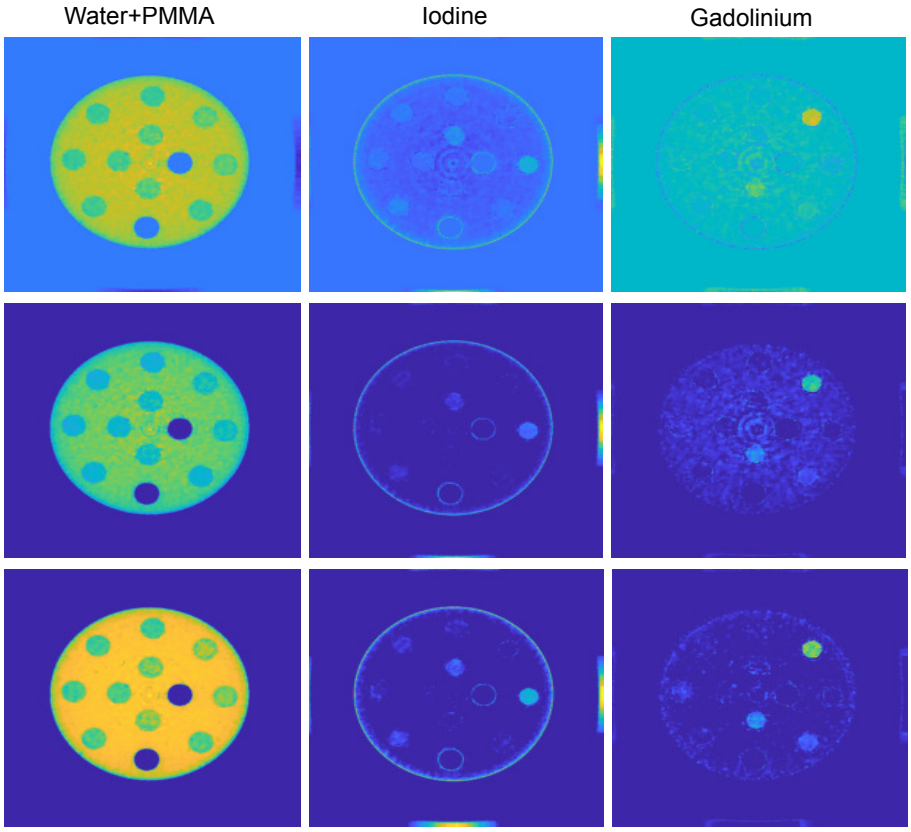


Figure 3.11: The results of material decomposition based on physical phantom. Top to bottom: Pseudo-inverse with SVD, L1 and DSR.

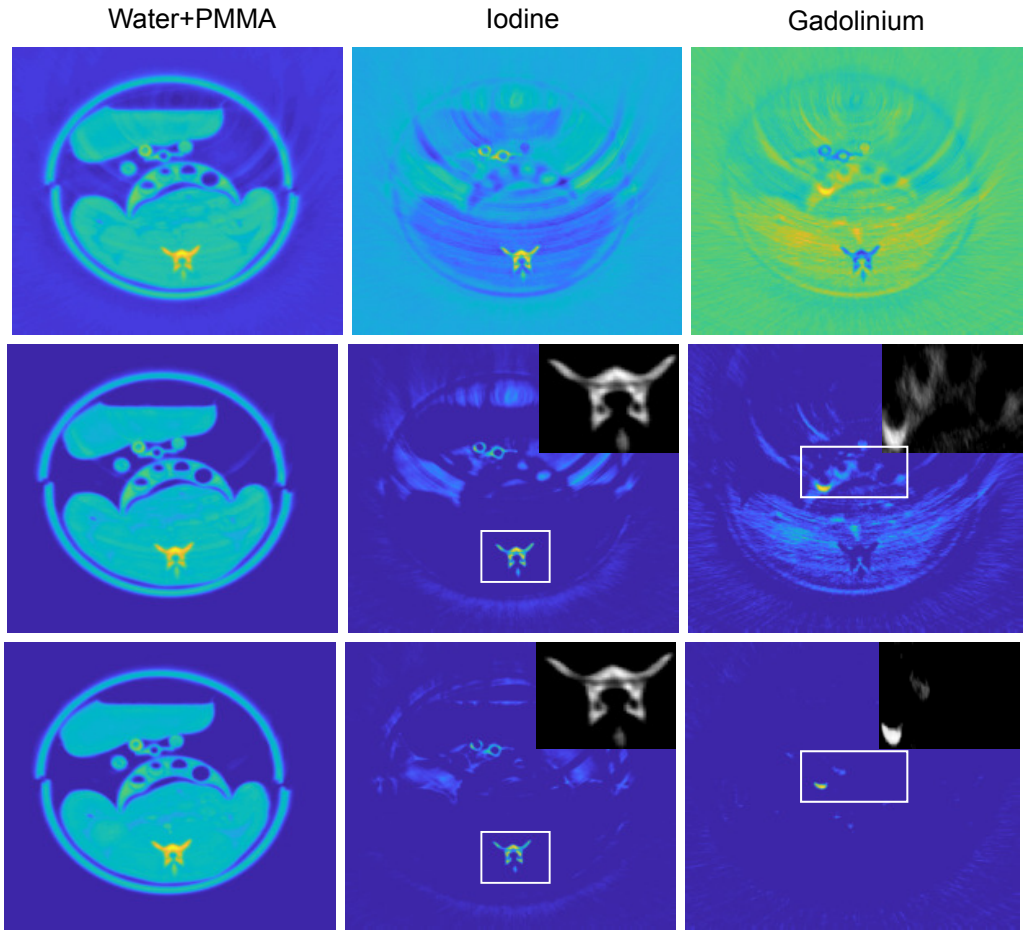


Figure 3.12: The results of material decomposition based on in vivo data. Top to bottom: Pseudo-inverse with SVD, L1 and DSR.

For in vivo data, the decomposition results of different methods are shown in Fig. 3.12. Obviously, both SVD and L1 method have worse detection ability for both iodine and gadolinium. On the contrary, the proposed DSR method has higher accuracy for both iodine and gadolinium. It should be noted that all the three methods cannot detect gadolinium of 2 mg/cc in the in-vivo data, which may ne resulted from the precision of effective decomposition matrix $\boldsymbol{M}$.

## 3.5 Discussion and conclusions

We have proposed a material decomposition method for spectral CT by simultaneously exploiting the limited value of mass density, the multi-dimensional nature and high correlation of multi-energy data and the local property of neighboring pixels. To get rid of the difficulties due to similarities among basis materials, spectral and spatial redundancies are eliminated through using joint sparsity and structural low-rank. At the same time, we also add bound constraint on mass density, which is naturally true in practi-

cal applications. Preliminary results revealed that the proposed DSR method has a good material decomposition ability even for very poorly conditioned problems.

The performance of material decomposition is influenced simultaneously by multiple effects, such as quantum noise, the number of energy bins and the set of basis materials. Actually, sCT material decomposition suffers from strong quantum noise at each single bin stemming from narrow bin-width. As shown in figure 3.2 (without Poisson noise) and figure 3.8 (with Poisson noise), the Poisson noise obviously degrades the decomposition performance. Theoretically, more bins can bring more spectral information. However, sCT material decomposition suffers from strong quantum noise at each single bin stemming from narrow bin-width. In other words, the energy resolution of sCT is limited by a trade-off between the total number of energy bins and the image quality at each bin. As a result, in practice, the number of energy bins of sCT is always constrained, *e.g.* 5 bins for Phillips sCT prototype (the setting in our experiments) [Si-Mohamed et al., 2018, Cormode et al., 2017]. Meanwhile, the bins of too lower energy can further worsen the decomposition. As shown in figure 3.7, material decomposition using 6 bins, with the additional bin of 20-30 kev, has more errors for all the three methods. For the set of basis materials, the decomposition is dramatically degraded by large number of basis materials, especially by the materials with similar mass attenuation coefficients more basis materials, as shown in figure 3.4. Nevertheless, even in this condition, the proposed DSR method still has better performance, as illustrated in figure 3.5.

The regularization in the proposed DSR method is a convex problem. We have used an iterative algorithm ADMM to solve the proposed model. To accelerate convergence, the initialization of variables in the ADMM was set as the results of pseudo-inverse with SVD. Although there are four regularizations in the cost function, only the joint sparsity term and the structural low-rank term have the regularization parameters $\lambda_1$ and $\lambda_2$. The results of material decomposition are clearly influenced by the regularization parameters. This is in fact a persistent problem, since solving cost function with more than one regularization parameter is still a challenging problem [Clark and Badea, 2014, Gao et al., 2011, Zhang et al., 2016, Ding et al., 2018]. The scalar regularization parameters $\lambda_1$ and $\lambda_2$ influence respectively the level of sparsity and low-rank. The augmented Lagrangian parameter $\tau$ that is equal to the step size of iteration has also an obvious impact on convergence speed. In practice, to make performance less dependent on the initial choice, we have updated $\tau$ in each iteration by the way discussed in [Boyd et al., 2010, WANG and LIAO, 2001](try to keep the primal and dual residual norms in the ADMM within a factor as they both converge to zero). Finally, due to the use of local property, the choice of regularization parameters $\lambda_1$, $\lambda_2$ and $\tau$ is also influenced by the size of patch. Generally, a smaller size of patch should have the correspondingly smaller regularization parameters, otherwise obvious errors will occur near the edges of patches in the decomposed material images. Note that neither too large patches nor too small patches accords with the local property or result in an accurate decomposition, and it should be set according to the property of each spectral CT data.

In conclusion, the proposed DSR method exhibits good performance in simultaneously separating and quantifying two contrast agents, e.g. iodine and gadolinium. In particular, the good ability of DSR to distinguish the contrast agents (*e.g.* iodine, gadolinium and xenon) suggests its interesting potential use for industrial and medical applications. In the future work, the collaborative joint sparsity and structural low-rank should

be further investigated to make full use of the sparsity and low-rank property hidden in the spectral CT data. Finally, a more robust strategy for the choice of regularization parameters could also be investigated.

# Chapter 4

# ROI-Wise Material Decomposition in Spectral Photon-Counting CT

## Contents

## 4.1 Introduction

SCT is a new kind of multi-energy X-ray CT that offers new possibilities for getting insights into material components in an object, thanks to the advances in photon-counting detector (PCD). Compared to conventional energy-integrating CT or dual energy CT, sCT can count the number of photons in multiple energy bins with one single exposure, *i.e*. utilizing spectral information. This advantage enables efficient material decomposition that aims to quantitatively separate different materials (at least three) present in a pixel.

However, the reliability and accuracy of the decomposition approaches (which were discussed in Chapter 2 and 3) are always impacted by unavoidable similarity between linear attenuation coefficients of basis materials [Si-Mohamed et al., 2018, Si-Mohamed et al., 2017a] (more details were discussed in Chapter 2). Such similarity makes it difficult to separate the basis materials. The difficult basis material separation is further worsened by strong quantum noise. The latter also limits the ability of PCD to recognize photons between adjacent energy bins [Schlomka et al., 2008], which renders the basis material separation still more difficult. Meanwhile, the performance of image-domain material decomposition is also susceptible to the quality of reconstructed sCT images including in particular the impact of beam hardening.

To improve the reliability and accuracy of material decomposition, it is important to make full use of more information beside the aforementioned spectral information [Zhang et al., 2016, Li et al., 2017, Zhang et al., 2017, Fadili et al., 2010, Xia et al., 2019]. A straightforward way of realizing this is to exploit morphological information embedded in the reconstructed sCT images. Image-domain material decomposition is then an approach of choice. In this chapter, we investigate a novel image-domain material decomposition method by directly decreasing the impacts of similarity between basis materials with the help of multiple features extracted from the reconstructed multi-energy spatial sCT images. The idea is to exploit the abundant information and high correlations in sCT images suffering from serious reconstruction errors and artifacts. To do that, we perform basis material optimization by selecting basis materials according to their spatio-energy similarity in segmented region of interests (ROIs) of multi-energy sCT images, thus leading to so-called ROI-wise material decomposition. To our knowledge, this is the first work to improve the mathematical condition of material decomposition through optimizing basis materials by means of spatio-energy segmentation.

The rest of this chapter is organized as follows. In Section 4.2, we describe the proposed method of ROI-wise material decomposition. Section 4.3 presents experiments and results on both simulations and real data. Finally, Sections 4.4 is given discussion and conclusion.

## 4.2 ROI-wise material decomposition

To make material decomposition more reliable and accurate, we propose to fully exploit their spatio-energy similarity in ROIs of multi-energy sCT images and inter-bin uncorrelation and material-dependent characteristics of noise in sCT images. To do that, we perform a basis material optimization through reducing the impact of material similarity by means of spatio-energy segmentation. Meanwhile, we construct a noise-reduced

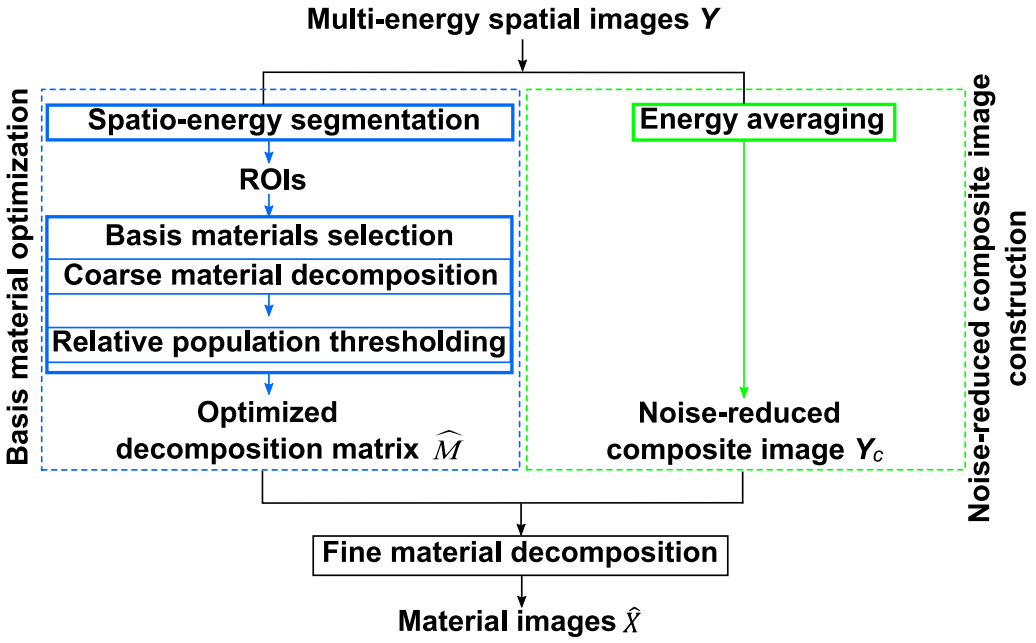


Figure 4.1: Diagram of the ROI-wise material decomposition algorithm. Top to bottom: the spatio-energy segmentation based basis material optimization (blue) and noise-reduced composite image construction (green), and the fine material decomposition.

composite image by introducing a so-called energy averaging [Leng et al., 2011], in which images at different energy bins are mixed but noise is reduced. Another characteristic of noise in sCT is that it is material-dependent, meaning that noise shows different impacts on materials according to their categories and mass densities, *e.g.* water-like materials (water, Poly(methyl methacrylate) (PMMA) and soft issue, *etc.*) with smaller mass attenuation coefficients and materials with lower densities are much easier to be influenced by noise compared to the dense materials of interest. It was reported in [Ducros et al., 2017, Si-Mohamed et al., 2018] that dilutions of contrast agents (*e.g.* iodine, gadolinium and gold, *etc.*) with lower concentrations have smaller contrast to noise ratio. The resulting noise-reduced composite image is then utilized in a material-wise way in the fine material decomposition. The global diagram of the proposed ROI-wise material decomposition is illustrated in figure 4.1.

Basis material optimization is first processed based on the spatio-energy segmentation that separates multi-energy spatial images into different ROIs. Next, the basis materials in $\boldsymbol{M}$ are selected by performing a coarse material decomposition followed by a relative population thresholding. The part of basis material optimization is boxed in blue in figure 4.1 and more details will be discussed in Section 4.2.1.

The noise-reduced composite image is constructed by averaging, in the direction of energy, multiple spatial images corresponding to different energy bins (the green part in figure 4.1 and details presented in Section 4.2.2).

The basis material optimization result and the noise-reduced composite image are finally fed in the fine material decomposition block to obtain the final material images.

### 4.2.1 Basis material optimization

As the core of our ROI-wise material decomposition, basis material optimization comprises two steps: spatio-energy segmentation and basis material selection. The first step aims to separate the reconstructed spatial images into different ROIs. The second one deletes irrelevant basis materials using a coarse material decomposition and a relative population thresholding.

We first obtain the ROIs of multi-energy images by spatio-energy segmentation, where each ROI represents a homogeneous area containing similar materials. To achieve such spatio-energy segmentation, morphological and spectral features of multi-energy images are used. figure 4.2 illustrates the segmentation of two ROIs in the multi-energy spatial images. Spectral features are extracted by regrouping the sCT images at all the energies as a single three-dimensional (3-D) image in which the energy is taken as a third dimension. Each pixel in the 3-D image has multi-energy values (energy-dependent $\mu$). Pixels having different $\mu$ curves, *i.e.* different spectral features, belong to different ROIs, as shown in the upper-middle part of figure 4.2. Morphological features of sCT images are in fact energy-dependent because the characteristics of materials in sCT images are energy-dependent. As a result, structures imperceptible at certain energy bins may be distinguished more easily at another bin, depending on the physical characteristics of materials. Therefore, we take the morphological features from the energy bin having the most reliable segmentation by evaluating a pre-processing segmentation based on Gaussian mixture model (GMM) at each single energy bin. Then, the extracted structures are treated as the common constraint for images at all energy bins, as shown in the lower-middle part of figure 4.2, where $\boldsymbol{Y}_s$ denotes the multi-dimensional image containing common structures. The spectral and morphological features are then exploited jointly for segmentation based on clustering.

In details, we use the kernel k-means method for the fusion of spectral and morphological features. The main advantage of kernel k-means is that it can make full use of kernel properties, which provides the ability to combine different features [Dhillon et al., 2004, Fauvel et al., 2012]. More precisely, we utilize the kernel k-means method to automatically segment the pixels in the 3-D image:

$$\mathcal{D}(\{\pi_k\}_{k=1}^K) = \sum_{k=1}^{K} \sum_{\boldsymbol{y}\in\pi_k} \|\Phi(\boldsymbol{y}) - \boldsymbol{m}_k\|_2^2, \quad s.t.\ \boldsymbol{m}_k = \frac{\Phi(\boldsymbol{y})}{\|\pi_k\|_1}, \tag{4.1}$$

where $\Phi$ represents a non-linear transform function, $\{\pi_k\}_{k=1}^K$ the partitioning of multi-energy pixel values $\boldsymbol{y} \in \mathcal{R}^B$ into different clusters $\pi_k$, $K$ the total number of clusters (*i.e.* the total number of ROIs and is initialized by the total number of basis materials ($M$)), $\boldsymbol{m}_k$ the ideal cluster values, and $\|\cdot\|_2$ and $\|\cdot\|_1$ denote L-2 and L-1 norm, respectively. As an enhanced algorithm of normal k-means, kernel k-means can separate vectors in a high-dimensional feature space based on the non-linear transform. The non-linear transform can be calculated with a convenient kernel, and new kernel can be constructed by linearly adding two basic kernels, denoted by $\boldsymbol{\mathcal{K}}_1$ and $\boldsymbol{\mathcal{K}}_2$ respectively, *i.e.* $\theta_1\boldsymbol{\mathcal{K}}_1 + \theta_2\boldsymbol{\mathcal{K}}_2$, which is still a kernel. We utilize this property to combine spectral and spatial features which are separately selected by two kernels, named as $\boldsymbol{\mathcal{K}}^{spectrum}$, $\boldsymbol{\mathcal{K}}^{space}$. The new kernel is then

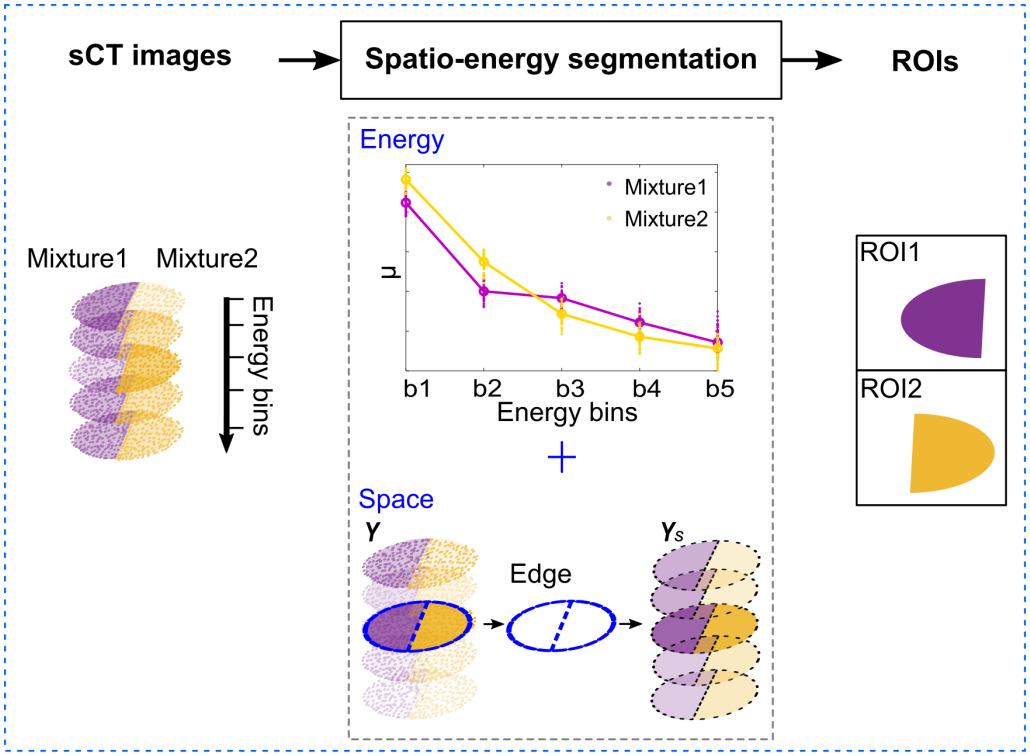


Figure 4.2: Diagram of the spatio-energy segmentation. Left to right: multi-energy spatial images containing mixture 1 and mixture 2, the spatio-energy segmentation using spectral (upper-middle) and spatial (lower-middle) features, and segmented ROIs.

obtained:

$$\mathcal{K}_{\sigma,\lambda} = \theta \mathcal{K}_{\sigma}^{spectrum} + (1-\theta)\mathcal{K}_{\sigma}^{space}, \tag{4.2}$$

where $0 \leq \theta \leq 1$ and $1-\theta$ designate the weights for spectral and spatial kernels, respectively. $\theta$ controls the relative impacts of spectral and spatial features on the final kernel.

The kernel for spectral features is a Gaussian radial basis kernel:

$$(\mathcal{K}_{\sigma}^{spectrum})_{ij} = \kappa_{\delta}(\boldsymbol{y}_i, \boldsymbol{y}_j) = \exp(-\frac{\|\boldsymbol{y}_i - \boldsymbol{y}_j\|_2^2}{2\sigma^2}), \tag{4.3}$$

where $\kappa$ denotes the Gaussian radial basis kernel and $\sigma$ the variance of the corresponding Gaussian distribution.

The kernel for spatial features is also a Gaussian radial basis kernel:

$$(\mathcal{K}_{\sigma}^{space})_{ij} = \kappa_{\delta}(\boldsymbol{y}_{si}, \boldsymbol{y}_{sj}) = \exp(-\frac{\|\boldsymbol{y}_{si} - \boldsymbol{y}_{sj}\|_2^2}{2\sigma^2}). \tag{4.4}$$

However, the pixel values $\boldsymbol{y}_{si} \in \mathcal{R}^B$ calculated in $\mathcal{K}_{\sigma}^{space}$ are those of the pre-processed 3-D image $\boldsymbol{Y}_s$ containing the 'labels' of morphological information. The pre-processing aims to detect spatial features from the image having the most reliable morphological information. We assume that all the data points are generated from a mixture of a limited number

of Gaussian distributions. Although materials have very different attenuation properties at different bins, the pixel values at each bin still obey the Gaussian distribution, of which the parameters and weights are different at different bins. More precisely, we firstly divide pixels in each spatial image by a classical classification method involving GMM, which is a probabilistic model that assumes that all the data points are generated from a mixture of a limited number of Gaussian distributions:

$$p_M(y^b) = \sum_{i=1}^{K} \alpha_i p(y^b | m_i^G, \sigma_i), \tag{4.5}$$

where $p(y^b|m_k^G,\sigma_i)$ represents the $i$-th Gaussian distribution with means $m_i^G$ and covariance $\sigma_i$, $\alpha_i$ the corresponding weights, $K$ the total number of components, and $y^b$ the $b$-th bin value of pixel $\boldsymbol{y}$ in the 3-D image. The models are known a priori; they are Gaussian. But, their parameters and mixture weights are unknown. The unknown parameters (mean $m^G$, covariance $\sigma$) in Gaussian models as well as the weights $\alpha$ were automatically estimated via the expectation maximization (EM) algorithm [McLachlan and Krishnan, 2008]. Meanwhile, the parameters are calculated independently at different bins.

Then, the spatial image at each energy bin is segmented into $K$ areas by classification. In our case the probability density function $p_M(y^b)$ of GMM is used to estimate the reliability of segmentation results. More precisely, the reliability of segmentation is evaluated by the optimal value of the loglikelihood cost function:

$$LL(\boldsymbol{Y}^b) = \ln\left(\prod_{i=1}^{N_P} p_M(y_i^b)\right), \tag{4.6}$$

where $N_P$ denotes the total number of pixels in the two-dimensional (2-D) image at each bin. The segmentation at certain energy bin with larger loglikelihood value is believed to be more reliable, and then the detected edges in the image at that energy bin are taken as the common edges for all the spatial images at different bins. Note that the images at different bins should be normalized (pixel value/maximum value at that bin) before comparing loglikelihood values. After that, the mean value of pixels inside each segmented area at each bin is calculated:

$$\bar{y}_{\{\pi_k\}}^b = \frac{1}{N_k} \sum_{i=1}^{N_k} y_i^b, \quad s.t. \quad y_i^b \in \{\pi_k\}, \tag{4.7}$$

where $y_i^b \in \{\pi_k\}$ represents the $i$-th pixel value in the $k$-th segmented area at the $b$-th bin, and $N_k$ the total number of pixels insider the $k$-th area. Then, a new 3-D image $\boldsymbol{Y}_s$ (the subscript 's' refers to 'spatio') is produced by assigning its pixel value the corresponding mean value $\bar{y}_{\{\pi_k\}}^b$:

$$y_{si}^b = \bar{y}_{\{\pi_k\}}^b, \quad s.t. \quad y_{si}^b \in \{\pi_k\}, \tag{4.8}$$

where $y_{si}^b \in \{\pi_k\}$ represents the $i$-th pixel value of $\boldsymbol{Y}_s$ in the $k$-th segmented area at the $b$-th bin. In other words, a 'label' is attributed to each pixel associated with its spatial features. Therefore, each multi-dimensional pixel is now assigned to two different values: the original value ($\boldsymbol{y}$) containing spectral feature and the mean value ($\boldsymbol{y}_s$) containing

morphological feature, of which the features can be extracted by different kernels and fused together by our final kernel in equation (4.2).

We have in total three k-means clustering procedures in the spatio-energy segmentation. Both spectral and morphological features are learned using clustering methods. Specifically, the spectral features are learned based on the vector classification (*i.e.* to classify vectors containing energy information), while the morphological features are learned based on the classification of mixture of Gaussian distributions (from the bin with the highest likelihood). Obviously, the two clustering procedures utilize different features. Finally, the morphological and spectral features are combined together using kernel k-means. As illustrated in figure 4.3, there are three clusterings in the second step of basis material optimization: clustering of spectral features (vector clustering), clustering of spatial features at each bin for the calculation of the highest likelihood, and clustering based on both spectral and spatial kernels. The spectral features are learned from vector information, while the spatial features utilize bin-by-bin information.

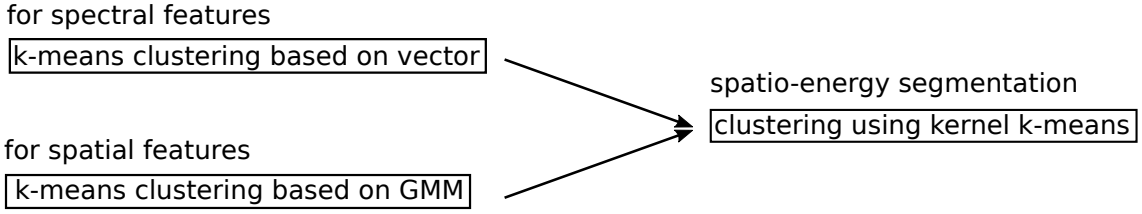


Figure 4.3: Sketch of spatio-energy segmentation.

The second step of basis material optimization is to update the initialized decomposition matrix under the principle of keeping the minimum needed number of basis materials (with respect to ground-truth) while excluding as many as possible. To do this, we introduce a coarse material decomposition in each ROI, which exploits the sparse nature by L-1 norm (*lasso* [Tibshirani, 1996]):

$$\underset{X}{\operatorname{argmin}} \frac{1}{2}\|\boldsymbol{Y} - \boldsymbol{M}\boldsymbol{X}\|_F^2 + \lambda\|\boldsymbol{X}\|_1, \tag{4.9}$$

where $\frac{1}{2}\|\boldsymbol{Y} - \boldsymbol{M}\boldsymbol{X}\|_F^2$ is the data fidelity term calculated in terms of Frobenius Norm $\|\cdot\|_F$ and $\lambda$ the Lagrange multiplier. The coarse material decomposition method is subject to obvious unreliability of detecting materials and poor accuracy [Xie et al., 2019]. It can nevertheless help indicate us which basis materials should be considered nonexistent, while the others are more plausible under certain selection criterion. Therefore, we propose a relative population thresholding (RPT) method to determine which basis material deserves to be selected. The RPT method is based on the population percentage defined as the ratio of the number of pixels containing certain decomposed material $N_x$ to the total number of pixels $N_{ROI}$ in each ROI (*i.e.* one pixel 'contains' a material means the decomposed mass density of this material is a positive number at the pixel); only the materials with percentage above a threshold will be preserved in each ROI. The physical meaning of RPT is partly involved with the aforementioned local property in both spectral and morphological domains. Local property limits the distribution of basis materials, which means that a corresponding minimum population percentage for all the

ROIs should exist. In other words, the threshold of population percentage is associated with the aggregation degree of materials. After basis material optimization, we obtain a new $\hat{\boldsymbol{M}}$ from $\boldsymbol{M}$ in the $k$-th ROI, as:

$$\begin{aligned} &\hat{\boldsymbol{M}}_k \leftarrow (\boldsymbol{M})_\alpha, \\ &if\ \frac{N_{x\alpha k}}{N_{ROIk}} \geq T \quad s.t.\ \underset{\boldsymbol{X}_k}{\operatorname{argmin}} \frac{1}{2}\|\boldsymbol{Y}_k - \boldsymbol{M}\boldsymbol{X}_k\|_F^2 + \lambda\|\boldsymbol{X}_k\|_1, \end{aligned} \tag{4.10}$$

where $\hat{\boldsymbol{M}}_k \in \mathcal{R}^{B\times M'}$ denotes the optimized decomposition matrix containing $M'$ entries in the $k$-th ROI, $(\boldsymbol{M})_\alpha$ the $\alpha$-th basis material in decomposition matrix $\boldsymbol{M}$, $\leftarrow$ the operator of assigning certain material from $\boldsymbol{M}$ to $\hat{\boldsymbol{M}}$, $N_{x\alpha k}$ the number of pixels containing the $\alpha$-th basis material in the $k$-th ROI, $T$ the population threshold, and $\boldsymbol{Y}_k$ and $\boldsymbol{X}_k$ the multi-energy spatial images and coarsely decomposed materials in the corresponding ROI, respectively.

### 4.2.2 Noise-reduced composite image construction

Noises at different energy bins are independent when the charge sharing effect of PCD can be ignored. Thus, by averaging multi-energy spatial images in the dimension of energy, we obtain a composite image where noise is reduced and information is mixed:

$$\boldsymbol{Y}_c = \frac{1}{B}\sum_{b=1}^{B} \boldsymbol{Y}^b, \tag{4.11}$$

where $\boldsymbol{Y}^b$ denotes the spatial image at the $b$-th energy bin.

### 4.2.3 Fine material decomposition

Fine material decomposition is the last step in the proposed ROI-wise material decomposition method, which involves three terms: data fidelity term based on the optimized decomposition matrix $\hat{\boldsymbol{M}}$, denoising regularization term involving the noise-reduced composite image $\boldsymbol{Y}_c$, and sparsity regularization term.

Especially, the denoising regularization term is devoted to exploiting the inter-bin uncorrelation and material-dependent characteristics of noise in sCT images owning to the presence of $\boldsymbol{Y}_c$. To prevent water-like materials (*e.g.* water, PMMA and soft tissue, *etc.*) from degrading materials of interest (*e.g.* contrast agents), we propose to utilize the noise-reduced composite image $\boldsymbol{Y}_c$ in a material-wise way. More precisely, we introduce a weight vector $\boldsymbol{w} \in \mathcal{R}^{1\times M'}$ associated with relative mass attenuation coefficients $w_\alpha$,

$$\boldsymbol{w} = [w_\alpha \bar{\mu}_{m\alpha}], \tag{4.12}$$

where $\bar{\mu}_{m\alpha}$ is the mean value of effective mass attenuation coefficients of the $\alpha$-th basis material for all the energy bins, $\bar{\mu}_{m\alpha} = \frac{1}{B}\sum_{b=1}^{B} \dot{\mu}_{m\alpha}(b)$, and $w_\alpha = \bar{\mu}_{m\alpha}/\bar{\mu}_{mB}$ with $\bar{\mu}_{mB}$ designating the mean value of effective mass attenuation coefficients of water-like material. Actually, $\boldsymbol{w}$ highlights the importance of materials of interest by decreasing the disturbance from water-like materials, *i.e.* in a material-wise way. Hence, the denoising regularization term involving composite spatial image can be formulated as $\|\boldsymbol{Y}_c - \boldsymbol{w}\boldsymbol{X}\|_{TV}^2$, where $\|\cdot\|_{TV}$ represents TV-norm.

Mathematically, we formulate the fine material decomposition as:

$$\begin{aligned}&\underset{\boldsymbol{X}}{\operatorname{argmin}} \sum_k \frac{1}{2}\|\boldsymbol{Y}_k - \hat{\boldsymbol{M}}_k \boldsymbol{X}_k\|_F^2 + \lambda_1 \|\boldsymbol{X}_k\|_1 + \lambda_2 \|\boldsymbol{Y}_{ck} - \boldsymbol{w}\boldsymbol{X}_k\|_{TV}^2 \\ &= \underset{\boldsymbol{X}}{\operatorname{argmin}} \frac{1}{2}\|\boldsymbol{Y} - \hat{\boldsymbol{M}}\boldsymbol{X}\|_F^2 + \lambda_1 \|\boldsymbol{X}\|_1 + \lambda_2 \|\boldsymbol{Y}_c - \boldsymbol{w}\boldsymbol{X}\|_{TV}^2. \end{aligned} \tag{4.13}$$

where $\|\boldsymbol{Y} - \hat{\boldsymbol{M}}\boldsymbol{X}\|_F^2$ denotes the data fidelity term, $\|\boldsymbol{X}\|_1$ the sparsity regularization term, and $\|\boldsymbol{Y}_c - \boldsymbol{w}\boldsymbol{X}\|_{TV}^2$ the denoising regularization term. The above fine material decomposition model is solved via the alternating direction method of multipliers (ADMM) iteration method [Boyd et al., 2010, Jiao et al., 2016].

## 4.3 Experiments and results

The performance of the proposed ROI-wise material decomposition method was evaluated on both digital and physical phantom data.

#### Image quality metrics

The performance of the proposed material decomposition was quantitatively evaluated using different metrics. The normalized Euclidean distance that utilized in Chapter 3 was also utilized for accuracy. Meanwhile, to emphasize the reliability of proposed method, we introduce two new criteria: the false positive (FP) and false negative (FN). The FP or FN rate is calculated as the ratio of the number of wrongly recognized pixels $N_{FP}$ (*i.e.* for materials inexistent in ground-truth but in decomposition results) or unrecognized $N_{FN}$ (*i.e.* for materials existent in ground-truth but not decomposed in results) to the total number of pixels in all the ROIs $N_{ROIs}$:

$$FP = \frac{N_{FP}}{N_{ROIs}}; \quad FN = \frac{N_{FN}}{N_{ROIs}}. \tag{4.14}$$

For sCT material decomposition, a smaller FP rate means smaller errors of confusing different materials, while a larger FN occurs when existing materials cannot be recognized. In other words, the smaller the FP and FN, the more reliable the material decomposition.

### 4.3.1 Digital data

The digital phantom is the same with the one in Chapter 3.

Two other methods were compared to the proposed ROI-wise material decomposition method: (a) the common TV method as:

$$\underset{\boldsymbol{X}}{\operatorname{argmin}} \frac{1}{2}\|\boldsymbol{Y} - \boldsymbol{M}\boldsymbol{X}\|_F^2 + \lambda \|\boldsymbol{X}\|_{TV}; \tag{4.15}$$

(b) the Coarse method in (4.9). Note that the 'Coarse' method is also an intermediate step of the ROI-wise method, which can be utilized to evaluate the impacts of the involved basis material optimization and energy averaging-based denoising. For clarity, we denote the proposed ROI-wise material decomposition by 'ROI' method in the Figures.

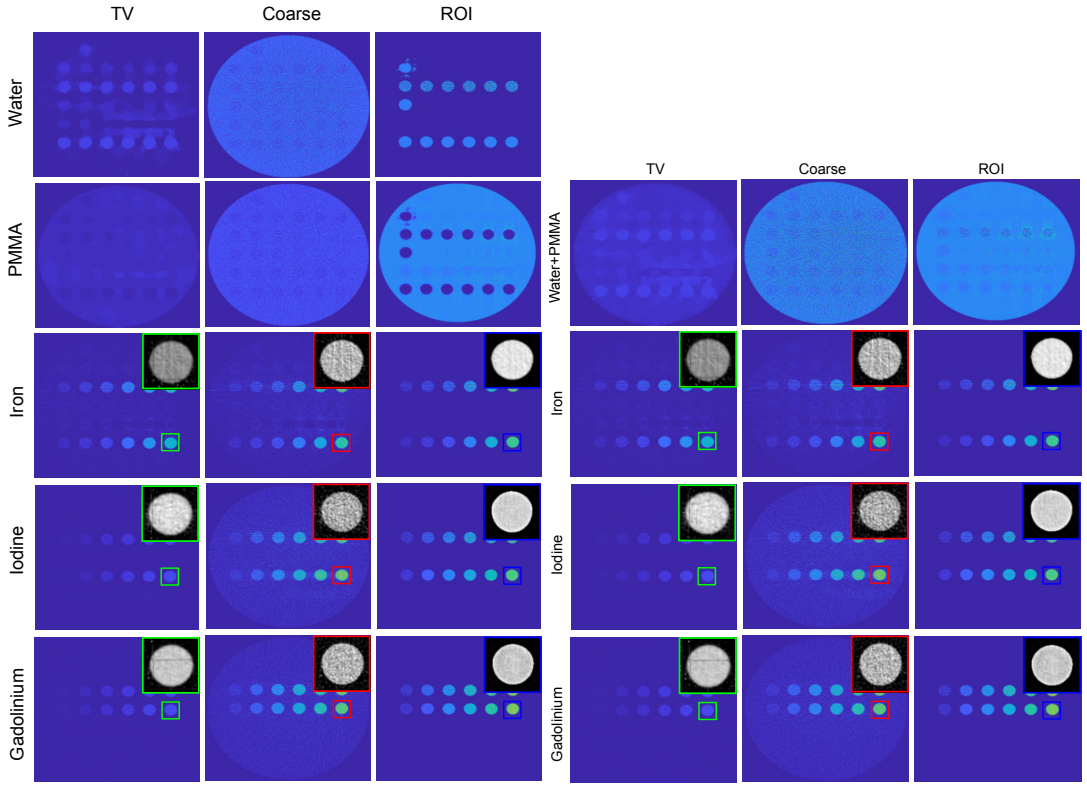


Figure 4.4: The results of material decomposition using three methods on digital phantom. Left to right: TV, Coarse and ROI decompositions.

The decomposition results of five basis materials ($K$=5: water, PMMA, iron, iodine and gadolinium) are shown in figure 4.4. In contrast to the other two methods, the proposed ROI-wise material decomposition method shows better detection ability in terms of edge-preserving performance. The images of water and PMMA are important, e.g., for non-contrast imaging. Visually, there are obviously more errors in water-like materials (*e.g.*, water and PMMA, *etc*) than in iron, iodine and gadolinium for all the three methods. However, compared to TV and Coarse method, the proposed ROI-wised method has better edge-preserving performance for water-like materials. In practical applications, the quantitative information of the last three materials are more useful, as a result of which we will pay more attention to the materials of interest: iron, iodine and gadolinium.

As an illustration, we list $error_m$ of iron, iodine and gadolinium for the three methods in Table 4.1. Clearly, ROI-wise method has the smallest $error_m$ for all the three materials compared to TV or Coarse method. We plot in figure 4.5 both measured and true concentrations of each vial and the corresponding linear regressions in the simulation experiment. As observed, the ROI-wise method has a constant behavior, namely the concentration of different inserts is always (except at the lowest concentration of 5 mg/cc) underestimated. In contrast, the other two methods present unpredictable behavior by either underestimating the concentration (for iron and gadolinium) or overestimating the concentration (for iodine).

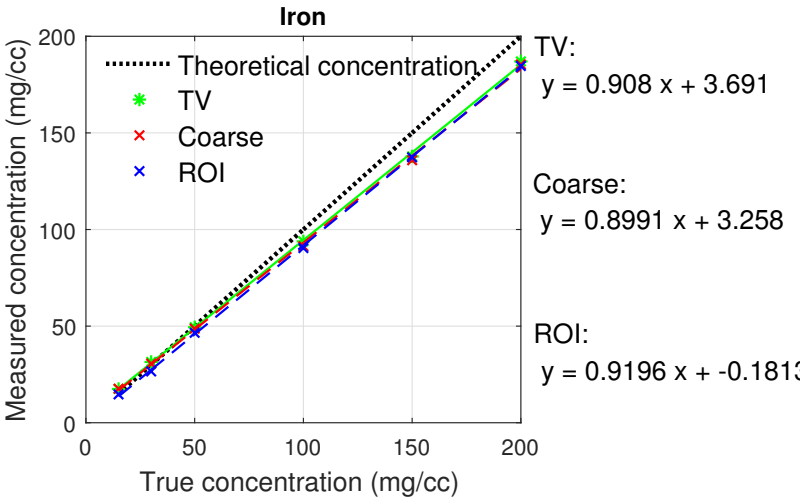


(a)

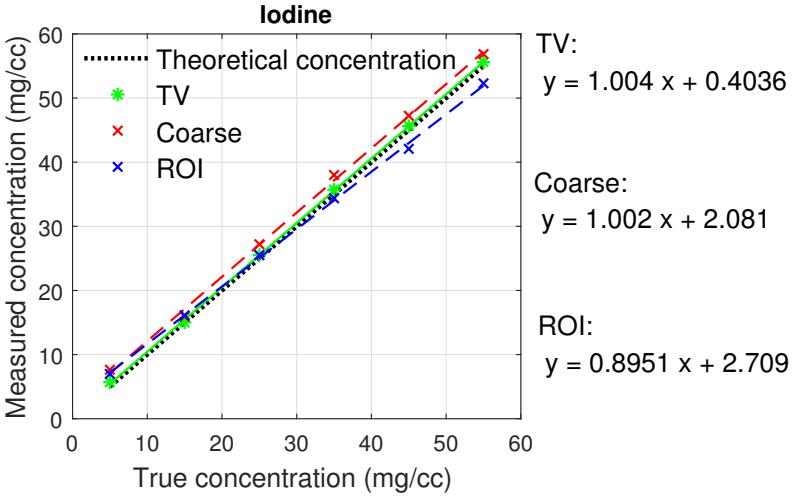


(b)

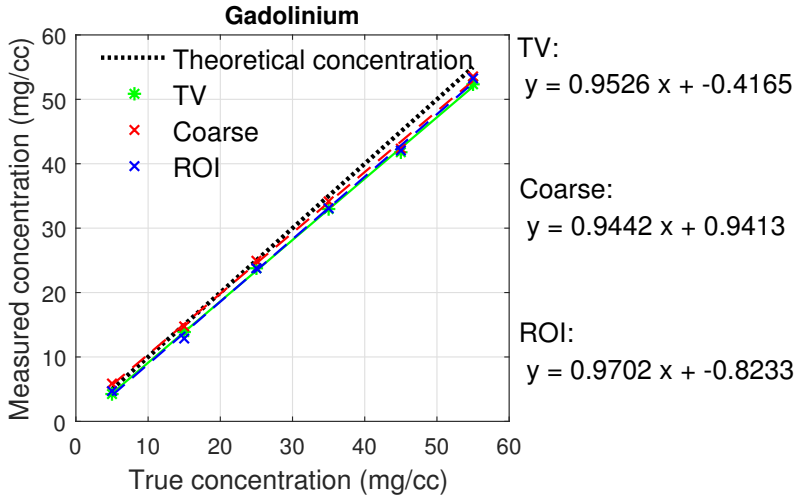


(c)

Figure 4.5: The linear regressions of material decomposition using three methods for (a) iron, (b) iodine and (c) gadolinium.

Table 4.1: The normalized Euclidean distance $error_m$ of different decomposition methods on digital phantom.

| Materials \ Methods | TV | Coarse | ROI |
|---|---|---|---|
| Iron | 0.21 | 0.23 | 0.14 |
| Iodine | 0.28 | 0.37 | 0.15 |
| Gadolinium | 0.26 | 0.31 | 0.12 |

The results in terms of FP and FN are given in Table 4.2. The proposed ROI-wise material decomposition method has a much smaller FP compared to the TV and Coarse methods. While for FN, the three methods exhibit similar performance for iodine and gadolinium, while for iron, ROI-wise method leads to obvious larger errors.

Table 4.2: The FP and FN rates of different decomposition methods on digital phantom.

| Materials \ Methods | | TV | Coarse | ROI |
|---|---|---|---|---|
| Iron | | 13.6 | 18.4 | 0.02 |
| Iodine | FP (%) | 5.2 | 9.6 | 0.01 |
| Gadolinium | | 4.9 | 6.1 | 0.01 |
| Iron | | 9.1 | 14.8 | 19.5 |
| Iodine | FN (%) | 29.3 | 28.5 | 29.9 |
| Gadolinium | | 28.0 | 26.3 | 30.3 |

### 4.3.2 Physical data

We show the results on both physical phantom and in vivo data which are the same with in Chapter 3.

The decomposition results of three basis materials ($K$=3: water-like, iodine and gadolinium) on the physical phantom are shown in figure 4.6. The proposed ROI-wise material decomposition method has clearly better performance in detection and quantification compared to TV and Coarse methods. Firstly, our method shows much better morphological accuracy, even for water-like materials. The selected areas for water-like materials using both TV and ROI-wise methods, shown in figure 4.7, illustrate that the edges of the selected areas are obviously blurred for both TV and Coarse methods but are more accurate for ROI-wise method. As observed, none of the three methods has accurately decomposed iodine with concentration 1 $mg/cc$. For example, ROI-wise method was not able to recognize iodine inside the disk, while the other two methods were not able to separate the iodine with water or gadolinium of 2 $mg/cc$.

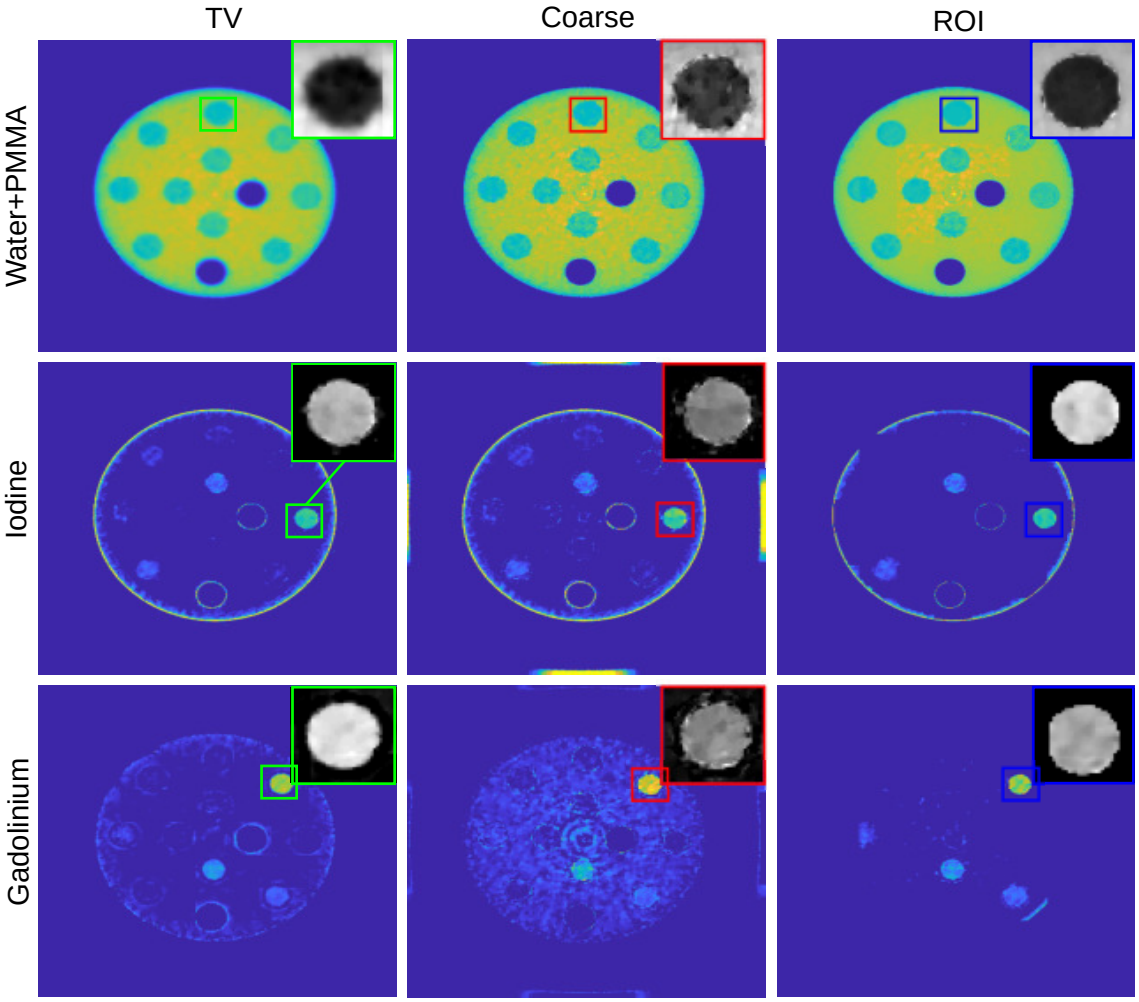


Figure 4.6: The results of material decomposition on physical phantom using three methods. Left to right: TV, Coarse and ROI decompositions.

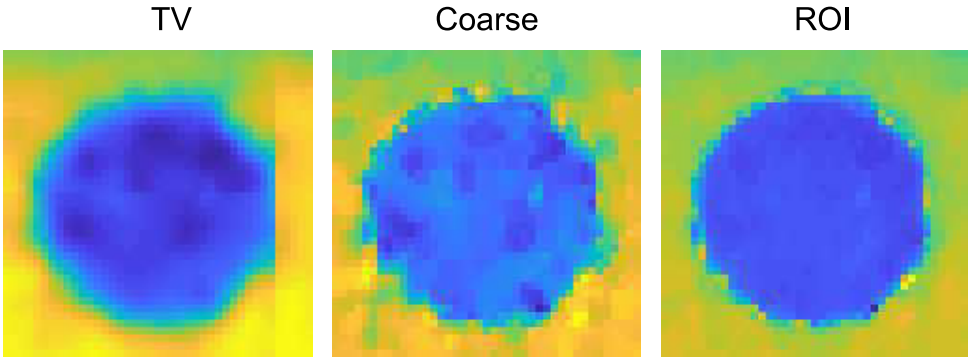


Figure 4.7: The results of decomposed water-like materials in selected areas in figure 4.6.

Secondly, more quantitatively as shown in Table 4.3, ROI-wise method has clearly smaller normalized Euclidean distance. Specially, ROI-wise method has higher accuracy for gadolinium than for iodine. We also list the mean error in each disk (*mean of each disk - ground-truth of each disk*) in Table 4.4 to further evaluate the decomposition performance of different concentrations. The mean errors of the ROI-wise method are always negative (i.e. underestimated) whatever the inserts, while the other two methods lead to either positive (i.e. overestimated) or negative mean errors, depending on inserts.

Table 4.3: The normalized Euclidean distances $error_m$ of different decomposition methods on physical phantom.

| Materials \ Methods | TV | Coarse | ROI |
|---|---|---|---|
| Iodine | 0.41 | 0.46 | 0.38 |
| Gadolinium | 0.26 | 0.98 | 0.23 |

Table 4.4: The mean error of decomposition in each disk on physical phantom.

| Materials | Methods | TV | Coarse | ROI |
|---|---|---|---|---|
| Iodine | 1 (mg/cc) | 0.4 | 0.1 | -1 |
| | 3.5 | -0.8 | -1 | -0.6 |
| | 7 | -3.1 | -3.4 | -2.7 |
| | 14 | -4.1 | -4.0 | -4.5 |
| Gadolinium | 2 | -0.7 | 1.7 | -0.3 |
| | 4 | -0.9 | 1.4 | -0.3 |
| | 8 | -2.2 | 1.3 | -2.2 |
| | 16 | -2.4 | 0.8 | -3.0 |

Table 4.5 lists both FN and FP for different materials using the three methods among which the proposed ROI-wise method exhibits the best accuracy. Especially for FP rate, the proposed ROI-wise method can have even 88% improvement for iodine and 95% for gadolinium compared to the Coarse method.

Table 4.5: The FP and FN rates of different decomposition methods on physical phantom.

| Materials | Methods | TV | Coarse | ROI |
|---|---|---|---|---|
| Iodine | FP (%) | 7.3 | 11.7 | 1.4 |
| Gadolinium | | 28.9 | 84.3 | 4.4 |
| Iodine | FN (%) | 5.1 | 4.2 | 4.5 |
| Gadolinium | | 2.0 | 0.7 | 1.8 |

Concerning the influence of important kernel parameters including the weight of spatial kernel $\theta$ and the variance of the Gaussian distribution $\sigma$, the decomposition performance of iodine with different $[\theta\ \sigma^2]$ is listed in Table 4.6 (noting that gadolinium has

the same trend for [$\theta$ $\sigma^2$], no longer listed here). A too small or big $\theta$ can lead to larger normalized Euclidean distance $error_m$. An intermediate value of $\theta = 0.2$ was selected in the experiment. $\sigma$ shows less impact on the decomposition, as a result of which we chose $\sigma^2 = 0.5$ according to its overall smaller $error_m$ for different $\theta$.

Table 4.6: The normalized Euclidean distances $error_m$ of different decomposition methods on physical phantom.

| $\theta$ \ $\sigma_s/\sigma$ | 0.2 | 0.4 | 0.6 | 0.8 | 1 |
|---|---|---|---|---|---|
| 0 | 0.26 | 0.26 | 0.26 | 0.26 | 0.26 |
| 0.2 | 0.22 | 0.22 | 0.22 | 0.22 | 0.22 |
| 0.4 | 0.22 | 0.21 | 0.22 | 0.22 | 0.22 |
| 0.6 | 0.20 | 0.26 | 0.21 | 0.21 | 0.22 |
| 0.8 | 0.21 | 0.22 | 0.22 | 0.38 | 0.22 |
| 1 | 0.21 | 0.22 | 0.22 | 0.21 | 0.39 |

$\lambda$ is 1e-5 for both equation 4.10 and 4.13, with which the sparsity constraint is relatively small. To evaluate the impact of lambda on the decomposition, we give more details about the material decomposition with different lambda in Coarse method, and the results are shown in figure 4.8. The results show that the RMSE of decomposition varies relatively smoothly with the sparsity constraint when lambda is smaller than 1e-5. Specifically, the sparsity using L1-constraint (Coarse) has stable and relatively smaller influence on the decomposition results. As a result, the improvement of our results should mainly come from the coarse-fine procedure.

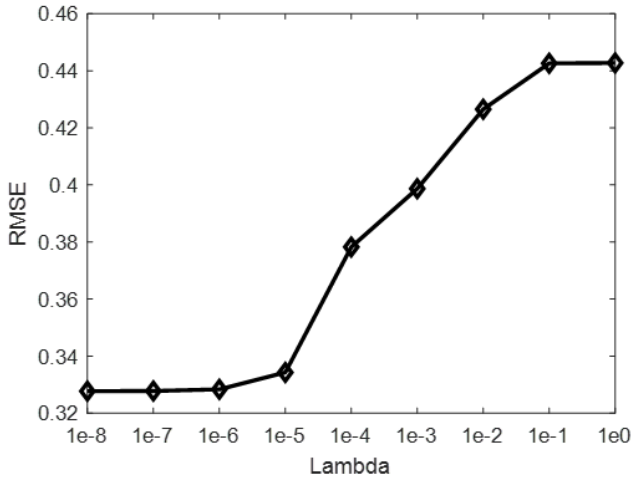


Figure 4.8: Influence of $\lambda$ on the RMSE using Coarse method.

Moreover, the influence of the relative population threshold $T$ is illustrated in figure 4.9. Both a smaller or bigger $T$ can lead to larger $error_m$. However, the error varies relatively smoothly with T, especially for gadolinium. In our setup, we chose $T = 0.4$ that corresponds to the smallest normalized Euclidean distance.

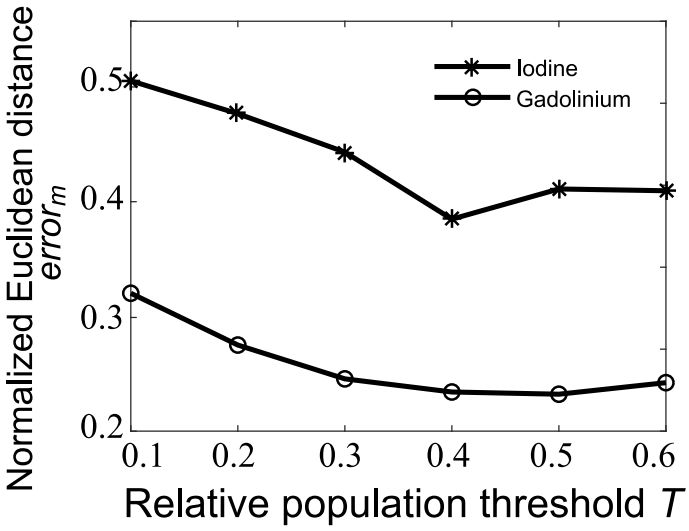


Figure 4.9: Influence of relative population threshold on the normalized Euclidean distance for iodine and gadolinium.

The decomposition results of the in vivo data are shown in figure 4.10. Both TV and L1 methods produce noisier results for both iodine and gadolinium. On the contrary, the proposed ROI-wise method has better detection ability for both iodine and gadolinium. Specifically, although all the three methods can detect iodine in the spine, the ROI-wise method gives the highest accuracy considering it reduce obviously noise in the background. For gadolinium, Table 4.7 lists the decomposed concentration of each tube. Clearly, the ROI-wise method presents the highest accuracy (the smallest error) for all the measured concentrations.

Table 4.7: The mean error of decomposed gadolinium in each tube on in vivo data.

| Methods / True Conc. | TV | Coarse | ROI |
|---|---|---|---|
| 10 (mg/cc) | -3.3 | -3.2 | -1.0 |
| 5 | -3.8 | -2.7 | -0.6 |
| 2 | -2.0 | -1.2 | -1 |

## 4.4 Discussion and conclusion

We have proposed a ROI-wise material decomposition method. The proposed method enables materials to be more reliably and accurately decomposed. This is mainly due to the introduction of spatio-spectral segmentation that allows pertinent features encoded in multi-energy sCT images to be extracted for basis materials optimization.

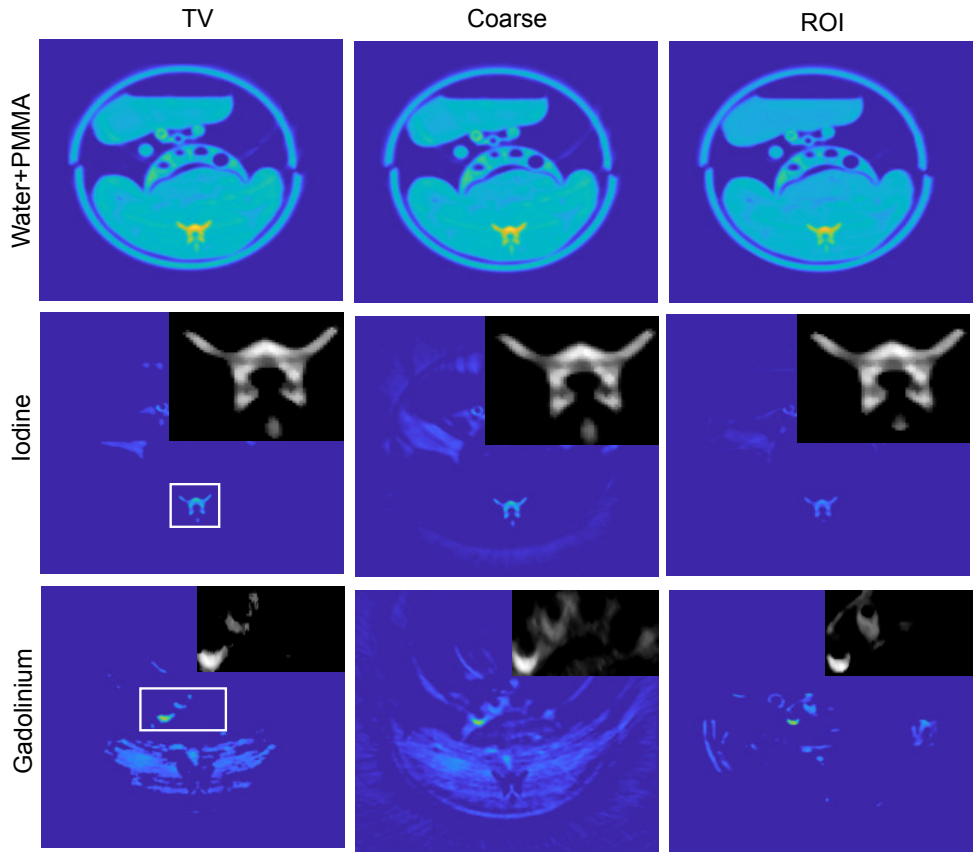


Figure 4.10: The results of material decomposition based on physical phantom. Left to right: Pseudo-inverse with TV, Coarse and ROI.

### Generality of the method

The proposed ROI-wise method is generic in the sense that it provides a framework for obtaining material decomposition from spatial reconstructed images. It provides promising perspectives for both medical applications and industrial nondestructive evaluation, considering its high accuracy and reliability. In addition to contrast agent imaging applications, our method can also be used for non-contrast imaging in medical applications. Indeed, in this work, we focused on five basis materials: water, PMMA, iron, iodine and gadolinium. Although none of the three methods can separate water and PMMA, the proposed ROI-wised method has nevertheless better edge-preserving performance for both water and PMMA, which implies that it can improve the performance of non-contrast imaging.

### Reliability and sensitivity

The results show that the ROI-wise material decomposition method favors more reliability while the sensitivity of detecting materials is somewhat sacrificed as the trade-off. This may partly explain why only materials with a concentration over certain limit could be accurately decomposed. This is the case for iodine with concentration 1 $mg/cc$ com-

pared to higher concentrations (figure 4.6). These results are consistent with the high improvement of FP (88% improvement for iodine and 95% for gadolinium compared to the Coarse method on physical phantom) while similar performance of FN (even worse compared to Coarse). Although Coarse or TV method shows better FN for certain materials (*e.g.* Coarse and TV for iron on digital phantom, and Coarse for gadolinium on physical phantom), the two methods cannot separate materials of small concentrations or water-like materials. In other words, Coarse or TV method produced smaller FN at the cost of confusing materials of interest with water-like materials. For example, smaller FN of Coarse method compared to ROI method on physical phantom is ascribed to the fact that Coarse method was not able to detect gadolinium of 2 $mg/cc$ from water or iodine of 1 $mg/cc$. The above detection limit of the proposed method is due to multiple factors, such as the performance of reconstruction and ROI segmentation. In clinical applications, although both FN and FP are preferred to be as small as possible, the focus depends on concrete situations. For example, false positive diagnoses of potential cancers create clinical uncertainty and often lead to multiple unnecessary biopsies or in certain cases surgical management of low-grade and low-volume disease [Quon et al., 2015]. Conversely, false negative diagnoses in terms of missing or delaying a diagnosis can also lead to real risks [Verbeek and Roobol, 2018].

The trade-off between sensitivity and reliability of the proposed ROI-wise method is regularized by the threshold $T$ in the relative population thresholding. As shown in figure 4.9, too small or too large $T$ induced the increase of decomposition errors, because smaller $T$ leads to poor reliability (but high sensitivity). In other words, when $T$ is too small, noise and reconstruction errors will have a strong impact on decomposition accuracy. On the opposite, excessive $T$ will degrade the decomposition ability for materials of small concentration. Fortunately, the results show a relatively large range for the choice of $T$ around the optimal value, which implies that the proposed method is relatively little sensitive to $T$.

**Influence of image reconstruction quality**

Finally, it is worth noting that image reconstruction quality has dramatical influence on the performance of material decomposition in image domain. Because of excessively low dose allocated to detectors, sCT reconstruction at each energy bin is a problem of low-dose CT reconstruction, which is also a challenging problem. A worse image reconstruction quality may deteriorate the performance of ROI segmentation, which in return may influence the accuracy of ROI-wise method, especially for images containing small structures (*e.g.*, small blood vessels). We have chosen a common but efficient algorithm in the field of low-dose CT reconstruction (SART-TV) to reconstruct sCT images. Note that there are many other methods that jointly reconstruct sCT image to mitigate artifacts [Gao et al., 2011, Yu et al., 2016, Liu et al., 2016, Zhang et al., 2017, Leng et al., 2011, Li et al., 2017], which will in turn improve the performance of image-domain material decomposition. The results of reconstruction using SART-TV still show obvious artifacts and noise. Nevertheless, even in this situation, the materials were still correctly decomposed on both digital and physical phantoms, which demonstrates the reliability of the proposed ROI-wise method.

In conclusion, we have proposed a ROI-wise material decomposition method for sCT

by jointly optimizing basis materials and reducing noise. This is achieved through spatio-energy segmentation and exploiting both morphological and spectral information in the sCT images. The results on digital and physical phantoms showed that the ROI-wise material decomposition method presents clearly higher accuracy and reliability compared to common decomposition methods based on TV or *lasso* regularization. In the future work, the ability of detecting low-concentration materials will further be investigated to improve the sensitivity of the method while maintaining reliability. Meanwhile, the ability of identifying small structures having small material concentration will also be investigated.

# Chapter 5

# Super-Energy-Resolution Material Decomposition in Spectral Photon-Counting CT Using Pixel-Wise Learning

## Contents

## 5.1 Introduction

It is a huge challenge to obtain high accuracy of material decomposition in clinical applications, especially for low-concentration materials [Chandarana et al., 2011, Jacobsen et al., 2019]. This is linked to the principle itself of sCT. With respect to conventional CT or dual-energy CT to some extent, sCT divides the whole energy range into so-called energy bins. More there are energy bins, the higher energy resolution (narrower energy-bin width) and more accurate material decomposition. However, more energy bins means at the same time less photons in each energy bin and consequently higher quantum noise. In other words, energy resolution of sCT is limited by a trade-off between the total number of energy bins and the image quality at each bin, which restricts the accuracy of material decomposition and ability of detecting low-concentration materials.

Most decomposition methods try to improve performance of material decomposition by exploiting the high correlation between spectral and spatial features embedded in the multi-energy images. However, almost no work can be found in the literature to enhance energy resolution of sCT by software.

In this chapter, we propose to introduce the notion of super-energy-resolution (SER) for sCT in order to improve material decomposition accuracy. The idea is to learn the relationship between spectral features of simulated data and those of physical data, then applying it to other physical data. To do it, theoretical sCT images containing abundant spectrum information, designated as SER images, are simulated according to physical phantoms. The mapping between actual sCT images and SER images are learned by utilizing a coupled dictionary learning (CDL) method in a pixel-wise way. SER images synthesized based on the learned mapping are then used for material decomposition in image-domain.

## 5.2 Trade-off between number of energy bins and undesired factors such as random noise

The measured signals are assumed to be corrupted by independent Poisson noise, discussed in Equation (2.7), listed again here:

$$M_i \sim \text{Poisson}(\text{mean} = n_i(P_\alpha)), \tag{5.1}$$

Noise of X-ray CT image is inversely related to the square root of the total number of photons used for reconstruction [Leng et al., 2011]. In other words, sCT suffers from stronger quantum noise for narrower bin.

Meanwhile, as discussed in Section 2.2, material decomposition in image-domain can be formulated in matrix form as:

$$\boldsymbol{Y} = \boldsymbol{M}\boldsymbol{X} + \boldsymbol{N}, \tag{5.2}$$

where $\boldsymbol{Y} \in \mathcal{R}^{B \times N_P}$ denotes the reconstructed multi-energy spatial images of $\boldsymbol{\mu}$ with $N_P$ indicating the total number of pixels or voxels, $\boldsymbol{M} \in \mathcal{R}^{B \times M}$ the decomposition matrix of $\boldsymbol{\mu_m}$, $\boldsymbol{X} \in \mathcal{R}^{M \times N_P}$ the decomposed basis material images of mass densities $\boldsymbol{\rho}$ and $\boldsymbol{N}$ the

noise. Generally, atoms in the decomposition matrix can be initialized by the effective mass attenuation coefficients [Le Huy and Molloi, 2011] according to:

$$\dot{\mu}_{m\alpha}(i) = \frac{\int_{E\in E_i} n_0(E) d_i(E) \mu_{m\alpha}(E) dE}{\int_{E\in E_i} n_0(E) d_i(E) dE}, \quad i = 1, ..., B, \tag{5.3}$$

where $\mu_{m\alpha}(E)$ is the theoretical mass attenuation coefficient at energy $E$ retrieved from NIST [Saloman and Hubbell, 1986], and $\int_{E\in E_i} n_0(E)dE$ the total number of incident photons belonging to the $i$-th energy bin of width $E_i$. $\dot{\mu}_{m\alpha}(i)$ represents the averaged value of all the theoretical mass attenuation coefficients inside the entire energy bin, which is an estimate of the true mass attenuation coefficient corresponding to that energy bin. As a result, thinner bins can produce more precise $\dot{\mu}_{m\alpha}(i)$, *i.e.* more precise $\boldsymbol{M}$.

As a result, the aforementioned trade-off between the number of energy bins and noise level leads to limited energy resolution in sCT. In practice, the number of energy bins of sCT is always constrained, *e.g.* 5 bins for Phillips sCT prototype [Si-Mohamed et al., 2018, Cormode et al., 2017].

## 5.3 Super-energy-resolution imaging using pixel-wise learning

This section firstly presents super-energy-resolution (SER) imaging in sCT. Then, the SER image synthesis method is introduced. At last, SER-based material decomposition is described in detail.

### 5.3.1 SER imaging in sCT

We propose to improve the energy resolution by means of fully exploiting both simulation data and physical data. To do it, SER is introduced in sCT.

SER images are virtual multi-energy images with much more bins but noise-reduced compared to the actual sCT images. figure 5.1 illustrates the relationship between actual sCT, denoted by low-energy-resolution (LER) imaging, and SER imaging by respectively plotting the multi-energy values of corresponding pixels in the LER and SER images. For one pixel in the reconstructed LER images (*e.g.* yellow asterisks in the left of figure 5.1, designated as $\boldsymbol{y_L} \in \mathcal{R}^{B_L}$), it has 5 values for 5 energy bins, *i.e.* $B_L = 5$. While for the corresponding SER pixel (yellow points in the right of figure 5.1, designated as $\boldsymbol{y_S} \in \mathcal{R}^{B_S}$), it can have much more values, *e.g.* 50 values for $B_S = 50$ (30 - 80 keV). Note that the choice of 50 bins corresponds to the most precise $\mu_m$ we can get from NIST. That is, $\mu$ is sampled every 1 keV [Saloman and Hubbell, 1986].

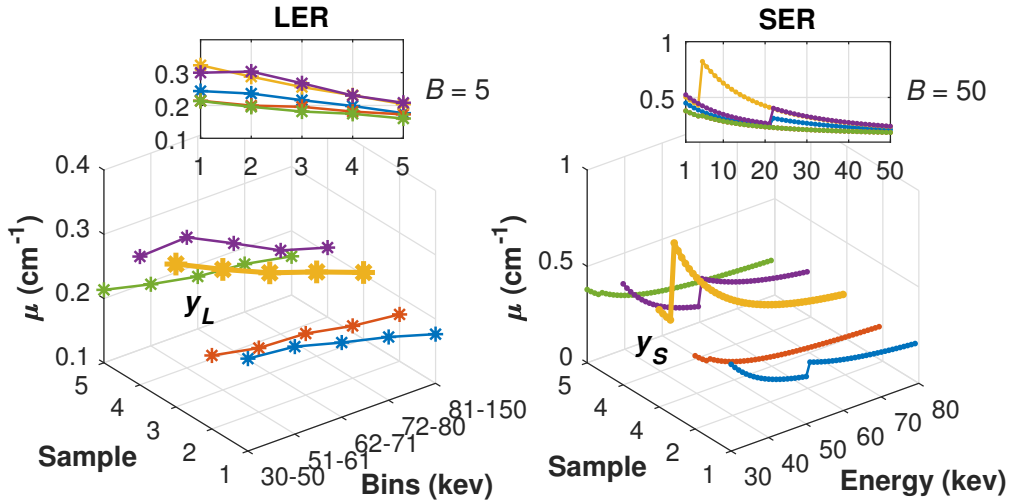


Figure 5.1: Linear attenuation coefficients: LER (left) and SER (right). Curves with different colors denote different pixels; corresponding LER and SER pixels have the same color.

The proposed SER imaging is achieved by introducing the assumption that if containing the same basis materials and concentrations, the mapping between LER and SER images is determined and can be learned. We realize it by learning the relationship between physical data and simulation data and then applying it to other physical data, as illustrated in figure 5.2. The physical data are measured and reconstructed as LER images, while the corresponding SER versions are produced by simulation with same shapes and components but more bins. Then, LER and SER spectral features are extracted and their relationship will be learned by a mapping which can be utilized to synthesize SER images for other in vivo data.

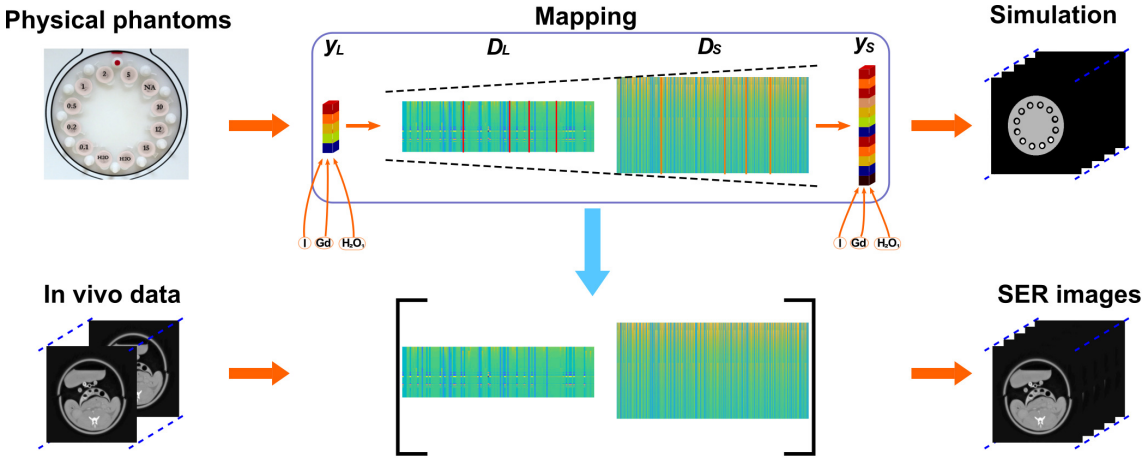


Figure 5.2: Illustration of SER based sCT imaging.

### 5.3.2 SER image synthesis based on coupled dictionary learning

We learn the mapping between LER and SER spectral features by utilizing CDL method in a pixel-wise way.

#### Pixel-wise training strategy

It is inefficient to directly learn the mapping from the whole LER and SER images or patches. In general, learning morphological features of certain organ or more is another challenge that demands abundant images with various spatial information for training. It will be expensive to produce these kinds of physical data currently. Meanwhile, the complex material components can make the learning more difficult.

We solve it by training the mapping form LER and SER pixel pairs, rather than the whole images or patches. With this strategy, the training samples only contain spectral information. Correspondingly, the physical phantoms used in our work can have simple shapes, but abundant material components.

Meanwhile, to cope with the difficulty of extracting features from noisy LER pixels, we enhance the learning by adding conventional CT images. The conventional CT images of physical phantoms are measured on the same machine but reconstructed with full spectrum, thus having lower noise level compared to with single energy bin. The conventional CT and sCT pixels are then concatenated together as one LER sample for training. As a result, now $\boldsymbol{y_L} \in \mathcal{R}^{(B_L+1)}$ is a combined LER pixel.

#### Learn the mapping by CDL

CDL was used in the field of spatial super resolution [Yang et al., 2010, Wang et al., 2012, Hu et al., 2018]. In the theory of dictionary learning, features of a pixel $\boldsymbol{y}$ can be represented as a sparse combination of atoms inside an over-complete dictionary $\boldsymbol{D}$. That is, $\boldsymbol{y} = \boldsymbol{D\alpha}$, where $\boldsymbol{\alpha}$ is the sparse codes with very few nonzero entries:

$$\text{argmin}\|\boldsymbol{\alpha}\|_0, \quad \text{s.t.} \quad \|\boldsymbol{y} - \boldsymbol{D\alpha}\|_2^2 \leq \epsilon \tag{5.4}$$

where $\|\boldsymbol{\alpha}\|_0$ designates $L_0$ norm of $\boldsymbol{\alpha}$. Generally, solving optimization problem in (5.4) is NP-hard, and it can be instead solved using $L_1$ norm, as:

$$\underset{\boldsymbol{\alpha}}{\text{argmin}}\|\boldsymbol{y} - \boldsymbol{D\alpha}\|_2^2 + \lambda\|\boldsymbol{\alpha}\|_1, \tag{5.5}$$

where $\lambda$ is the Lagrange parameter.

LER and SER pixel sets can then be separately represented using a LER dictionary $\boldsymbol{D_L}$ and a SER dictionary $\boldsymbol{D_S}$:

$$\begin{aligned} &\underset{\boldsymbol{\Lambda_L}}{\text{argmin}}\|\boldsymbol{Y_L} - \boldsymbol{D_L\Lambda_L}\|_F^2 + \lambda_L\|\boldsymbol{\Lambda_L}\|_1, \\ &\underset{\boldsymbol{\Lambda_S}}{\text{argmin}}\|\boldsymbol{Y_S} - \boldsymbol{D_S\Lambda_S}\|_F^2 + \lambda_S\|\boldsymbol{\Lambda_S}\|_1, \end{aligned} \tag{5.6}$$

where $\boldsymbol{Y_L} \in \mathcal{R}^{(B_L+1)\times N_t}$ and $\boldsymbol{Y_S} \in \mathcal{R}^{B_S\times N_t}$ respectively designate the LER and SER pixel sets with $N_t$ pixels in the training set, $\boldsymbol{D_L} \in \mathcal{R}^{(B_L+1)\times N_D}$ and $\boldsymbol{D_S} \in \mathcal{R}^{B_S\times N_D}$ the LER and

SER dictionaries containing $N_D$ atoms, $\boldsymbol{\Lambda_L}$ and $\boldsymbol{\Lambda_S}$ the corresponding sparse codes, and $\|\boldsymbol{Y} - \boldsymbol{D\Lambda}\|_F^2$ the data fidelity term calculated in terms of Frobenius Norm $\|\cdot\|_F$. Then, the connection between LER and SER features is established by jointly training $\boldsymbol{D_L}$ and $\boldsymbol{D_S}$, formulated as:

$$\begin{aligned} &\underset{\widetilde{\Lambda},\widetilde{D}}{\operatorname{argmin}} \|\widetilde{\boldsymbol{Y}} - \widetilde{\boldsymbol{D}}\widetilde{\boldsymbol{\Lambda}}\|_F^2 + \lambda\|\widetilde{\boldsymbol{\Lambda}}\|_1, \\ &s.t. \quad \widetilde{\boldsymbol{Y}} = \begin{bmatrix} \boldsymbol{Y_S} \\ \boldsymbol{Y_L} \end{bmatrix}, \widetilde{\boldsymbol{D}} = \begin{bmatrix} \boldsymbol{D_S} \\ \boldsymbol{D_L} \end{bmatrix}, \widetilde{\boldsymbol{\Lambda}} = \begin{bmatrix} \boldsymbol{\Lambda_S} \\ \boldsymbol{\Lambda_L} \end{bmatrix}. \end{aligned} \tag{5.7}$$

Meanwhile, a transform matrix is utilized to decrease the impacts of dramatic gap between simulation and physical data:

$$\boldsymbol{\Lambda_S} = \boldsymbol{W\Lambda_L}, \tag{5.8}$$

where $\boldsymbol{W}$ denotes the transform matrix that was firstly introduced in spatial super resolution for stable cross-style image synthesis [Wang et al., 2012]. The enhanced training model then becomes:

$$\begin{aligned} &\underset{\boldsymbol{D},\boldsymbol{\Lambda},\boldsymbol{W}}{\operatorname{argmin}} \|\boldsymbol{Y_S} - \boldsymbol{D_S\Lambda_S}\|_F^2 + \|\boldsymbol{Y_L} - \boldsymbol{D_L\Lambda_L}\|_F^2 \\ &+ \gamma\|\boldsymbol{\Lambda_S} - \boldsymbol{W\Lambda_L}\|_F^2 + \lambda_W\|\boldsymbol{W}\|_F^2 + \lambda_S\|\boldsymbol{\Lambda_S}\|_1 + \lambda_L\|\boldsymbol{\Lambda_L}\|_1. \end{aligned} \tag{5.9}$$

We solve the above model by the alternating direction method of multipliers (ADMM) iteration method [Boyd et al., 2010], which alternately updates coupled dictionaries $\widetilde{\boldsymbol{D}}$, sparse codes $\widetilde{\boldsymbol{\Lambda}}$ and transform matrix $\boldsymbol{W}$, as in Algorithm 2.

**Algorithm 2 ADMM of training the coupled dictionaries**

**Input:** $\boldsymbol{Y_L}, \boldsymbol{Y_S}$ (training pairs)
**Initialization:** $\boldsymbol{D_S}$, $\boldsymbol{D_L}$, $\boldsymbol{\Lambda_S}$, $\boldsymbol{\Lambda_L}$ **and** $\boldsymbol{W}$
**Training:**
  **while** *condition*
    **update sparse codes:** $\boldsymbol{\Lambda_S}$, $\boldsymbol{\Lambda_L}$
    **update coupled dictionaries:** $\boldsymbol{D_S}$, $\boldsymbol{D_L}$
    **update transform matrixes:** $\boldsymbol{W}$
  **end**
**Output:** $\boldsymbol{D_S}$, $\boldsymbol{D_L}$ and $\boldsymbol{W}$

It should be noted that atoms in the dictionaries learned using a pixel-wise strategy are energy-dependent, in contrary to spatial features in traditional spatial-super-resolution applications. figure 5.3 illustrates the difference between spatial super resolution and super energy resolution by showing the learned features. Atoms learned from a spatial image are morphological features, while for SER, atoms in the dictionary are energy-dependent and look more like $\mu$ curves.

After training, we can easily synthesize SER pixel $\hat{\boldsymbol{y}}_{\boldsymbol{S}}$ from its LER version $\boldsymbol{y_L}$ with the learned coupled dictionaries and transform matrix, by solving the following optimiza-

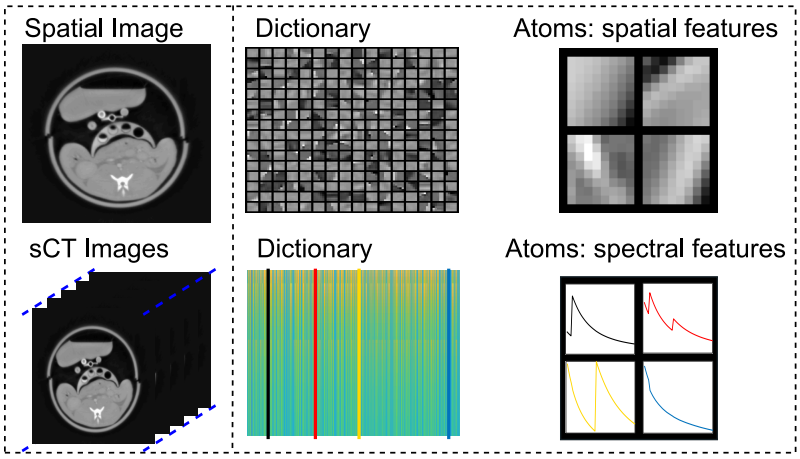


Figure 5.3: Features Learned with dictionary learning method for spatial super resolution and super energy resolution. Note that the dictionary for sCT images (lower) is the SER dictionary.

tion:

$$\begin{aligned}&\mathbb{SER}(\boldsymbol{y_L} \rightarrow \hat{\boldsymbol{y}}_S):\\ &\underset{\hat{\boldsymbol{y}}_S}{\operatorname{argmin}} \|\hat{\boldsymbol{y}}_S - \boldsymbol{D_S}\boldsymbol{\alpha_S}\|_F^2 + \|\boldsymbol{y_L} - \boldsymbol{D_L}\boldsymbol{\alpha_L}\|_F^2\\ &+ \gamma\|\boldsymbol{\alpha_S} - \boldsymbol{W}\boldsymbol{\alpha_L}\|_F^2 + \lambda_S\|\boldsymbol{\alpha_S}\|_1 + \lambda_L\|\boldsymbol{\alpha_L}\|_1. \end{aligned} \tag{5.10}$$

### 5.3.3 Material decomposition using SER images

The synthesized SER images are then utilized for image-domain material decomposition. A more precise decomposition matrix $\boldsymbol{M}$ suitable for the SER images is then needed. For LER, $\boldsymbol{\mu_m}$ of each basis material (one column of $\boldsymbol{M}$ in equation (5.2) designated as $\boldsymbol{M_L}$) is an effective value on $B_L$ energy bins. In contrast, $\boldsymbol{M}$ for SER (designated as $\boldsymbol{M_S}$) has much more energy bins, *e.g.* $B_S = 50$. Each column of $\boldsymbol{M_S}$ is a more precise value directly retrieved from NIST, as illustrated in figure 5.4.

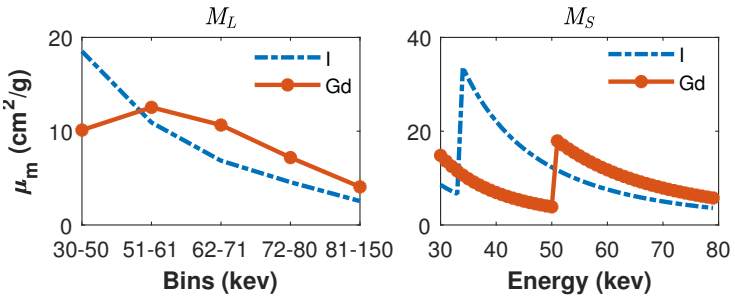


Figure 5.4: Mass attenuation coefficients in $\boldsymbol{M_L}$ and $\boldsymbol{M_S}$ for iodine and gadolinium.

To evaluate the decomposition performance of the synthesized SER images, we choose a common image-domain decomposition method using $L_1$ norm (lasso) regularization.

Mathematically, we formulate the SER-based material decomposition using lasso as:

$$\hat{\boldsymbol{x}} = \underset{\boldsymbol{x}}{\operatorname{argmin}} \|\hat{\boldsymbol{y}}_S - \boldsymbol{M}_S \boldsymbol{x}\|_F^2 + \lambda \|\boldsymbol{x}\|_1. \tag{5.11}$$

The total algorithm of SER based material decomposition is shown in Algorithm 3.

**Algorithm 3 SER based Material Decomposition**

**Input:**
**Data:** $\boldsymbol{y}_L$ (testing pixel)
**Learned:** $\boldsymbol{D}_S$, $\boldsymbol{D}_L$ and $\boldsymbol{W}$

**SER Image Synthesis**
$\mathbb{SER}(\boldsymbol{y}_L \rightarrow \hat{\boldsymbol{y}}_S)$

**Material Decomposition Using Synthesized SER Images**
$\hat{\boldsymbol{x}} = \underset{\boldsymbol{x}}{\operatorname{argmin}} \|\hat{\boldsymbol{y}}_S - \boldsymbol{M}_S \boldsymbol{x}\|_F^2 + \lambda \|\boldsymbol{x}\|_1.$

**Output:** $\hat{\boldsymbol{x}}$

## 5.4 Experiments and results

The performance of the proposed ROI-wise material decomposition method was evaluated on both digital and physical phantom data.

### Image quality metrics

Both SER images synthesis and material decomposition were quantitatively evaluated. Normalized Root Mean Square Error (NRMSE) (*i.e.* NRMSE = RMSE/$\bar{x}$ for the image $x$) and peak signal-to-noise ratio (PSNR) were utilized to assess the quality of synthesized SER images. Note that NRMSE and PSNR were respectively calculated on the whole images of iodine and gadolinium, in order to show the total synthesis performance of all concentrations. The smaller the NRMSE and the higher the PSNR, the more accurate the synthesis.

To evaluate the accuracy of material decomposition, mean and standard deviation ($\delta$) were calculated for each dilution. Meanwhile, linear regression between the nominal (y-axial) and measured concentrations (using the calculated mean values, x-axial) was performed for all dilutions, as: $y = ax + b$, where $a$ and $b$ represent the slope and y-intercept, respectively. To further assess the detection ability of contrast agents, we also calculated the limit of detection (LOD) for both iodine and gadolinium. The LOD was described by the Clinical and Laboratory Standards Institute [Moretti et al., 2011] as:

$$\begin{aligned} \mathrm{LOB} &= \bar{x}_{\mathrm{blank}} + 1.645\delta_{\mathrm{blank}}, \\ \mathrm{LOD} &= \frac{\mathrm{LOB} - b}{a}, \end{aligned} \tag{5.12}$$

where $\bar{x}_{\mathrm{blank}}$ denotes mean water signal detected in the images of decomposed contrast agents, $\delta_{\mathrm{blank}}$ the standard deviation of the measurement and LOB the limit of blank.

LOB denotes the highest apparent contrast agent concentration expected to be found when replicates of a sample contain no contrast agent, which was calculated using tubes of water in each phantom. LOD is taken as the lowest concentration of a contrast agent in a sample that can be detected.

### 5.4.1 Digital data

#### Digital phantom data generation

The data of sCT was simulated using INSA software Virtual X-ray Imaging (VXI) [Duvauchelle et al., 2000]. For LER imaging, the X-ray energy bins were set as: 30-40kev, 40-50kev, 50-60kev, 60-70kev and 70-80kev, while for SER, bin interval is equally set as 1keV in the range of 30-80 kev. The detector response function was considered ideal in the simulation.

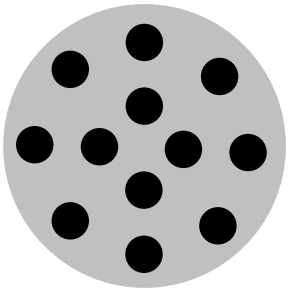

Figure 5.5: Digital phantom.

In our experiments, 11 phantoms were generated, which have the same shape but different materials. The impact of phantom shapes on decomposition was considered insignificant in this work, because SER imaging focus on spectral features rather than spatial ones. Each reconstructed phantom (one slice) has 256*256 pixels and contains five materials: water, PMMA, gadolinium (Gd) and iodine (I), one of which is shown in figure 5.5. Disks in different phantoms contain mixtures of different concentration in the range of 0-20 mg/cc for both I and Gd. As a result, 655 thousands of training pairs were extracted from 10 of the 11 phantoms for training, while the left one for testing. Note that the digital phantom for testing has the same material components and concentration with the physical phantom discussed in Chapter 3 (figure 3.9).

#### Results

Two kinds of sCT images were utilized to evaluate the proposed SER-based material decomposition: LER images $\boldsymbol{Y_L}$ and synthesized images $\hat{\boldsymbol{Y}}_{\boldsymbol{S}}$. The corresponding results of material decomposition are respectively denoted as $\boldsymbol{X_L}$ and $\hat{\boldsymbol{X}}_{\boldsymbol{S}}$.

Firstly, we show the performance of synthesized SER images based on CDL. Four atoms in the trained dictionary for SER images are shown in figure 5.6. The images can be represented by atoms multiplied by sparse coding coefficients. The results in terms of of RMSE and PSNR (dB) of synthesized SER images $\hat{\boldsymbol{Y}}_{\boldsymbol{H}}$ and interpolated up-sampled images $\hat{\boldsymbol{Y}}_{\boldsymbol{L}}$ are plotted in figure 5.7. $\hat{\boldsymbol{Y}}_{\boldsymbol{H}}$ have better precision in terms of smaller RMSE and

higher PSNR. The synthesized SER images based on dictionary learning have obviously better precision of reconstruction, compared to the high-dimensional images interpolated based on pre-material-decomposition. It should be noticed that RMSE and PSNR are worse at the energy of k-edge.

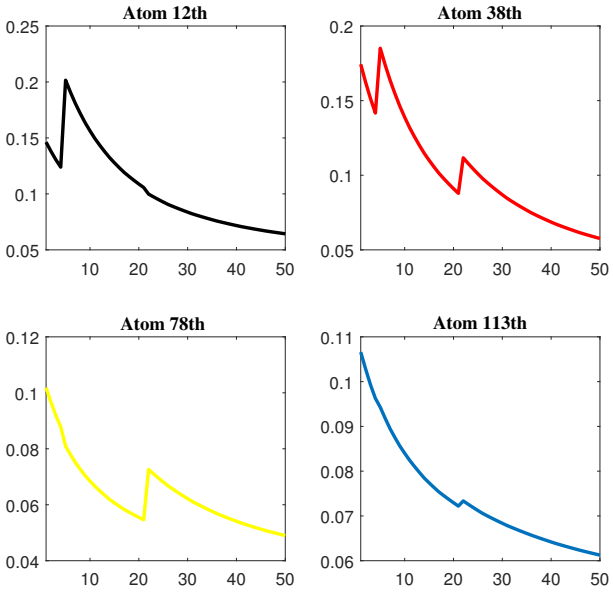


Figure 5.6: Four atoms (the 12th, 38th, 78th and 113th) in the trained dictionary for SER images

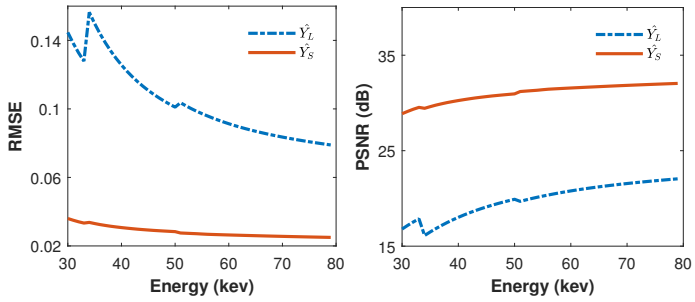


(a) (b)

Figure 5.7: The performance of reconstruction: (a) RMSE; (b) PSNR

The decomposition results of four basis materials are shown in figure 5.8. In contrast to LER, SER-based material decomposition shows much higher detection ability for all the basis materials and is much similar with the ground-truth. Especially, for iodine, LER-based method cannot even separate it from the other three materials, while SER-based method shows much better precision.

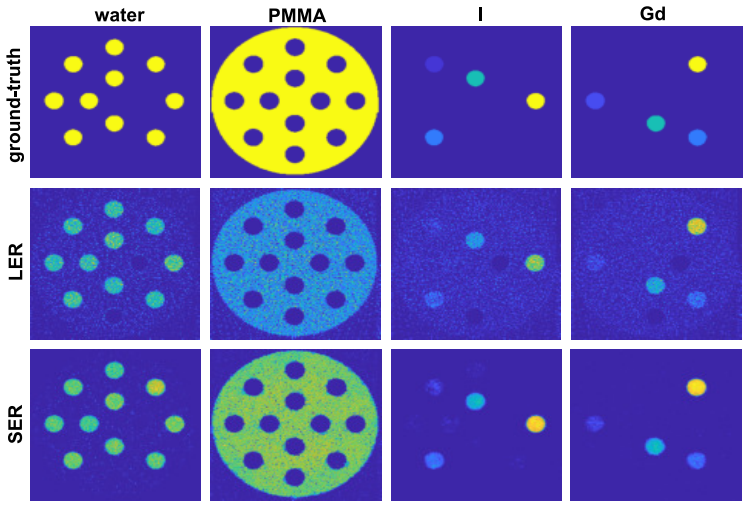


Figure 5.8: The results of material decomposition based on three sCT images. Left to right: ground-truth, theoretical SER, LER and SER images

For more quantitative analysis, we compare the mass density of Fe, I and Gd in the corresponding rows. The results indicate that DSR has good decomposition ability for all of iron, iodine and gadolinium, as shown in figure 5.9. In contrast, L1 yields much lower density of iron and higher density of iodine compared to the theoretical values. As an illustration, we list $error_m$ of water, PMMA, iodine and gadolinium in Table 5.1. Clearly, SER-based method has smaller $error_m$ for all the four basis materials.

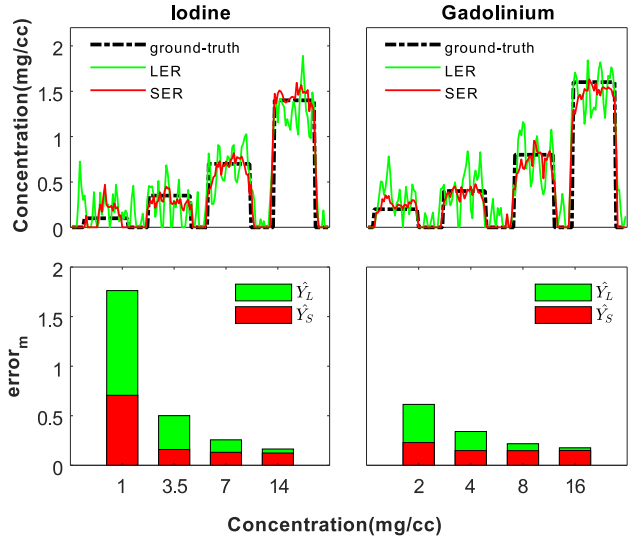


Figure 5.9: The mass densities of iodine, gadolinium and water in corresponding dilution.

Table 5.1: The normalized Euclidean distance $error_m$ of different decomposition methods on digital phantom.

| Materials \ Methods | LER | SER |
|---|---|---|
| water+PMMA | 0.6 | 0.4 |
| Iodine | 0.6 | 0.1 |
| Gadolinium | 0.5 | 0.1 |

### 5.4.2 Physical data

**Physical phantom data generation**

The experiments were performed on physical data from a Philips sCT prototype [Si-Mohamed et al., 2018,Cormode et al., 2017]. Projection data was obtained at tube voltage 120 kVp and current 220 mA. The volumetric CT dose index ($CTDI_{vol}$) was 22.2 mGy. The scan consists of 2400 projections; each projection has 924 parallel rays; each ray contains 5 energy bins. The energy thresholds of sCT are the same for all the physical data in this work: 30, 51, 62, 72, 81 keV.

The performance of the proposed SER based material decomposition method was evaluated on both physical phantoms and in vivo data. The physical phantoms are shown in figure 5.10a, the images of which are the reconstructed gadolinium at one single bin. The upper phantom without a large ring is for training, while the lower one with the large ring for testing. sCT images of phantom with large ring have stronger quantum noise and more artifacts, due to less photons that can pass the phantom and be detected. Removable tubes containing different dilutions of iodine or gadolinium are inserted in the center of phantoms, as shown in figure 5.10b. The number on each disk refers to the concentration (mg/cc) which covers from 0.1 $mg/cc$ to 15 $mg/cc$. In our experiments, both iodine (I) and gadolinium (Gd) were measured for training and testing.

Meanwhile, we use another in vivo dataset to further evaluate the proposed method. Reconstructed images of a rabbit 5 and 15 min after injection of gadolinium are shown in figure 5.11, respectively. The image of 5 min after injection is a little blurred due to movement.

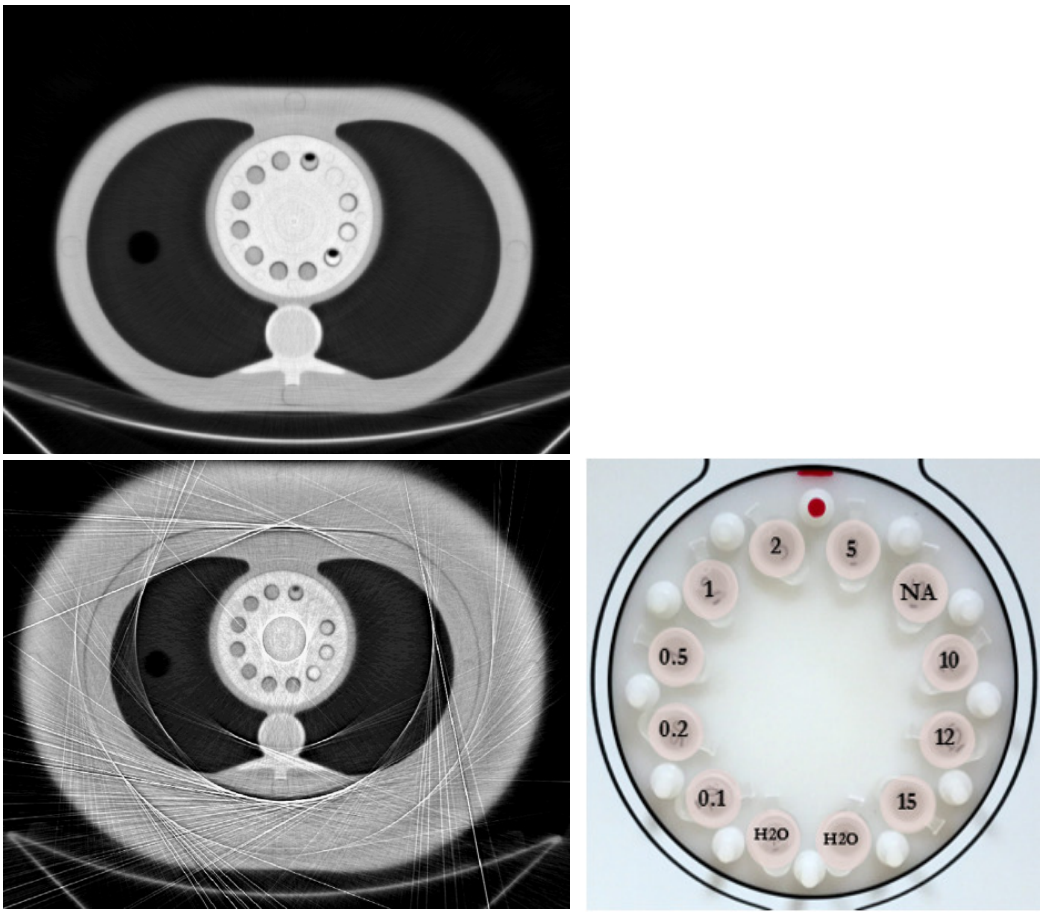


(a) (b)

Figure 5.10: (a) Physical phantoms without (upper) and with (lower) large ring: gadolinium at the 4-th bin; (b) inserts: labels refer to the nominal concentration present in each tube (mg/cc).

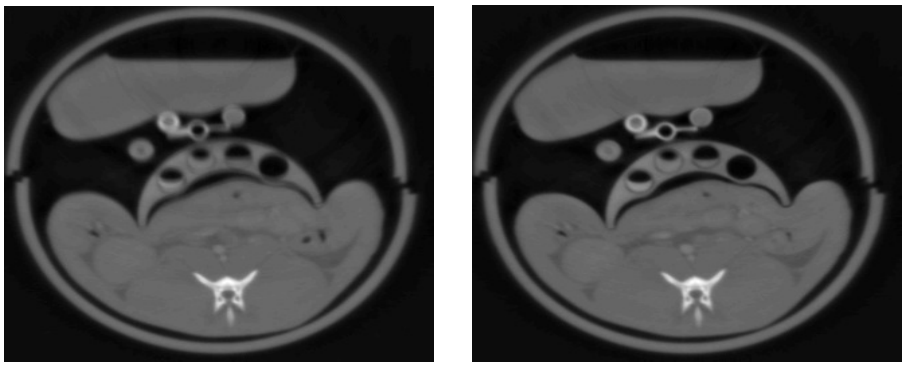

(a) (b)

Figure 5.11: The reconstructed image of in vivo data at the first energy bin: (a) 5 min after injection of gadolinium; (b) 15 min after.

The spatial images of all physical data were separately reconstructed at each energy bin via a common reconstruction method: conjugate gradient method (with Reconstruction Toolkit (RTK) [Rit et al., 2014]). All phantoms were reconstructed into 9 slices and the size of each slice is 900*900. We learned the coupled dictionaries composed of 1024 ($N_D$) atoms from 400K ($N_t$) random LER-SER pixel pairs.

**Training**

NRMSE and PSNR (dB) of synthesized SER images at each energy bin are shown in figure 5.12. SER images of iodine have relatively higher accuracy than gadolinium, *e.g.* smaller NRMSE and higher PSNR, although both of them have good synthesis performance. Note that low-energy bins have relatively larger NRMSE and smaller PSNR, especially for bins of k-edge (*i.e.* energy bins containing k-edge). Also, we need to recover more details at the first two bins: 30 - 50 keV and 51 - 61 keV.

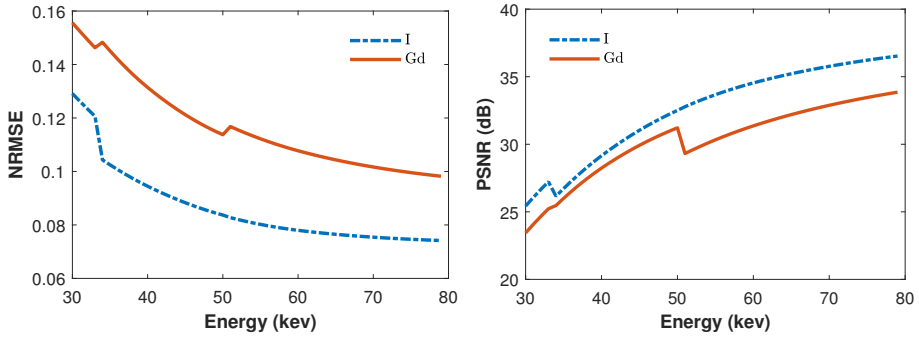


(a) (b)

Figure 5.12: The (a) NRMSE and (b) PSNR of synthesized SER images for iodine and gadolinium.

The material decomposition results of synthesized SER images are shown in figure 5.13. Visually, the proposed SER-based material decomposition method presents good detection ability in terms of edge-preserving performance in training. It can substantially preserve edge information even for low-concentration iodine and gadolinium *e.g.* 0.5 mg/cc, as illustrated in the regions-of-interests (ROIs). Note that all the ROIs are shown with grayscale images in order to highlight morphological information.

To quantitatively assess the decomposition, linear regressions of iodine and gadolinium for all the concentrations are illustrated in figure 5.14. Both iodine and gadolinium have clearly higher accuracy with respect to theoretical concentrations. The correlations between the measured and prepared concentrations are strongly linear for all dilutions (all $R^2 \geq 0.95$). The slopes are close to 1 for both iodine ($a$ = 0.96) and gadolinium ($a$ = 0.97). The y-intercept values are very low, *e.g.* $b$ = -0.26 for iodine and -0.38 for gadolinium. Additionally, the decomposition is very reliable because both iodine and gadolinium are always underestimated and their standard deviations are small.

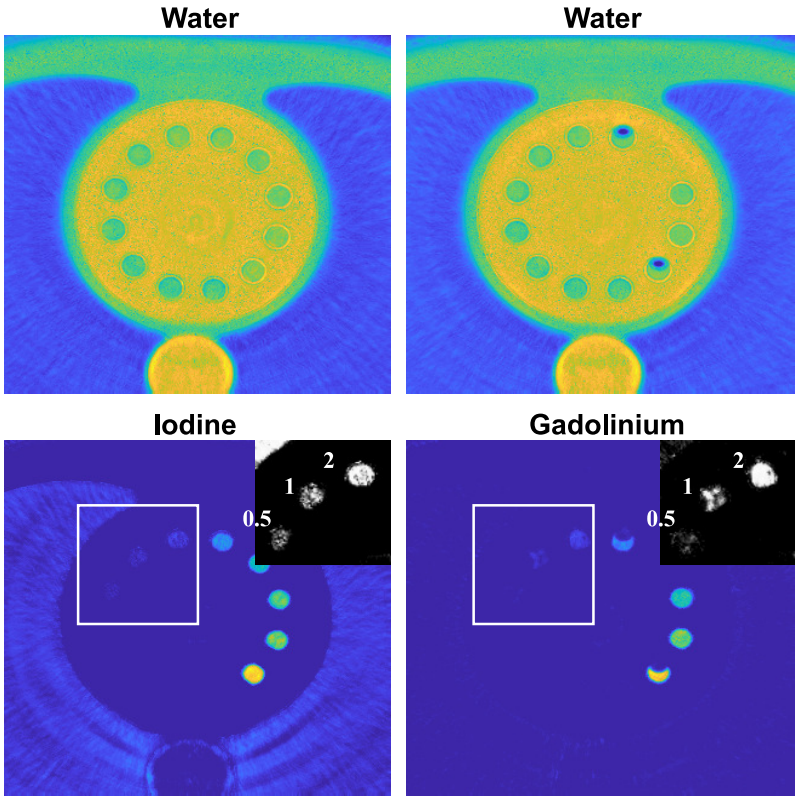


Figure 5.13: The results of SER based material decomposition method on physical phantoms in training. Note that ROIs are shown in grayscale to highlight morphological information. Labels in ROIs refer to the nominal concentration present in each tube (mg/cc).

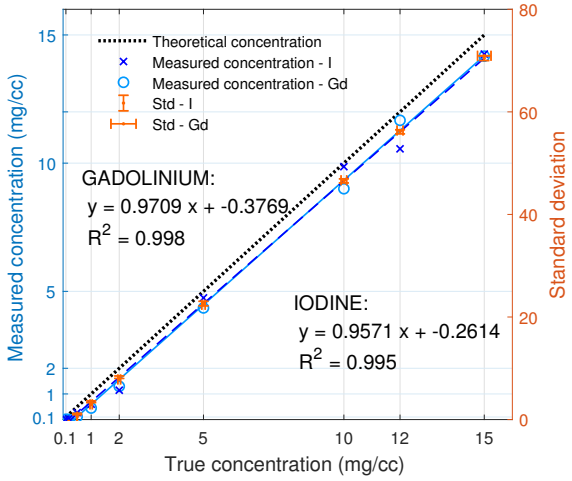


Figure 5.14: The linear regressions of iodine and gadolinium for SER based material decomposition in training: linear regression model, R-squared ($R^2$) and standard deviation (std).

Table 5.2 lists LOD for both iodine and gadolinium, to further assess the detection limit. Both iodine and gadolinium can be detected for concentrations lower than 0.5 mg/cc in training. More specifically, the proposed SER method has better detection ability for iodine than for gadolinium.

Table 5.2: The LOD of different material decomposition methods on physical phantoms.

| | LER | SER | |
|---|---|---|---|
| | | Training | Testing |
| I | 1.28 | 0.34 | 0.56 |
| Gd | 5.70 | 0.45 | 0.84 |

**Testing**

The LER-based material decomposition method using the same lasso regularization was compared to the proposed SER-based method. Both physical phantoms with large ring and in vivo data were tested.

The material decomposition results of physical phantoms with large ring are shown in figure 5.15. In contrast to LER method, the proposed SER method shows better performance in quantification and detection compared to LER method. Firstly, the proposed SER method gives much better morphological accuracy in terms of edge-preserving performance and much less noise, even for low-concentration materials, *e.g.* 0.5 mg/cc for both iodine and gadolinium. The edges are substantially preserved by SER method. While for LER method, the selected areas of low-concentration materials are overwhelmed by noise and cannot be detected.

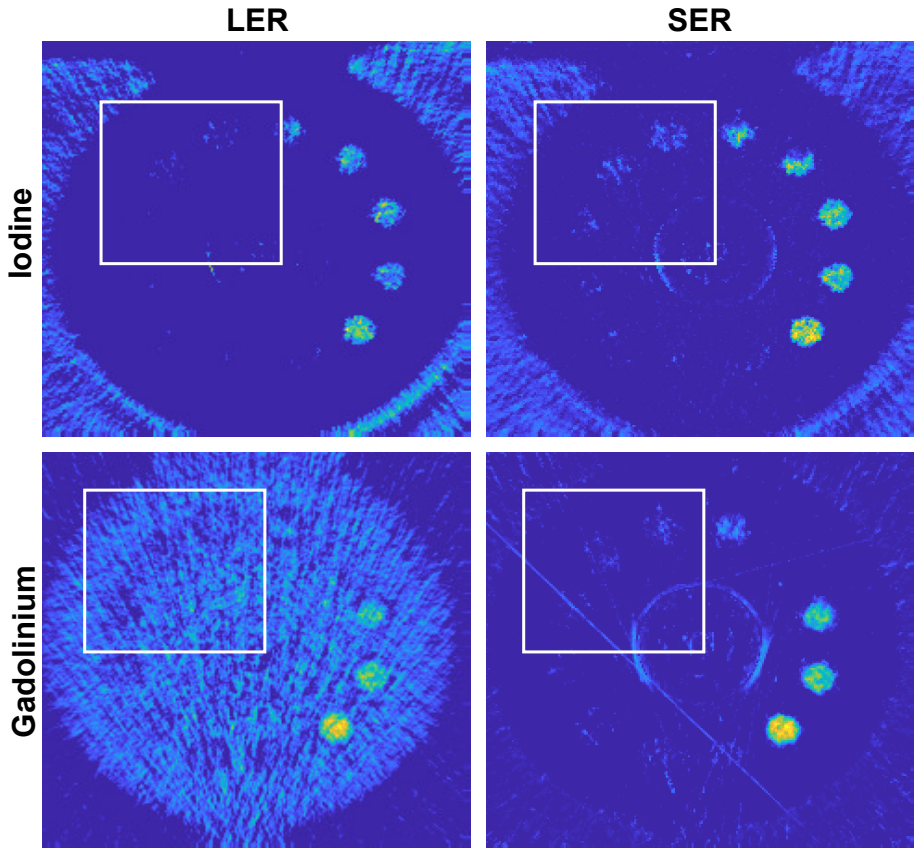


(a)

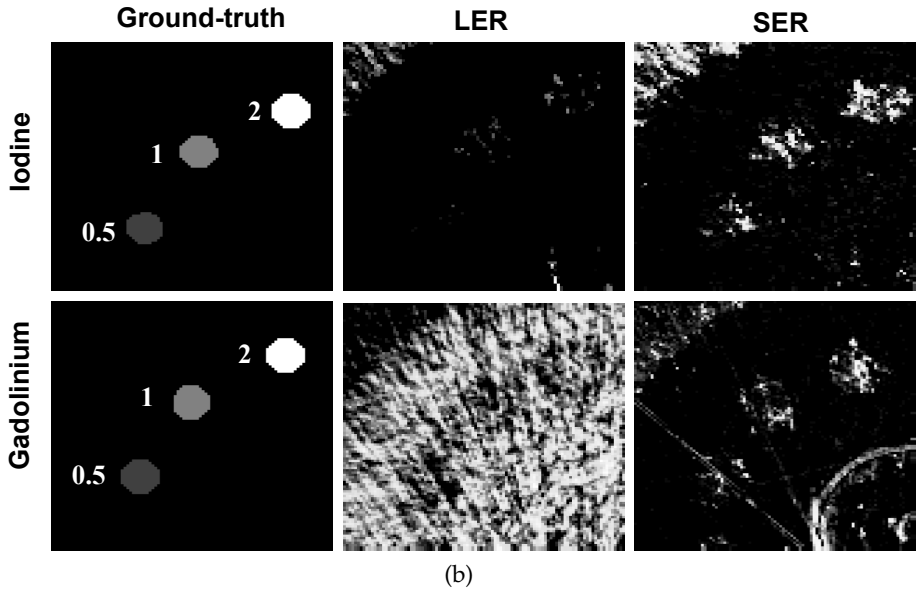


(b)

Figure 5.15: (a) The results of different material decomposition methods on physical phantoms in testing; (b) the ROIs in (a) for low-concentration materials. Labels in ROIs refer to the nominal concentration present in each tube (mg/cc).

Secondly, more quantitatively as shown in figure 5.16, linear regressions of both I and Gd illustrate that SER-based method has much smaller errors. SER method has more precise slope (for iodine: $a_{\mathrm{LER}} = 0.71$ and $a_{\mathrm{SER}} = 0.87$; for gadolinium: $a_{\mathrm{LER}} = 1.24$ and $a_{\mathrm{SER}} = 0.94$) and y-intercept value (for iodine: $b_{\mathrm{LER}} = 1.71$ and $b_{\mathrm{SER}} = -0.08$; for gadolinium: $b_{\mathrm{LER}} = 0.92$ and $b_{\mathrm{SER}} = -0.51$). Meanwhile, SER method is more reliable with smaller standard deviations and almost all decomposed values are always underestimated. As can be observed in Table 5.2 that lists LOD values of different methods for both iodine and gadolinium, our SER method has much stronger detection ability for both iodine and gadolinium compared to LER method by producing the smaller LOD values in testing. It has better detection ability for iodine than for gadolinium, which represents the same results as in training.

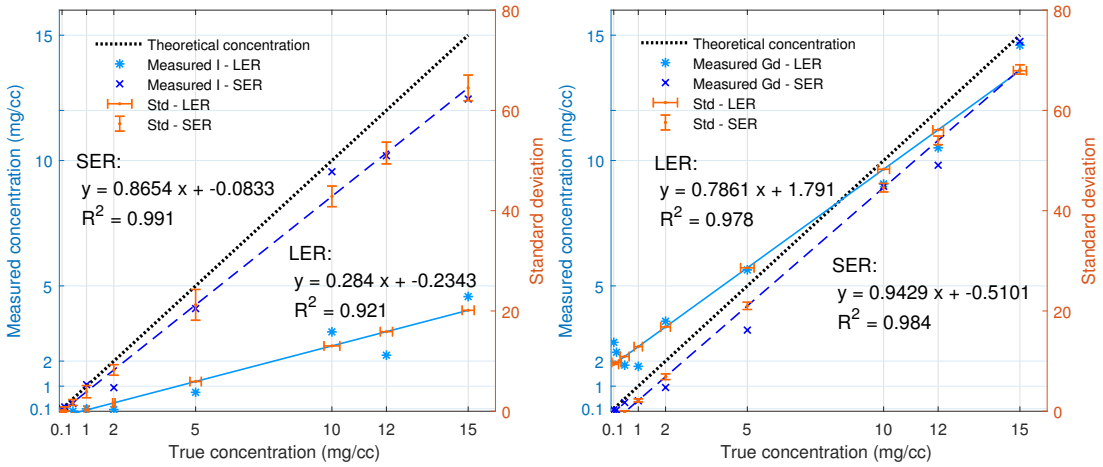


Figure 5.16: The linear regressions of (a) iodine and (b) gadolinium for different material decomposition methods in testing: linear regression model, R-squared ($R^2$) and standard deviation (std).

Meanwhile, the decomposition results of different methods on in vivo data are shown in figure 5.17. Calcium (Ca) in the spine is decomposed on the basis material iodine, due to their similarity of mass attenuation coefficients in our energy thresholds setting. For gadolinium, although the ground-truth is unknown in the in vivo data, tubes of gadolinium dilutions nearby the rabbit were evaluated alternatively. Obviously, LER method cannot separate gadolinium from iodine and has more noise for both iodine and gadolinium. On the contrary, the proposed SER method has better detection ability for both iodine (in the spine) and gadolinium (in tubes and organs). Mean and standard deviation of gadolinium in the tubes are listed in Table 5.3. Obviously, the SER method leads to more accurate decomposition for gadolinium of concentrations covering from 10 mg/cc to 2 mg/cc.

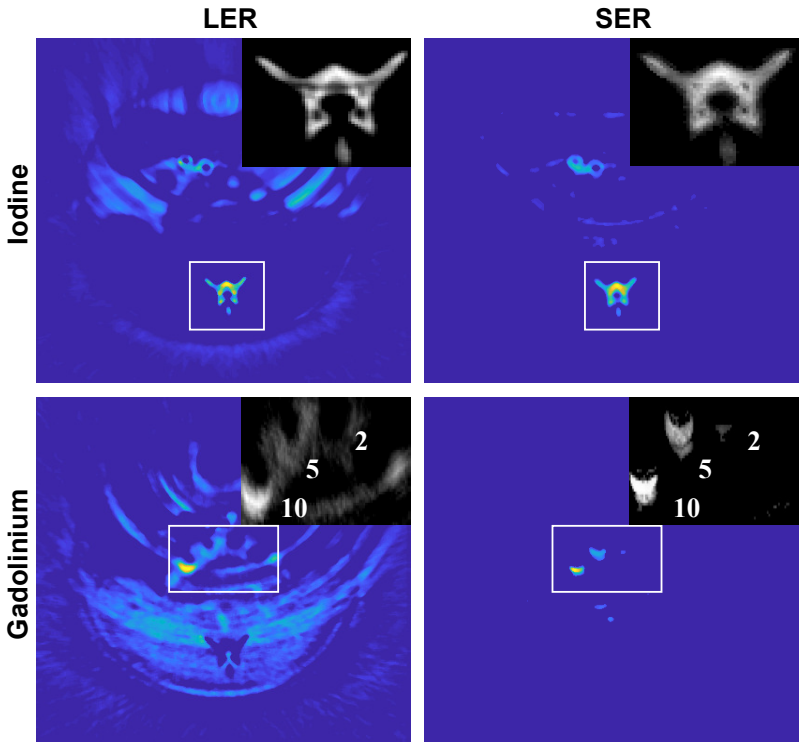


(a)

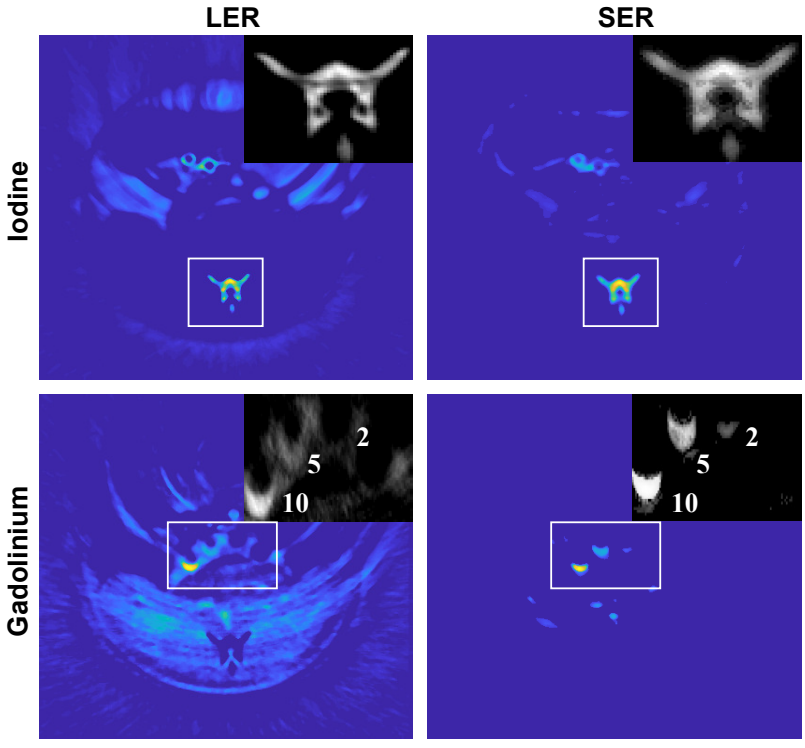


(b)

Figure 5.17: The results of different material decomposition methods on in vivo data in testing: (a) 5 min after the injection of contrast agents; (b) 15 min after. Note that calcium in spine is decomposed on the basis material 'iodine', and the basis material gadolinium exists in tubes and organs.

Table 5.3: The mean and standard deviation (std) of each tube on in vivo data (15 min after injection of gadolinium).

| | LER | SER |
|---|---|---|
| True Conc. (mg/cc) | mean+std | |
| 10 | 6.8 + 0.7 | 10.0+ 1.8 |
| 5 | 2.5 + 0.5 | 4.4 + 0.5 |
| 2 | 0.8 + 0.4 | 1.9 + 0.3 |

## 5.5 Discussion and conclusion

Our main goal is to improve the energy resolution of sCT in order to improve the decomposition accuracy and detection ability. To realize it, we have proposed a SER imaging by fully exploiting abundant spectral features embedded in both simulation and physical data. Preliminary results revealed that the proposed SER method enables accurate decomposition and high detection ability even for low-concentration materials.

The SER-based material decomposition method is reliable. Firstly, even for noisier conditions with respect to training, the proposed SER method enables high decomposition accuracy and detection ability. In our experiments, we trained the dictionaries on the phantoms without large ring, but tested on the ones with large ring which have more noise and artifacts. However, the results still show better decomposition accuracy and detection ability of the proposed method compared to the LER method, especially for iodine. Secondly, accurate decomposition of in vivo data polluted by movement (5 min after the injection) also shows the reliability of our method. Moreover, the decomposition results of both iodine and gadolinium are always underestimated for almost all concentrations.

Each single synthesized SER image is a virtual monochromatic image. Actually, for dual-energy CT, there is a similar but different imaging method called virtual monochromatic image (mono-E or VMS) [Iyama et al., 2018, Matsumoto et al., 2011], which aims to enhance the visibility of contrast agent. A mono-E image is generally reconstructed from a pair of decomposed basis material images (*e.g.* a soft-tissue-like basis material and a contrast agent) in dual-energy CT [Wu et al., 2016, McCollough et al., 2015]. The performance of mono-E is determined by the material decomposition that is processed only on actual images (LER images in the present study). In contrast, SER images are directly synthesized using spectral features learned from both simulation and physical data. As a result, our method can be regarded as a new but more accurate mono-E imaging.

In conclusion, we have proposed a SER imaging to improve the energy resolution of sCT. This is achieved through learning a mapping between simulation and physical data in a pixel-wise way and applying it to other physical data. The results on both physical phantoms and in vivo data showed that the SER-based material decomposition method presents clearly higher accurate material decomposition and detection ability compared to the LER-based method. In the future work, the performance of other image-domain decomposition methods using SER images will be investigated.

# Conclusions and Perspectives

## Conclusions

In this thesis, we have studied the quantitative material decomposition methods for spectral photon-counting CT. As mentioned in General Introduction, our main contribution is that we have proposed three image-domain material decomposition methods: (1) Material Decomposition in X-ray Spectral CT Using Multiple Constraints in Image Domain; (2) ROI-Wise Material Decomposition in Spectral Photon-Counting CT; (3) Super-Energy-Resolution Material Decomposition in Spectral Photon-Counting CT Using Pixel-wise Learning.

Before presenting the achievements of the present thesis work, the basic principles of spectral CT have been reviewed in Chapter 1, including spectral CT imaging system, reconstruction methods and applications. Then, the model of material decomposition and mathematical foundations of solving the decomposition are discussed in detail.

Acquainted with the general principles of spectral CT and knowledge of material decomposition, we set up the present work following the above-mentioned three aspects:

(1) Material Decomposition in X-ray Spectral CT Using Multiple Constraints in Image Domain (Chapter 3).

We have proposed a material decomposition method for spectral CT by simultaneously exploiting the limited value of mass density, the multi-dimensional nature and high correlation of multi-energy data and the local property of neighboring pixels. To get rid of the difficulties due to similarities among basis materials, spectral and spatial redundancies are eliminated through using joint sparsity and structural low-rank. At the same time, we also add bound constraint on mass density, which is naturally true in practical applications. The results of both simulation and physical experiments revealed that the proposed DSR method has a good material decomposition ability even for very poorly conditioned problems.

(2) ROI-Wise Material Decomposition in Spectral Photon-Counting CT (Chapter 4).

We have proposed a ROI-wise material decomposition method for sCT by jointly optimizing basis materials and reducing noise. This is achieved through spatio-energy segmentation and exploiting both morphological and spectral information in the sCT images. The results on digital and physical data showed that the ROI-wise material decomposition method presents clearly higher accuracy and reliability compared to common decomposition methods based on TV or *lasso* regularization.

(3) Super-Energy-Resolution Material Decomposition in Spectral Photon-Counting CT Using Pixel-wise Learning (Chapter 5).

We have proposed a SER imaging to improve the energy resolution of sCT. This is achieved through learning a mapping between simulation and physical data in a pixel-wise way and applying it to other physical data. The results on both digital and physical data showed that the SER-based material decomposition method presents clearly higher accurate material decomposition and detection ability compared to the LER based method.

## Perspectives

With respect to the proposed material decomposition methods for spectral photon-counting CT, several potential improvements can be carried out in the future:

(1) Material Decomposition in X-ray Spectral CT Using Multiple Constraints in Image Domain. The collaborative joint sparsity and structural low-rank should be further investigated to make full use of sparsity and low-rank property hidden in the spectral CT data. Meanwhile, a more robust strategy for the choice of regularization parameters could also be investigated.

(2) ROI-Wise Material Decomposition in Spectral Photon-Counting CT. The ability of detecting low-concentration materials may further be investigated to improve the sensitivity of the method while maintaining reliability. What's more, the ability of identifying small structures having small material concentration could also be investigated.

(3) Super-Energy-Resolution Material Decomposition in Spectral Photon-Counting CT Using Pixel-wise Learning. The performance of other image-domain decomposition methods using SER images may be investigated.

## Author's publications

**Journal papers:**

- **Bingqing Xie**, Ting Su, Valérie Kaftandjian, Pei Niu, Feng Yang, Marc Robini, Yuemin Zhu, Philippe Duvauchelle. "Material Decomposition in X-ray Spectral CT Using Multiple Constraints in Image Domain." (2019). Journal of Nondestructive Evaluation, 38(1):16.
- **Bingqing Xie**, Pei Niu, Ting Su, Valérie Kaftandjian, Loic Boussel, Philippe Douek, Feng Yang, Yuemin Zhu, Philippe Duvauchelle. "Material Decomposition in X-ray Spectral CT Using Multiple Constraints in Image Domain.". IEEE Transaction on Nuclear Science. (in revision)
- **Bingqing Xie**, Valérie Kaftandjian, Pei Niu, Ting Su, Loic Boussel, Philippe Douek, Feng Yang, Yuemin Zhu, Philippe Duvauchelle. "Super-Energy-Resolution Material Decomposition in Spectral Photon-Counting CT Using Pixel-Wise Learning.". IEEE Transaction on Medical Imaging. (to be submitted soon)
- Pei Niu, Marc Robini, **Bingqing Xie**, Ting Su, Valérie Kaftandjian, Feng Yang, Lihui Wang,Loic Boussel, Philippe Douek, Yuemin Zhu. "Simultaneous Multimodal Imaging Using Spectral Photon-Counting CT: a Simulation Study", IEEE Transactions on Biomedical Engineering (under review).

**Conference papers:**

- **B. Xie**, T. Su, V. Kaftandjian, P. Duvauchelle, P. Niu, M. Robini, and Y. Zhu. "Image Domain Local Joint Sparse Material Decomposition in Spectral CT." 8th Conference on Industrial Computed Tomography (iCT 2018), Wels, Austria, Feb 2018.
- P. Niu, M. Robini, **B. Xie**, T. Su, V. Kaftandjian, F. Yang, Y. Zhu, and P. Duvauchelle, "Simultaneous reconstruction and denoising of spectral CT images," in International Conference on Signal Processing Proceedings, ICSP, 2019.

# Bibliography

[Alessio and MacDonald, 2013] Alessio, A. M. and MacDonald, L. R. (2013). Quantitative material characterization from multi-energy photon counting CT. *Medical physics*, 40(3):031108.

[Alvarez and Macovski, 1976] Alvarez, R. E. and Macovski, A. (1976). Energy-selective reconstructions in X-ray computerised tomography. *Physics in Medicine and Biology*, 21(5):002.

[Andersen and Kak, 1984] Andersen, A. H. and Kak, A. C. (1984). Simultaneous Algebraic Reconstruction Technique (SART): A Superior Implementation of the Art Algorithm. *Ultrasonic Imaging*, 6(1):81–94.

[Beister et al., 2012] Beister, M., Kolditz, D., and Kalender, W. A. (2012). Iterative reconstruction methods in X-ray CT. *Physica Medica*, 28(2):94–108.

[Berglund et al., 2014] Berglund, J., Johansson, H., Lundqvist, M., Cederström, B., and Fredenberg, E. (2014). Energy weighting improves dose efficiency in clinical practice: implementation on a spectral photon-counting mammography system. *Journal of Medical Imaging*, 1(3):031003.

[Boyd et al., 2010] Boyd, S., Parikh, N., Chu, E., Peleato, B., and Eckstein, J. (2010). Distributed Optimization and Statistical Learning via the Alternating Direction Method of Multipliers. *Foundations and Trends® in Machine Learning*, 3(1):1–122.

[Cai et al., 2013] Cai, C., Rodet, T., Legoupil, S., and Mohammad-Djafari, A. (2013). A full-spectral Bayesian reconstruction approach based on the material decomposition model applied in dual-energy computed tomography. *Med. Phys.*, 40(11):111916.

[Cai et al., 2010] Cai, J.-F., Candès, E. J., and Shen, Z. (2010). A Singular Value Thresholding Algorithm for Matrix Completion. *SIAM Journal on Optimization*, 20(4):1956–1982.

[Candes et al., 2006] Candes, E., Romberg, J., and Tao, T. (2006). Robust uncertainty principles: exact signal reconstruction from highly incomplete frequency information. *IEEE Transactions on Information Theory*, 52(2):489–509.

[Candès et al., 2011] Candès, E. J., Li, X., Ma, Y., and Wright, J. (2011). Robust principal component analysis? *Journal of the ACM*, 58(3):1–37.

[Carramate et al., 2011] Carramate, L. F. N. D., Oliveira, C. A. B., Silva, A. L. M., da Silva, A. M., dos Santos, J. M. F., and Veloso, J. F. C. A. (2011). Energy weighting technique in Quantum Computed Tomography using a MPGD. *Journal of Instrumentation*, 6(02):C02002–C02002.

[Chandarana et al., 2011] Chandarana, H., Megibow, A. J., Cohen, B. A., Srinivasan, R., Kim, D., Leidecker, C., and Macari, M. (2011). Iodine quantification with dual-energy CT: Phantom study and preliminary experience with renal masses. *American Journal of Roentgenology*, 196(6):693–700.

[Chen et al., 2008] Chen, G.-H., Tang, J., and Leng, S. (2008). Prior image constrained compressed sensing (PICCS): A method to accurately reconstruct dynamic CT images from highly undersampled projection data sets. *Medical Physics*, 35(2):660–663.

[Clark and Badea, 2014] Clark, D. P. and Badea, C. T. (2014). Spectral diffusion: an algorithm for robust material decomposition of spectral CT data. *Physics in Medicine and Biology*, 59(21):6445–6466.

[Cormode et al., 2010] Cormode, D. P., Roessl, E., Thran, A., Skajaa, T., Gordon, R. E., Schlomka, J.-P., Fuster, V., Fisher, E. A., Mulder, W. J. M., Proksa, R., and Fayad, Z. A. (2010). Atherosclerotic Plaque Composition: Analysis with Multicolor CT and Targeted Gold Nanoparticles. *Radiology*, 256(3):774–782.

[Cormode et al., 2017] Cormode, D. P., Si-Mohamed, S., Bar-Ness, D., Sigovan, M., Naha, P. C., Balegamire, J., Lavenne, F., Coulon, P., Roessl, E., Bartels, M., Rokni, M., Blevis, I., Boussel, L., and Douek, P. (2017). Multicolor spectral photon-counting computed tomography: in vivo dual contrast imaging with a high count rate scanner. *Scientific Reports*, 7(1):4784.

[Dhillon et al., 2004] Dhillon, I. S., Guan, Y., and Kulis, B. (2004). Kernel k-means. In *Proceedings of the 2004 ACM SIGKDD international conference on Knowledge discovery and data mining - KDD '04*, page 551, New York, New York, USA. ACM Press.

[Ding et al., 2018] Ding, Q., Niu, T., Zhang, X., and Long, Y. (2018). Image-domain multimaterial decomposition for dual-energy CT based on prior information of material images. *Medical Physics*, 45(8):3614–3626.

[Donoho, 2006] Donoho, D. (2006). Compressed sensing. *IEEE Transactions on Information Theory*, 52(4):1289–1306.

[Ducros et al., 2017] Ducros, N., Abascal, J. F. P.-J., Sixou, B., Rit, S., and Peyrin, F. (2017). Regularization of nonlinear decomposition of spectral x-ray projection images. *Medical Physics*, 44(9):e174–e187.

[Duvauchelle et al., 2000] Duvauchelle, P., Freud, N., Kaftandjian, V., and Babot, D. (2000). Computer code to simulate X-ray imaging techniques. *Nuclear Instruments and Methods in Physics Research, Section B: Beam Interactions with Materials and Atoms*, 170(1):245–258.

[Elbakri and Fessler, 2002] Elbakri, I. and Fessler, J. (2002). Statistical image reconstruction for polyenergetic X-ray computed tomography. *IEEE Transactions on Medical Imaging*, 21(2):89–99.

[Faby et al., 2015] Faby, S., Kuchenbecker, S., Sawall, S., Simons, D., Schlemmer, H.-P., Lell, M., and Kachelrieß, M. (2015). Performance of today's dual energy CT and future multi energy CT in virtual non-contrast imaging and in iodine quantification: A simulation study. *Medical Physics*, 42(7):4349–4366.

[Faby et al., 2014] Faby, S., Kuchenbecker, S., Simons, D., Schlemmer, H.-P., Lell, M., and Kachelrieß, M. (2014). CT calibration and dose minimization in image-based material decomposition with energy-selective detectors. *Proceedings of SPIE Medical Imaging*, 9033(6221):903318.

[Fadili et al., 2010] Fadili, M. J., Starck, J.-L., Bobin, J., and Moudden, Y. (2010). Image Decomposition and Separation Using Sparse Representations: An Overview. *Proceedings of the IEEE*, 98(6):983–994.

[Fauvel et al., 2012] Fauvel, M., Chanussot, J., and Benediktsson, J. (2012). A spatial–spectral kernel-based approach for the classification of remote-sensing images. *Pattern Recognition*, 45(1):381–392.

[Feuerlein et al., 2008] Feuerlein, S., Roessl, E., Proksa, R., Martens, G., Klass, O., Jeltsch, M., Rasche, V., Brambs, H.-J., Hoffmann, M. H. K., and Schlomka, J.-P. (2008). Multienergy Photon-counting K-edge Imaging: Potential for Improved Luminal Depiction in Vascular Imaging. *Radiology*, 249(3):1010–1016.

[Foygel Barber et al., 2016] Foygel Barber, R., Sidky, E. Y., Gilat Schmidt, T., and Pan, X. (2016). An algorithm for constrained one-step inversion of spectral CT data. *Physics in Medicine and Biology*, 61(10):3784–3818.

[Gao et al., 2011] Gao, H., Yu, H., Osher, S., and Wang, G. (2011). Multi-energy CT based on a prior rank, intensity and sparsity model (PRISM). *Inverse Problems*, 27(11):115012.

[Giersch et al., 2004] Giersch, J., Niederlöhner, D., and Anton, G. (2004). The influence of energy weighting on X-ray imaging quality. *Nuclear Instruments and Methods in Physics Research Section A: Accelerators, Spectrometers, Detectors and Associated Equipment*, 531(1-2):68–74.

[Gilbert, 1972] Gilbert, P. (1972). Iterative methods for the three-dimensional reconstruction of an object from projections. *Journal of Theoretical Biology*, 36(1):105–117.

[Gordon et al., 1970] Gordon, R., Bender, R., and Herman, G. T. (1970). Algebraic Reconstruction Techniques (ART) for three-dimensional electron microscopy and X-ray photography. *Journal of Theoretical Biology*, 29(3):471–481.

[Heismann, Björn J., Bernhard T. Schmidt and Flohr., 2012] Heismann, Björn J., Bernhard T. Schmidt and Flohr., T. (2012). *Spectral computed tomography*. SPIE Bellingham, WA.

[Holt, 2014] Holt, K. M. (2014). Total Nuclear Variation and Jacobian Extensions of Total Variation for Vector Fields. *IEEE Transactions on Image Processing*, 23(9):3975–3989.

[Hou et al., 2018] Hou, X., Teng, Y., Kang, Y., and Qi, S. (2018). A separable quadratic surrogate total variation minimization algorithm for accelerating accurate CT reconstruction from few-views and limited-angle data. *Medical Physics*, 45(2):535–548.

[Hu et al., 2018] Hu, X., Heide, F., Dai, Q., and Wetzstein, G. (2018). Convolutional Sparse Coding for RGB+NIR Imaging. *IEEE Transactions on Image Processing*, 27(4):1611–1625.

[Iwanczyk et al., 2009] Iwanczyk, J. S., Nygard, E., Meirav, O., Arenson, J., Barber, W. C., Hartsough, N. E., Malakhov, N., and Wessel, J. C. (2009). Photon Counting Energy Dispersive Detector Arrays for X-ray Imaging. *IEEE Transactions on Nuclear Science*, 56(3):535–542.

[Iyama et al., 2018] Iyama, Y., Nakaura, T., Iyama, A., Katahira, K., and Yamashita, Y. (2018). The Usefulness of Dual-Layer Spectral Computed Tomography for Myelography: A Case Report and Review of the Literature. *Case Reports in Orthopedics*, 2018:1–4.

[Jacobsen et al., 2019] Jacobsen, M. C., Cressman, E. N. K., Tamm, E. P., Baluya, D. L., Duan, X., Cody, D. D., Schellingerhout, D., and Layman, R. R. (2019). Dual-Energy CT: Lower Limits of Iodine Detection and Quantification. *Radiology*, 292(2):414–419.

[Jiao et al., 2016] Jiao, Y., Jin, Q., Lu, X., and Wang, W. (2016). Alternating Direction Method of Multipliers for Linear Inverse Problems. *SIAM Journal on Numerical Analysis*, 54(4):2114–2137.

[KACZMARZ, 1993] KACZMARZ, S. (1993). Approximate solution of systems of linear equations†. *International Journal of Control*, 57(6):1269–1271.

[Kalender et al., 1988] Kalender, W., Klotz, E., and Kostaridou, L. (1988). An algorithm for noise suppression in dual energy CT material density images. *IEEE Transactions on Medical Imaging*, 7(3):218–224.

[Kowalski et al., 2009] Kowalski, M., Kowalski, M., Regression, S., Mixed, U., Applied, N., and Kowalski, M. (2009). Sparse Regression Using Mixed Norms To cite this version : Sparse Regression Using Mixed Norms. 27(3):303–324.

[LaRoque et al., 2008] LaRoque, S. J., Sidky, E. Y., and Pan, X. (2008). Accurate image reconstruction from few-view and limited-angle data in diffraction tomography. *Journal of the Optical Society of America A*, 25(7):1772.

[Le and Molloi, 2011] Le, H. Q. and Molloi, S. (2011). Least squares parameter estimation methods for material decomposition with energy discriminating detectors. *Medical Physics*, 38(1):245–255.

[Le Huy and Molloi, 2011] Le Huy, Q. and Molloi, S. (2011). Least squares parameter estimation methods for material decomposition with energy discriminating detectors. *Medical physics*, 38(1):245–55.

[Lee et al., 2016a] Lee, D., Kim, Y.-s., Choi, S., Lee, H., Choi, S., and Kim, H.-J. (2016a). Anatomical decomposition in dual energy chest digital tomosynthesis. page 978367.

[Lee et al., 2016b] Lee, W.-J., Kang, S.-R., Choi, S.-C., Lee, S.-S., Heo, M.-S., Huh, K.-H., and Yi, W.-J. (2016b). Material decomposition with the multi-energy attenuation coefficient ratio by using a multiple discriminant analysis. *Journal of the Korean Physical Society*, 69(2):231–240.

[Leng et al., 2011] Leng, S., Yu, L., Wang, J., Fletcher, J. G., Mistretta, C. A., and McCollough, C. H. (2011). Noise reduction in spectral CT: Reducing dose and breaking the trade-off between image noise and energy bin selection. *Medical Physics*, 38(9):4946–4957.

[Li et al., 2017] Li, Z., Leng, S., Yu, L., Manduca, A., McCollough, C. H., Buades, A., Coll, B., and Morel, J. M. (2017). An effective noise reduction method for multi-energy CT images that exploit spatio-spectral features. *Medical Physics*, 44(5):1610–1623.

[Li et al., 2015] Li, Z., Leng, S., Yu, L., Yu, Z., and McCollough, C. H. (2015). Image-based Material Decomposition with a General Volume Constraint for Photon-Counting CT. *Proceedings of SPIE–the International Society for Optical Engineering*, 9412.

[Liu et al., 2016] Liu, J., Ding, H., Molloi, S., Zhang, X., and Gao, H. (2016). TICMR: Total Image Constrained Material Reconstruction via Nonlocal Total Variation Regularization for Spectral CT. *IEEE Transactions on Medical Imaging*, 35(12):2578–2586.

[Long and Fessler, 2014] Long, Y. and Fessler, J. A. (2014). Multi-Material Decomposition Using Statistical Image Reconstruction for Spectral CT. *IEEE Transactions on Medical Imaging*, 33(8):1614–1626.

[Macovski et al., 1976] Macovski, A., Alvarez, R., Chan, J.-H., Stonestrom, J., and Zatz, L. (1976). Energy dependent reconstruction in X-ray computerized tomography. *Computers in Biology and Medicine*, 6(4):325–336.

[Mail et al., 2008] Mail, N., Moseley, D. J., Siewerdsen, J. H., and Jaffray, D. A. (2008). The influence of bowtie filtration on cone-beam CT image quality. *Medical Physics*, 36(1):22–32.

[Matsumoto et al., 2011] Matsumoto, K., Jinzaki, M., Tanami, Y., Ueno, A., Yamada, M., and Kuribayashi, S. (2011). Virtual Monochromatic Spectral Imaging with Fast Kilovoltage Switching: Improved Image Quality as Compared with That Obtained with Conventional 120-kVp CT. *Radiology*, 259(1):257–262.

[McCollough et al., 2015] McCollough, C. H., Leng, S., Yu, L., and Fletcher, J. G. (2015). Dual- and Multi-Energy CT: Principles, Technical Approaches, and Clinical Applications. *Radiology*, 276(3):637–653.

[McLachlan and Krishnan, 2008] McLachlan, G. J. and Krishnan, T. T. (2008). *The EM algorithm and extensions*. Wiley-Interscience.

[Mechlem et al., 2018] Mechlem, K., Ehn, S., Sellerer, T., Braig, E., Munzel, D., Pfeiffer, F., and Noel, P. B. (2018). Joint Statistical Iterative Material Image Reconstruction for Spectral Computed Tomography Using a Semi-Empirical Forward Model. *IEEE Transactions on Medical Imaging*, 37(1):68–80.

[Mendonca et al., 2014] Mendonca, P. R., Lamb, P., and Sahani, D. V. (2014). A flexible method for multi-material decomposition of dual-energy CT images. *IEEE Transactions on Medical Imaging*, 33(1):99–116.

[Moretti et al., 2011] Moretti, M., Sisti, D., Rocchi, M. B., and Delprete, E. (2011). CLSI EP17-A protocol: A useful tool for better understanding the low end performance of total prostate-specific antigen assays. *Clinica Chimica Acta*, 412(11-12):1143–1145.

[Neuhaus et al., 2017] Neuhaus, V., Abdullayev, N., Große Hokamp, N., Pahn, G., Kabbasch, C., Mpotsaris, A., Maintz, D., and Borggrefe, J. (2017). Improvement of Image Quality in Unenhanced Dual-Layer CT of the Head Using Virtual Monoenergetic Images Compared With Polyenergetic Single-Energy CT. *Investigative Radiology*, 52(8):470–476.

[Nie et al., 2010] Nie, F., Huang, H., Cai, X., and Ding, C. H. (2010). Efficient and robust feature selection via joint L2, 1-norms minimization. In *Advances in Neural Information Processing Systems*, volume 23, pages 1813–1821.

[Pan et al., 2010] Pan, D., Roessl, E., Schlomka, J. P., Caruthers, S. D., Senpan, A., Scott, M. J., Allen, J. S., Zhang, H., Hu, G., Gaffney, P. J., Choi, E. T., Rasche, V., Wickline, S. A., Proksa, R., and Lanza, G. M. (2010). Computed tomography in color: Nanok-enhanced spectral CT molecular imaging. *Angewandte Chemie - International Edition*, 49(50):9635–9639.

[Pan et al., 2014] Pan, D., Schirra, C. O., Wickline, S. A., and Lanza, G. M. (2014). Multicolor computed tomographic molecular imaging with noncrystalline high-metal-density nanobeacons. *Contrast Media and Molecular Imaging*, 9(1):13–25.

[Pan and Yang, 2010] Pan, S. J. and Yang, Q. (2010). A Survey on Transfer Learning. *IEEE Transactions on Knowledge and Data Engineering*, 22(10):1345–1359.

[Panta et al., 2015] Panta, R. K., Walsh, M. F., Bell, S. T., Anderson, N. G., Butler, A. P., and Butler, P. H. (2015). Energy Calibration of the Pixels of Spectral X-ray Detectors. *IEEE Transactions on Medical Imaging*, 34(3):697–706.

[Quon et al., 2015] Quon, J. S., Moosavi, B., Khanna, M., Flood, T. A., Lim, C. S., and Schieda, N. (2015). False positive and false negative diagnoses of prostate cancer at multi-parametric prostate MRI in active surveillance. *Insights into Imaging*, 6(4):449–463.

[Rao and Kreutz-Delgado, 1999] Rao, B. and Kreutz-Delgado, K. (1999). An affine scaling methodology for best basis selection. *IEEE Transactions on Signal Processing*, 47(1):187–200.

[Rit et al., 2014] Rit, S., Vila Oliva, M., Brousmiche, S., Labarbe, R., Sarrut, D., and Sharp, G. C. (2014). The Reconstruction Toolkit (RTK), an open-source cone-beam CT reconstruction toolkit based on the Insight Toolkit (ITK). *Journal of Physics: Conference Series*, 489(1).

[Roessl and Proksa, 2007] Roessl, E. and Proksa, R. (2007). K-edge imaging in x-ray computed tomography using multi-bin photon counting detectors. *Physics in Medicine and Biology*, 52(15):4679–4696.

[Rudin et al., 1992] Rudin, L. I., Osher, S., and Fatemi, E. (1992). Nonlinear total variation based noise removal algorithms. *Physica D: Nonlinear Phenomena*, 60(1-4):259–268.

[Saloman and Hubbell, 1986] Saloman, E. and Hubbell, J. (1986). X-ray attenuation coefficients (total cross sections): Comparison of the experimental data base with the recommended values of Henke and the theoretical values of Scofield for energies between 0. 1-100 keV. Technical report.

[Schirra et al., 2014] Schirra, C. O., Brendel, B., Anastasio, M. A., and Roessl, E. (2014). Spectral CT: a technology primer for contrast agent development. *Contrast Media & Molecular Imaging*, 9(1):62–70.

[Schlomka et al., 2008] Schlomka, J. P., Roessl, E., Dorscheid, R., Dill, S., Martens, G., Istel, T., Bäumer, C., Herrmann, C., Steadman, R., Zeitler, G., Livne, A., and Proksa, R. (2008). Experimental feasibility of multi-energy photon-counting K-edge imaging in pre-clinical computed tomography. *Physics in Medicine and Biology*, 53(15):4031–4047.

[Schmidt, 2009] Schmidt, T. G. (2009). Optimal "image-based" weighting for energy-resolved CT. *Medical Physics*, 36(7):3018.

[Shepp and Vardi, 1982] Shepp, L. A. and Vardi, Y. (1982). Maximum Likelihood Reconstruction for Emission Tomography. *IEEE Transactions on Medical Imaging*, 1(2):113–122.

[Si-Mohamed et al., 2017a] Si-Mohamed, S., Bar-Ness, D., Sigovan, M., Cormode, D. P., Coulon, P., Coche, E., Vlassenbroek, A., Normand, G., Boussel, L., and Douek, P. (2017a). Review of an initial experience with an experimental spectral photon-counting computed tomography system. *Nuclear Instruments and Methods in Physics Research Section A: Accelerators, Spectrometers, Detectors and Associated Equipment*, 873:27–35.

[Si-Mohamed et al., 2018] Si-Mohamed, S., Bar-Ness, D., Sigovan, M., Tatard-Leitman, V., Cormode, D. P., Naha, P. C., Coulon, P., Rascle, L., Roessl, E., Rokni, M., Altman, A., Yagil, Y., Boussel, L., and Douek, P. (2018). Multicolour imaging with spectral photon-counting CT: a phantom study. *European Radiology Experimental*, 2(1):34.

[Si-Mohamed et al., 2017b] Si-Mohamed, S., Cormode, D. P., Bar-Ness, D., Sigovan, M., Naha, P. C., Langlois, J.-B., Chalabreysse, L., Coulon, P., Blevis, I., Roessl, E., Erhard, K., Boussel, L., and Douek, P. (2017b). Evaluation of spectral photon counting computed tomography K-edge imaging for determination of gold nanoparticle biodistribution in vivo. *Nanoscale*, 9(46):18246–18257.

[Sidky and Pan, 2008] Sidky, E. Y. and Pan, X. (2008). Image reconstruction in circular cone-beam computed tomography by constrained, total-variation minimization. *Physics in Medicine and Biology*, 53(17):4777–4807.

[Song et al., 2007] Song, J., Liu, Q. H., Johnson, G. A., and Badea, C. T. (2007). Sparseness prior based iterative image reconstruction for retrospectively gated cardiac micro-CT. *Medical Physics*, 34(11):4476–4483.

[Taguchi and Iwanczyk, 2013] Taguchi, K. and Iwanczyk, J. S. (2013). Vision 20/20: Single photon counting x-ray detectors in medical imaging. *Medical physics*, 40(10):100901.

[Taguchi et al., 2007] Taguchi, K., Zhang, M., Frey, E. C., Xu, J., Segars, W. P., and Tsui, B. M. W. (2007). Image-domain material decomposition using photon-counting CT. *Proceedings of SPIE*, 6510(1):651008–651008–12.

[Tian et al., 2011] Tian, Z., Jia, X., Yuan, K., Pan, T., and Jiang, S. B. (2011). Low-dose CT reconstruction via edge-preserving total variation regularization. *Physics in Medicine and Biology*, 56(18):5949–5967.

[Tibshirani, 1996] Tibshirani, R. (1996). Regression Shrinkage and Selection Via the Lasso. *Journal of the Royal Statistical Society: Series B (Methodological)*, 58(1):267–288.

[Touch et al., 2016] Touch, M., Badea, C. T., Lo, J. Y., and Reiman, R. E. (2016). *Machine Learning-based Techniques to Address Spectral Distortions in Photon Counting X-ray Computed Tomography*. PhD thesis, Duke University.

[Vacca, 1981] Vacca, R. (1981). *Regression Diagnostics — Identifying Influential Data and Sources of Collinearity*, volume 32. Wiley.

[Verbeek and Roobol, 2018] Verbeek, J. F. M. and Roobol, M. J. (2018). What is an acceptable false negative rate in the detection of prostate cancer? *Translational Andrology and Urology*, 7(1):54–60.

[Wang et al., 2012] Wang, S., Zhang, D., Liang, Y., and Pan, Q. (2012). Semi-coupled dictionary learning with applications to image super-resolution and photo-sketch synthesis. *IEEE Conference on Computer Vision and Pattern Recognition (CVPR), 2012*, pages 2216–2223.

[WANG and LIAO, 2001] WANG, S. L. and LIAO, L. Z. (2001). Decomposition Method with a Variable Parameter for a Class of Monotone Variational Inequality Problems. *Journal of Optimization Theory and Applications*, 109(2):415–429.

[Wang et al., 2013] Wang, Y., Qian, B., Li, B., Qin, G., Zhou, Z., Qiu, Y., Sun, X., and Zhu, B. (2013). Metal artifacts reduction using monochromatic images from spectral CT: Evaluation of pedicle screws in patients with scoliosis. *European Journal of Radiology*.

[Weidinger et al., 2016] Weidinger, T., Buzug, T. M., Flohr, T., Kappler, S., and Stierstorfer, K. (2016). Polychromatic Iterative Statistical Material Image Reconstruction for Photon-Counting Computed Tomography. *International Journal of Biomedical Imaging*.

[Wu et al., 2016] Wu, D., Zhang, L., Zhu, X., Xu, X., and Wang, S. (2016). A weighted polynomial based material decomposition method for spectral x-ray CT imaging. *Physics in Medicine and Biology*, 61(10):3749–3783.

[Wu et al., 2009] Wu, X., Langan, D. A., Xu, D., Benson, T. M., Pack, J. D., Schmitz, A. M., Tkaczyk, E. J., Leverentz, J., and Licato, P. (2009). Monochromatic CT image representation via fast switching dual kVp. volume 7258, page 725845.

[Xia et al., 2019] Xia, W., Wu, W., Niu, S., Liu, F., Zhou, J., Yu, H., Wang, G., and Zhang, Y. (2019). Spectral CT Reconstruction—ASSIST: Aided by Self-Similarity in Image-Spectral Tensors. *IEEE Transactions on Computational Imaging*, 5(3):420–436.

[Xie et al., 2019] Xie, B., Su, T., Kaftandjian, V., Niu, P., Yang, F., Robini, M., Zhu, Y., and Duvauchelle, P. (2019). Material Decomposition in X-ray Spectral CT Using Multiple Constraints in Image Domain. *Journal of Nondestructive Evaluation*, 38(1):16.

[Yang et al., 2010] Yang, J., Wright, J., Huang, T. S., and Ma, Y. (2010). Image super-resolution via sparse representation. *IEEE Transactions on Image Processing*, 19(11):2861–2873.

[Yu et al., 2011] Yu, L., Christner, J. A., Leng, S., Wang, J., Fletcher, J. G., and McCollough, C. H. (2011). Virtual monochromatic imaging in dual-source dual-energy CT: radiation dose and image quality. *Medical physics*, 38(12):6371–9.

[Yu et al., 2012] Yu, L., Leng, S., and McCollough, C. H. (2012). Dual-Energy CT–Based Monochromatic Imaging. *American Journal of Roentgenology*, 199(5_supplement):S9–S15.

[Yu et al., 2016] Yu, Z., Leng, S., Li, Z., and McCollough, C. H. (2016). Spectral prior image constrained compressed sensing (spectral PICCS) for photon-counting computed tomography. *Physics in Medicine and Biology*, 61(18):6707–6732.

[Zainon, 2012] Zainon, R. (2012). *Spectral Micro-CT Imaging of Ex Vivo Atherosclerotic Plaque*. PhD thesis, University of Canterbury.

[Zeng et al., 2016] Zeng, D., Bian, Z., Gong, C., Huang, J., He, J., Zhang, H., Lu, L., Feng, Q., Liang, Z., and Ma, J. (2016). Iterative image reconstruction for multienergy computed tomography via structure tensor total variation regularization. page 978349.

[Zhang et al., 2017] Zhang, Y., Mou, X., Wang, G., and Yu, H. (2017). Tensor-Based Dictionary Learning for Spectral CT Reconstruction. *IEEE Transactions on Medical Imaging*, 36(1):142–154.

[Zhang et al., 2016] Zhang, Y., Xi, Y., Yang, Q., Cong, W., Zhou, J., and Wang, G. (2016). Spectral CT Reconstruction With Image Sparsity and Spectral Mean. *IEEE Transactions on Computational Imaging*, 2(4):510–523.

[Zhao et al., 2012] Zhao, L.-q., He, W., Li, J.-y., Chen, J.-h., Wang, K.-y., and Tan, L. (2012). Improving image quality in portal venography with spectral CT imaging. *European Journal of Radiology*, 81(8):1677–1681.

[Zhao et al., 2016] Zhao, W., Niu, T., Xing, L., Xie, Y., Xiong, G., Elmore, K., Zhu, J., Wang, L., and Min, J. K. (2016). Using edge-preserving algorithm with non-local mean for significantly improved image-domain material decomposition in dual-energy CT. *Physics in Medicine and Biology*, 61(3):1332–1351.

[Zhou et al., 2018] Zhou, W., Lane, J., Carlson, M., Bruesewitz, M., Witte, R., Koeller, K., Eckel, L., Carter, R., McCollough, C., and Leng, S. (2018). Comparison of a Photon-Counting-Detector CT with an Energy-Integrating-Detector CT for Temporal Bone Imaging: A Cadaveric Study. *American Journal of Neuroradiology*, 39(9):1733–1738.

[Zimmerman and Schmidt, 2015] Zimmerman, K. C. and Schmidt, T. G. (2015). Experimental comparison of empirical material decomposition methods for spectral CT. *Physics in Medicine and Biology*, 60(8):3175–3191.

# Abbreviations

**ASIC** Application-specific Integrated Circuit

**ADMM** Alternating Direction Method of Multipliers

**CNR** Contrast-to-noise Ratio

**CT** Computed Tomography

**CdTe** Cadmium Telluride

**DECT** Dual-energy Computed Tomography

**EID** Energy Integrating Detector

**FBP** Filtered Back-projection

**keV** Kiloclectron Volts

**LER** Low Energy Resolution

**LS** Least Squares

**ML** Maximum-Likelihood

**PCD** Photon Counting Detector

**PMMA** Poly(Methyl Methacrylate)

**ROI** Region of Interest

**sCT** Spectral Computed Tomography

**SER** Super Energy Resolution

**SNR** Signal-to-noise Ratio

**TV** Total Variation

# Main Symbols

$B$ Number of energy bins

$d(E)$ Detector response function

$E$ Energy

$\boldsymbol{M}$ Decomposition matrix

$n_i$ Expected number of photons at the $i$-th bin

$P_\alpha$ Density integral of material $\alpha$

$\boldsymbol{X}$ Decomposed basis material images

$\boldsymbol{Y}$ Reconstructed multi-energy spatial images

$Z$ Atomic number

$\mu$ Linear attenuation coefficient

$\mu_{\mathrm{m}}$ Mass attenuation coefficient

$\rho$ Density

$\lambda_i$ Expected number of photons in the i-*th* energy bin

$\|\cdot\|_F$ Frobenius norm

$\|\cdot\|_1$ L1 norm

$\|\cdot\|_2$ L2 norm

$\|\cdot\|_{2,1}$ L2,1 norm

$\|\cdot\|_*$ Nuclear norm

$\bigtriangledown \boldsymbol{X}$ Gradient matrix of X

FOLIO ADMINISTRATIF

THESE DE L'UNIVERSITE DE LYON OPEREE AU SEIN DE L'INSA LYON

NOM : XIE
(avec précision du nom de jeune fille, le cas échéant)

DATE de SOUTENANCE : 19/03/2020

Prénoms : Bingqing

TITRE : Image-domain material decomposition in spectral photon-counting CT for medical applications

NATURE : Doctorat

Numéro d'ordre : 2020LYSEI021

Ecole doctorale : Electronique, électrotechnique, automatique (EEA)

Spécialité : Traitement du Signal et de l'Image

RESUME :
La décomposition de matériaux est un problème fondamental et primordial dans la tomographie spectrale (sCT—spectral computed tomography) par rayons X basée sur des détecteurs à comptage de photons (PCD—photon counting detector). La présente thèse porte sur le développement de méthodes de décomposition de matériaux en utilisant des informations spectrale et morphologique encodées dans des images sCT multi-énergie. Dans ce cadre, trois méthodes ont été développées. Pour la première méthode, en utilisant la densité de masse limitée, la parcimonie conjointe locale, et le faible rang structurel (DSR) dans le domaine de l'image, nous obtenons une décomposition très précise de matériaux tels que le gadolinium, l'iode et le fer. Les résultats sur les données numériques et physiques du fantôme ont démontré que la méthode DSR proposée conduit à une décomposition plus précise que la méthode pseudo-inverse habituelle avec décomposition en valeur singulière (SVD—singular value decomposition) et la méthode de régularisation parcimonieuse courante avec contrainte de norme L1 (lasso). La deuxième méthode opère par région. Elle consiste à optimiser les matériaux de base en se basant sur la segmentation spatio-énergétique des régions d'intérêt (ROI—regions-of-interests) dans les images sCT, à réduire le bruit en faisant le moyennage des images spatiales multi-énergie, et à effectuer une décomposition fine des matériaux impliquant une matrice de décomposition optimisée, une régularisation du débruitage et une régularisation parcimonieuse. Les résultats sur des données numériques et physiques ont montré que la méthode proposée de décomposition des matériaux ROI par ROI (ROI-wise—region-of-interests-wise) présente une fiabilité et une précision nettement supérieures à celles des méthodes de décomposition courantes fondées sur la régularisation de la variation totale (TV) ou de la norme L1. Dans la troisième méthode, nous proposons la notion d'imagerie sCT à super-résolution énergétique (SER—super-energy-resolution), qui est réalisée en établissant la relation entre la simulation et les fantômes physiques au moyen d'un apprentissage par dictionnaire couplé, de manière pixel par pixel. L'efficacité de ces méthodes proposées a été validée sur des données de fantômes numériques, de fantômes physiques et in vivo. Les résultats montrent que, pour la même méthode de décomposition de matériaux utilisant la régularisation par lasso, l'imagerie à super-résolution énergétique proposée présente une précision de décomposition et un pouvoir de détection beaucoup plus élevé que ce que peut fournir la machine sCT actuelle.

MOTS-CLÉS : Tomographie, Rayons X, CT spectrale, Détecteur à comptage des photons, Décomposition de matériaux, Apprentissage machine, Représentation éparse

Laboratoire (s) de recherche : CREATIS

Directeur de thèse: ZHU Yuemin

Président de jury :

Composition du jury : LAQUERRIERE Patrice, VINCENT Nicole, PIERE-SIMON Jouk, ZHU Yuemin, KAFTANDJIAN Valérie, DUVAUCHELLE Philippe